



The order in disorder:  
Magnetism in amorphous cobalt-based thin films and  
heterostructures

Kristbjörg Anna Þórarinsdóttir



Faculty of Science  
School of Engineering and Natural Sciences  
University of Iceland  
2022



**The order in disorder:  
Magnetism in amorphous cobalt-based thin films  
and heterostructures**

Kristbjörg Anna Þórarinsdóttir

Dissertation submitted in partial fulfillment of a  
*Philosophiae Doctor* degree in Physics

Advisor  
Friðrik Magnus

PhD Committee  
Friðrik Magnus  
Björgvin Hjörvarsson  
Snorri Þorgeir Ingvarsson

Opponents  
Eric Fullerton  
Sarah Thompson

Faculty of Science  
School of Engineering and Natural Sciences  
University of Iceland  
Reykjavík, June 2022

The order in disorder: Magnetism in amorphous cobalt-based thin films and heterostructures

Dissertation submitted in partial fulfillment of a *Philosophiae Doctor* degree in Physics

Copyright © Kristbjörg Anna Þórarinsdóttir 2022  
All rights reserved

Faculty of Science  
School of Engineering and Natural Sciences  
University of Iceland  
Dunhaga 3  
107, Reykjavík, Reykjavík  
Iceland

Telephone: 525-4000

Bibliographic information:

Kristbjörg Anna Þórarinsdóttir, 2022, *The order in disorder: Magnetism in amorphous cobalt-based thin films and heterostructures*, PhD dissertation, Faculty of Science, University of Iceland, 101 pp.

ISBN 978-9935-9630-3-1

Printing: Háskólaprent, Fálkagata 2, 107 Reykjavík  
Reykjavík, Iceland, June 2022

Hversu flókið getur það verið?

*Friðrik Magnus*

*Tíleinkað dásamlegu foreldrum mínum, kys og knús.*

# Abstract

The work in this thesis is focused on understanding the emergent properties of amorphous magnetic materials. Amorphous materials lack long-range structural ordering, characteristic of crystalline materials. Instead, these materials exhibit medium-to-short range order. In elemental form, metals always form crystals but can be amorphized by alloying with other metals of different atomic radii.

To study the magnetic properties of amorphous magnetic metals, we use CoAlZr and TbCo of various compositions, both in single layers and nanolaminates. The samples were fabricated using direct current magnetron sputtering in an ultra-high vacuum system. Structural characterization was done using x-ray reflectivity and grazing incidence x-ray diffraction. The magnetic properties were measured using magneto-optic Kerr effect, vibrating sample magnetometry, and polarized neutron reflectometry.

First, we show how the magnetic properties of the ferromagnetic Co are affected by diluting it with non-magnetic AlZr. We find that the critical temperature and magnetization of CoAlZr depends on composition, and decreases linearly with increasing AlZr content. Due to the disordered structure, there is a local distribution in Co concentration with regions of high and low Co density. We find a surprising manifestation of this chemical modulation, which emerges as competing anisotropies. By analyzing the anisotropy as a function of composition, we can define quantitatively a cobalt composition distribution on the nanoscale (Paper III). Similar to the CoAlZr, we also observe competing anisotropy in the TbCo alloy. We find, by analyzing the effective anisotropy as a function of composition and thickness, that there are two competing anisotropy terms in the TbCo layer: interface and bulk anisotropy. The interface favors in-plane magnetization while the bulk favors perpendicular magnetization (Paper IV).

In the second part of this study, we focus on hybrid structures composed of multilayers of alternating high- and low-  $T_c$  CoAlZr and bilayers of TbCo and CoAlZr. In the CoAlZr multilayers, we find that within the low- $T_c$  layer there is a non-zero magnetization at three times its intrinsic ordering temperature which extends through at least 10 nm. This is due to the proximity to the ferromagnetic (high  $T_c$ ) layer (Paper I). In the TbCo/CoAlZr bilayers, we investigate the exchange coupling between two layers with crossed magnetic anisotropies. We find that a 7.5 nm interface layer of the CoAlZr is strongly exchange coupled to the TbCo with a magnetization perpendicular to the plane and switches in unison with the TbCo layer (Paper II). To resolve the depth dependence of the magnetization, these hybrid structures are then investigated further using polarized neutron reflectivity (Paper V).





# Útdráttur

Í þessari ritgerð er lögð áhersla á að skilja seguleiginleika myndlausra efna. Myndlaus efni skortir langrækna kristaluppbyggingu, en þess í stað geta þessi efni haft stutta eða meðallanga uppröðun. Málmar sem frumefni mynda alltaf kristalla, en hægt er að búa til myndlausu málma með því að blanda saman tveimur eða fleiri mismunandi málum, með misstóra frumeindaradíusa, í melmi.

Til að rannsaka seguleiginleika myndlausra málma notum við CoAlZr og TbCo í ýmsum samsetningum, bæði sem einlög og í marglögum. Sýnin eru búin til með jafnstraumssegulspætun í ofurháu lofttæmiskerfi. Byggingareiginleikar sýnanna voru greindir með röntgenspeglun og lághornsröntgenbognun. Seguleiginleikarnir voru mældir með MOKE, VSM og með skautaðri nifteindaspeglun.

Fyrst sýnum við hvernig seguleiginleikar járnseglandi Co breytast með því að mynda melmi með óseglandi AlZr. Við sjáum að Curie hitastigið og segulvægið á CoAlZr stjórnast af samsetningunni, og minnkar línulega með auknu AlZr innihaldi. Vegna óreiðukenndrar uppröðunar á myndlausum efnum er staðbundin dreifing í Co innihaldi sem gefur svæði með háum og lágum þéttleika af Co. Þetta leiðir til staðbundins breytileika í Curie hitastigi. Við sjáum óvænta birtingamynd af þessari dreifingu í efnasamsetningu, sem kemur fram sem keppni milli ólíkrar segulmisáttunar. Með því að mæla hver segulmisáttunin er sem fall af samsetningu, getum við skilgreint Co samsetningardreifingu (Grein III). Svipað og með CoAlZr, þá mælum við líka samkeppni milli mismunandi segulmisáttunar í TbCo melmi. Við sjáum, með því að greina seguláttun sem fall af samsetningu og þykkt, að það eru tvær segulmisáttanir að keppast í TbCo laginu: yfirborðs- og bolsegulmisáttun. Yfirborðið er auðseglandi í plani húðarinnar á meðan bolurinn er auðseglandi hornrétt á planið (Grein IV).

Í seinni hluta rannsóknarinnar, einblínum við á fjöllög af há- og lág- $T_c$  CoAlZr lögum á víxl og tvílögum af TbCo/CoAlZr. Í CoAlZr fjöllögum sýnum við að í lág- $T_c$  laginu er framkallaður ofurmeðseglandi fasi vegna nálægðar við há- $T_c$  lagið. Þetta segulástand er langreikið og er til staðar við hitastig sem er þrisvar sinnum hærra en innra Curie hitastig lág- $T_c$  lagsins (Grein I). Í TbCo/CoAlZr tvílögum rannsökum við segulskiptikrafta milli laga með hornréttu og láréttu seguláttun miðað við plan sýnisins. Við greinum svæði í CoAlZr laginu, þar sem segulspunarnir eru sterkt tengdir við TbCo lagið og hluti spunaáferðar CoAlZr lagsins liggur þvert á húðina. Þetta svæði hefur svipaða seguleiginleika og TbCo lagið, og verkar því eins og segulgormur (Grein II). Til að greina dýptarhæði seguláferðarinnar, framkvæmum við mælingu með skautaðri nifteindaspeglun (Grein V).



# Table of Contents

Abstract	v
Útdráttur	vii
Table of Contents	ix
List of Original Papers	xi
Acknowledgments	xiii
<b>1 Introduction</b>	<b>1</b>
<b>2 Survey of magnetic properties</b>	<b>3</b>
2.1 Exchange interactions . . . . .	4
2.2 Magnetic ordering . . . . .	7
2.3 Magnetic anisotropy . . . . .	11
2.4 Nanolaminates . . . . .	19
<b>3 Experimental methods</b>	<b>21</b>
3.1 Sample fabrication . . . . .	21
3.2 Structural characterization . . . . .	25
3.3 Magnetic characterization . . . . .	29
<b>4 Competing magnetic anisotropies</b>	<b>37</b>
4.1 Order in randomness . . . . .	37
4.2 Magnetic phase diagram of TbCo . . . . .	44
<b>5 Hybrid structures</b>	<b>49</b>
5.1 Giant magnetic proximity effect . . . . .	49
5.2 Exchange spring magnets . . . . .	51
<b>6 Concluding thoughts</b>	<b>55</b>
Bibliography	57
Abbreviations	65
<b>7 Original papers</b>	<b>67</b>
Paper I . . . . .	69
Paper II . . . . .	79
Paper III . . . . .	87



# List of Original Papers

- I **Giant magnetic proximity effect in amorphous layered magnets.**  
**K.A. Thórarinsdóttir**, H. Palonen, G. K. Pálsson, B. Hjörvarsson, F. Magnus  
Physical Review Materials **3**, 054409, 2019.
  
- II **Amorphous exchange-spring magnets with crossed perpendicular and in-plane anisotropies.**  
**K.A. Thórarinsdóttir**, T. Hase, B. Hjörvarsson, F. Magnus  
Physical Review B **103**, 014440, 2021.
  
- III **Finding order in disorder: Magnetic coupling distributions and competing anisotropies in an amorphous metal alloy.**  
**K.A. Thórarinsdóttir**, N. Strandqvist, V.V Sigurjónsdóttir, E.B. Thorsteins-  
son, B. Hjörvarsson, F. Magnus  
APL Materials **10**, 041103, 2022.
  
- IV **Tuneable spin reorientation transitions in Co-rich TbCo amorphous thin films.**  
**K.A. Thórarinsdóttir**, B.R. Thorbjarnardóttir, U.B. Arnalds, F. Magnus  
In manuscript, 2022.
  
- V **Magnetization profile of an exchange spring magnet with crossed perpendicular and in-plane magnetic anisotropy.**  
**K.A. Thórarinsdóttir**, N. Strandqvist, A. Caruana, C. Kinane, U.B. Arnalds,  
B. Hjörvarsson, F. Magnus  
In manuscript, 2022.



## Acknowledgments

I would like to thank my supervisor Friðrik Magnus for his bottomless patience and impeccable supervision. I am forever grateful for this opportunity and the last four years have been filled with joy, excitement and anxiety. I am going to miss showing up unannounced to your office to ramble something about hysteresis loops and then run away before you have had any time to process. I would also like to thank Björgvin Hjörvarsson and Snorri Þorgeir Ingvarsson for their valuable discussions and guidance. I can not imagine a better team of supervisors!

My dearest friend and coworker Nanny Strandqvist!!! I can truly say that this would not have been possible without you, our travels and (almost) daily discussions. Even though we could not meet up for almost two years due to the Covid situation, it still felt like you were right next to me when I was asking you stupid questions.

No matter if the VSM was broken or nothing made sense, showing up to work always made everything better because of the amazing and beautiful staff in VR-III. Kibbi, Taha, Einar, Ásgeir, Unnar, Árni, Davíð, and Sibbi. Having lunch with all of you (at 11:30 sharp) was pretty often the highlight of my day. Special thanks to Kibbi for being the most entertaining person in the lab, stealing plants and ganging up against everyone with you was a lot of fun (for us). Taha and Einar, thank you for listening to my infodump and all the other stuff (and I also listened to you, so you are both welcome). I could/can always count on both of you, both with help in the lab and venting. Árni and Unnar, thank you for all of the help throughout the years, it really meant a lot to me. Big thanks to "my" beamline scientists Andrew Caruana (good cop) and Christy Kinane (bad cop), I really enjoy working with the two of you and I have learned a lot from our collaboration.

To my friends Hallmann, Olga and Pétur. Thank you for keeping me entertained throughout the years, our friendship means the world to me and I am excited to intermix our fields so we can go to conferences together.

Of course I cannot leave out the computational chemists and theoretical/experimental physicists, especially Barði, Aleksei, Mohammad, Swetha, Kristina, and Villi. Shotgunning a beer on the roof of VR-III would not have been the same without you all.

Special thanks to Ari Ólafsson, I am so grateful for everything you have taught me and for hiring me to work in Vísindasmiðjan. Working with you and Martin Swift helped me grow into the person I am today.

Ísak, Vala and Örn, thank you for being your wonderful self!!

Finally, my lovely parents and brothers. Thank you for being there and being patient while I spent the last nine years focusing on my studies.





# Chapter 1

## Introduction

The 2021 Nobel prize in physics was awarded to Klaus Hasselmann, Syukuro Manabe, and Giorgio Parisi “for groundbreaking contributions to our understanding of complex systems”[1]. Complex systems are not the same as complicated systems. They have many interacting parts and emerging properties, which are very difficult to model. This could for example be Earth’s climate system, the spread of a pandemic, or a material such as *glass*.

In pure metals, the atoms arrange periodically, forming crystals. The arrangement can then be described by one of the Bravais lattices, which are different configurations the crystal can exhibit. With various deposition methods, it is possible to fabricate alloys that do not have this periodic arrangement. Such materials are called amorphous and have a disordered atomic arrangement, and can therefore not be described by a set of lattice vectors. The amorphous structure can, for example, be achieved by alloying two elements with a large difference in atomic radius and/or crystal structure. Glass, for instance, lacks periodic structure and this is where amorphous metal alloys get their name: *metallic glass*.

In crystals, the amount of elements that can be alloyed together, before precipitating or segregating, is limited. In amorphous materials, there is no long-range periodic structure, and consequently no point defects or lattice mismatch. As a result, the composition range where two or more elements can be alloyed together, without forming small crystals, is much larger. The magnetic properties of any alloy, crystalline or amorphous, depend on composition and thickness. Therefore the magnetic properties of amorphous alloys can be tuned over a large composition range. Additionally, amorphous thin films tend to be very flat, have excellent layering and well-defined layer thickness. This enables the fabrication of high-quality amorphous heterostructures [2–5].

In an amorphous alloy containing two elements, the two elements will not be uniformly spread out, but there will be regions within the material where the density of one element exceeds the other, resulting in local variations

in the composition [6]. If we now say that one element is magnetic, and the other is non-magnetic, then it becomes apparent that within the film the magnetic properties are inhomogeneous.

This inhomogeneity results in elusive magnetic properties, such as long-range exchange coupling and giant proximity effects. Due to the lack of crystalline order, it is challenging to study and identify the origin of these effects. The work in this thesis is dedicated to magnetic amorphous alloys, and to gain insight into what determines their elusive magnetic properties.

Chapter 2 provides a brief overview of the origin of magnetism and the fundamental theory needed for the work of this thesis. The fabrication of thin films and structural and magnetic characterization is summarized in chapter 3. The work of this thesis is then divided into two final chapters. In chapter 4 we first show the effect of the disordered structure of amorphous CoAlZr, and how the magnetic moment and critical temperature change with composition. We find that the variation in composition within the thin film can be described by a gaussian distribution function (Paper III). Second, we study the magnetic properties of Co rich TbCo, and show how the effective anisotropy changes with composition and thickness (Paper IV). In chapter 5 we examine hybrid structures composed of CoAlZr and TbCo. First, structures composed of multilayers of alternating high- and low- $T_c$  CoAlZr are studied. We find that within the low- $T_c$  layer, that due to the proximity of the ferromagnetic (high- $T_c$ ) layer, there is a non-zero magnetization at three times its intrinsic ordering temperature which extends through at least 10 nm (Paper I). Second, spring magnets with crossed magnetic anisotropy formed of TbCo and CoAlZr with long-range exchange coupling are examined. By studying the thickness dependence of the magnetic properties, we find that a substantial interface layer of the CoAlZr is pinned out-of-plane with the TbCo, acting as an extension to it (Papers II and V).

# Chapter 2

## Survey of magnetic properties

Magnetism mainly arises from the electrons of atoms and molecules with unpaired spins. Most materials in our surroundings are described as "non-magnetic". This strictly means, that in the absence of a magnetic field, there is no magnetic field originating from those materials. Also, in the presence of an external field, any attraction (or repulsion) is usually very weak. In the periodic table of elements, most elements are described as non-magnetic. If the electron shells are complete (all electrons are paired) the material is diamagnetic. If there are unpaired spins, each atom acts as a tiny magnet due to the uncanceled moment of each unpaired electron, these materials are referred to as *paramagnetic*.

If the coupling between the electrons of the paramagnetic material (the exchange interaction) is strong enough, these tiny moments can align so they all point microscopically in the same direction and the magnetic moment of all the atoms adds up. These materials are called ferro- or ferrimagnets, or just permanent magnets. Fe, Co, and Ni, shown in pink in the abbreviated periodic table of the elements in Fig. 2.1, are the *only* three elements that have this long-range order at room temperature. Although, only these three elements are magnetic at room temperature, the elements belonging to the rare-earth (RE) group, highlighted in yellow and orange in Fig. 2.1, have a non-zero magnetic moment and become magnetically ordered below room temperature.

By alloying the magnetic transition metals (TM) with, for example RE metals, it is possible to fabricate materials with magnetic properties that do not exist in pure elements. RE-TM magnets are, for example, used as permanent magnets, as they are much stronger magnets than a rod of iron. In this thesis, we study amorphous thin films of  $\text{Co}_x\text{AlZr}_{1-x}$  and  $\text{Tb}_{1-y}\text{Co}_y$  with  $x = 65 - 100\%$  and  $y = 88 - 92\%$ . Although both alloys contain mostly cobalt, these two systems exhibit very different magnetic properties due to the difference in magnetic interactions of the elements.

In the following section, we first give a brief introduction to the origin of magnetism and the interaction between localized spins, to give a funda-

Transition Metals										Other metals									
										<div>1326.982</div> <div><b>Al</b></div> <div>Aluminium</div>									
2144.956 <b>Sc</b> Scandium	2247.867 <b>Ti</b> Titanium	2350.942 <b>V</b> Vanadium	2451.996 <b>Cr</b> Chromium	2554.938 <b>Mn</b> Manganese	2655.845 <b>Fe</b> Iron	2758.933 <b>Co</b> Cobalt	2858.693 <b>Ni</b> Nickel	2963.546 <b>Cu</b> Copper	3065.39 <b>Zn</b> Zinc	3169.723 <b>Ga</b> Gallium									
3988.906 <b>Y</b> Yttrium	4091.224 <b>Zr</b> Zirconium	4192.906 <b>Nb</b> Niobium	4295.94 <b>Mo</b> Molybdenum	4395.94 <b>Tc</b> Technetium	44101.07 <b>Ru</b> Ruthenium	45102.91 <b>Rh</b> Rhodium	46106.42 <b>Pd</b> Palladium	47107.87 <b>Ag</b> Silver	48112.41 <b>Cd</b> Cadmium	49114.82 <b>In</b> Indium	50118.71 <b>Sn</b> Tin								
57-71 <b>La-Lu</b> Lanthanide	72178.49 <b>Hf</b> Hafnium	73180.95 <b>Ta</b> Tantalum	74183.84 <b>W</b> Tungsten	75186.21 <b>Re</b> Rhenium	76190.23 <b>Os</b> Osmium	77192.22 <b>Ir</b> Iridium	78195.08 <b>Pt</b> Platinum	79196.97 <b>Au</b> Gold	80200.59 <b>Hg</b> Mercury	81204.38 <b>Tl</b> Thallium	82207.2 <b>Pb</b> Lead	83208.98 <b>Bi</b> Bismuth							
<div>57138.91 <b>La</b> Lanthanum</div> <div>58140.12 <b>Ce</b> Cerium</div> <div>59140.91 <b>Pr</b> Praseodymium</div> <div>60144.24 <b>Nd</b> Neodymium</div> <div>61145 <b>Pm</b> Promethium</div> <div>62150.36 <b>Sm</b> Samarium</div> <div>63151.96 <b>Eu</b> Europium</div> <div>64157.25 <b>Gd</b> Gadolinium</div> <div>65158.93 <b>Tb</b> Terbium</div> <div>66162.50 <b>Dy</b> Dysprosium</div> <div>67164.93 <b>Ho</b> Holmium</div>																			
<div>←LightHeavy→</div>																			
Rare Earth																			

Figure 2.1: Selected elements from the periodic table of elements. The bold framed elements are the Co, Tb, Al and Zr. Co and Tb are interesting from a magnetic properties point of view. The non-magnetic Al and Zr are alloyed with Co to form amorphous CoAlZr. Figure adapted from [7].

mental understanding of the exchange interaction. We then also discuss, the more appropriate, magnetism of itinerant electrons. We also describe the different magnetic orderings and their temperature dependence and various anisotropy terms. In the last section, we discuss hybrid structures, composed of layers of different magnetic materials. These discussions will be mostly limited to the magnetic elements Tb and Co.

## 2.1 Exchange interactions

Magnetism arises due to the unpaired spins in the outermost electron shell. The unpaired spins in the TM iron group are located on the  $3d$  orbital, while for RE they are located on the  $4f$  orbital. In the most simple model, the atom is composed of a nucleus, and the electrons form shells around it, where each shell can contain a limited even number of electrons. For cobalt, the  $3d$  electrons interact strongly due to large overlap of the orbital wavefunctions resulting in *direct exchange coupling*. Due to the shielding of the  $4f$  electrons of Tb, we do not get direct overlap of the orbitals, but nevertheless we have magnetic order mediated by conduction electrons through *indirect exchange coupling* [8].

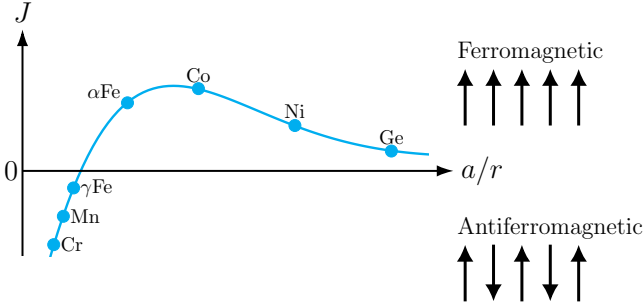


Figure 2.2: Bethe-Slater curve. The exchange coupling  $J$  depends on the ratio between the interatomic distance  $a$  and the radius of the orbital  $r$ . Depending on the sign of the exchange integral  $J$ , the magnetic moments either align parallel ( $J > 0$ ) or antiparallel ( $J < 0$ ). Figure adapted from Ref. [9].

### 2.1.1 Direct exchange coupling

Let us first consider the case of localized moments. The exchange interaction between localized electron spins leads to ferromagnetism and other forms of magnetic ordering as a result of the Dirac-Heisenberg exchange interaction. The exchange interaction between two electrons,  $\vec{S}_i$  and  $\vec{S}_j$ , can be described by the Hamiltonian [8]

$$H = -2J \sum_{i < j} \vec{S}_i \cdot \vec{S}_j \quad (2.1)$$

where  $J$  is the isotropic exchange constant. The exchange constant  $J$  is a purely quantum mechanical term which does not have a classical analog. It emerges from the electrostatic interaction between the electrons and nucleus and lowers the total Coulomb energy. For antiferromagnetic or ferrimagnetic materials, the exchange constant is negative, so that the energy is at a minimum when  $\vec{S}_i$  and  $\vec{S}_j$  are antiparallel. For ferromagnetic materials,  $J$  is positive so that  $\vec{S}_i$  and  $\vec{S}_j$  align in parallel.

In 3d transition metals, the strength of the exchange coupling  $J$  can be described by the Bethe-Slater curve, which depends on the ratio between the interatomic distance  $a$  between interacting atoms and the radius  $r$  of the electron shell [10, 11]. The dependence of  $J$  on  $a/r$  is illustrated in Fig. 2.2. When  $a/r$  is small  $J$  is antiferromagnetic, and as the ratio increases, the ordering becomes ferromagnetic.

The Bethe-Slater curve correctly predicts the ferromagnetic ordering in Fe, Co, Ni, and Gd, where only the first three have long range order at

room temperature. From the Heisenberg Hamiltonian, the magnetization is due to partially filled orbitals of interacting atoms with localized electrons. In solids, the energy states are not well defined, or local, and this is due to the Pauli exclusion principle. According to Pauli, no two electrons with the same four quantum numbers (three spatial and one spin) can occupy the same state. So within the atom, each state can contain one electron with spin up and one with spin down. In solids, the wave functions of neighboring atoms overlap, resulting in more than two electrons occupying the same state, which is against the Pauli exclusion principle. This causes each energy state to split up into multiple energy states, where each state only contains two electrons. When the difference between these energies becomes small, we can approximate the energy distribution as a continuum, or a band [9]. The number of states per energy that an electron can occupy is given by the density of states,  $g(E)$  (DOS). In non-magnetic solids, the number of electrons with spin up and spin down is equal. If the DOS near the Fermi level and the exchange coupling,  $J$ , are large enough, it can become more energetically favorable to have an uneven number of up and down electrons, i.e. raising the energy of a spin down electron, to spin up, resulting in a spontaneous ferromagnetic ordering. This is known as the Stoner criterion [12], which is fulfilled when

$$Ug(E_F) \geq 1 \quad (2.2)$$

where  $U$  is the Coulomb energy of the sub bands, and  $g(E_F)$  is the density of states at the Fermi level (see for example [8]). This criterion is only fulfilled for three elemental metals, namely Fe, Ni, and Co [13], which are the only three *room temperature* ferromagnetic elements. These three elements lose their magnetic order at very high temperatures, 900 K for Ni, 1043 K for Fe and, 1400 K for Co. Other metals can also have magnetic ordering, but this occurs below room temperature, for example 293 K for Gd, 220 K for Tb, and 89 K for Dy. These metals belong to the RE group (yellow and orange elements in Fig. 2.1) and have a significantly lower critical temperature than the TM metals, but a much larger magnetic moment, and in some cases, a very large anisotropy. It is therefore useful to combine these elements in an alloy to achieve the large moment and anisotropy of the RE and the high critical temperature of the TM.

### 2.1.2 RE - TM alloys

The large magnetic moment of the rare earth elements comes from the large number of unpaired spins in the  $f$  orbital. The low critical temperature is due to the much weaker exchange coupling of RE metals. The  $4f$  electrons

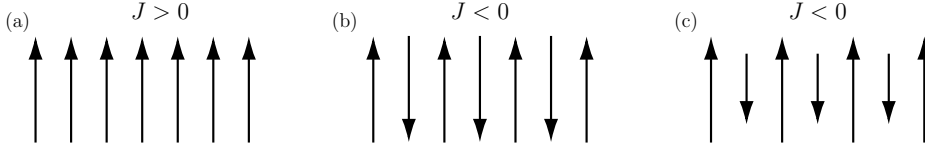


Figure 2.3: **(a)** Ferromagnetic ordering,  $J > 0$ . **(b)** Antiferromagnetic ordering,  $J < 0$ . **(c)** Ferrimagnetic ordering,  $J < 0$ .  $J$  is the exchange constant from Eq. 2.1.

are localized, and lie spatially closer to the core than the valence electrons, leading to minimal direct overlap of the  $f$  electrons between RE atoms. Instead the magnetic ordering is mediated by the conduction electrons, which are polarized by the  $4f$  electrons through *indirect exchange coupling*. This is approximately 100 times weaker than the direct exchange coupling between TM-TM materials [14].

The magnetic properties of RE-TM alloys are highly material and composition dependent, and the magnetic ordering of RE-RE and RE-TM alloys is far from trivial. The TM elements usually have a relatively simple ferromagnetic ordering, while the spin structure of RE elements can be ferromagnetic, antiferromagnetic or even helical [15]. The coupling in RE-TM alloys depends on the alloy, but can be roughly divided up into two parts: i) Light RE-TM alloys which couple ferromagnetically (SmCo [4], etc) and ii) Heavy RE-TM alloys which couple antiferromagnetically (TbCo [16], TbFe [17], GdFe [18], etc).

## 2.2 Magnetic ordering

Depending on the sign on the exchange coupling  $J$ , the exchange energy can be minimized by either parallel (ferromagnetism (FM)) or anti-parallel (antiferromagnetism (AFM)) alignment of the magnetic moments. This results in three different possibilities of alignment as shown in a simple schematic in Fig. 2.3. For (a), the magnetic moments all lie parallel (ferromagnetism), and the total magnetic moment is the sum of all the moments. In (b) the magnetic moments align antiparallel (antiferromagnetic) such that the total magnetic moment is zero, but each individual atom carries a moment. In (c) the neighbouring magnetic moments are antiparallel as in (b) but they are unequal in size. Therefore, the two spin sublattices do not cancel completely, and the material has non-zero magnetic moment, called *ferrimagnetism*.

CoAlZr is ferromagnetic, where the spins of the cobalt atoms align parallel. In TbCo, the Tb and Co moments align antiparallel. If the

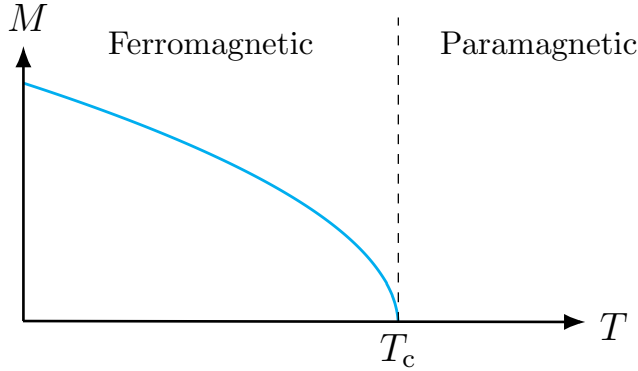


Figure 2.4: Magnetization as a function of temperature with  $\beta = 1/2$ . Below  $T_c$  the sample is a ferromagnet, at the critical temperature  $T = T_c$  the magnetization reduces to zero and all long range order is lost and the material becomes paramagnetic.

magnetic moment of the two sublattices is the same, the total moment of the sample reduces to zero. However, Tb and Co have a large difference in magnetic moment ( $9.36\mu_B$  [15] and  $1.7\mu_B$  [19], respectively, where  $\mu_B$  is the Bohr magneton) and temperature dependence, so the usual configuration of TbCo alloys is ferrimagnetic.

For a ferri- or ferromagnetic body to retain its spontaneous magnetization, the exchange coupling between the atoms has to be stronger than the thermal fluctuations [9]. As the temperature is elevated, the thermal energy of the atoms increases and the alignment of the magnetic moments becomes disrupted. At a high enough temperature, called the critical temperature or Curie temperature, all order is lost, and the spontaneous magnetization drops to zero. This disordered state is called paramagnetic, and although the total magnetization is zero, the atoms have a non-zero moment. By applying a field, the magnetic moments align parallel to the field, but reducing the field to zero will result in disorder and zero magnetization. TM and RE alloys obey the Curie law and display susceptibility that scales inversely with temperature [9].

### 2.2.1 Ordering temperature of ferromagnets

The temperature above which a ferromagnet becomes paramagnetic is called the Curie temperature or critical temperature and is often written as  $T_c$ . The magnetization  $M$  decreases as a function of temperature  $T$ , and



for a ferromagnetic material, it follows a simple power law [20]

$$M \propto M_0 \left(1 - \frac{T}{T_c}\right)^\beta \quad (2.3)$$

where  $M_0$  is the magnetization at absolute zero temperature, and  $\beta$  is the critical exponent. This is shown in Fig. 2.4 with  $\beta = 1/2$ , where the material is paramagnetic above the  $T_c$ , but below  $T_c$  the material will spontaneously magnetize.

The critical temperature is material and thickness [3, 21, 22] dependent, and can, for example, be tuned smoothly by changing the composition in amorphous alloys [23]. In amorphous CoAlZr the critical temperatures and magnetization decrease linearly with decreasing Co content, and below 66% Co content, the alloy is not magnetic at any temperature. This means that even with more than 50% Co content, there is no long-range magnetic ordering. From this it is apparent that removing a Co atom (replacing it with Al or Zr) is not the equivalent of removing one Co atomic moment. If that were the case, then replacing Co with Al or Zr would just lead to a linear decrease of the magnetization ( $1.67\mu_B$  per Co atom), that would cross zero at 0% Co. In fact, when replacing Co with Al or Zr, the effective decrease in moment per cobalt atom is  $4.3\mu_B$ . By substituting with AlZr, the electrons are transferred to the unfilled band of the 3d metal, by removing a cobalt atom decreases the total moment by  $1.67\mu_B$  and then an additional decrease is due to the decrease in moment in neighboring atoms [24]. The linear relationship between the composition and magnetization and critical temperature is discussed in paper III.

The critical temperature of thin films also depends on film thickness. If the thickness of the thin films is close to the spin-spin correlation length,  $T_c$  will shift to lower temperatures. This is referred to as the *finite size effect*. The decrease in  $T_c$  is only observed for thicknesses below 5 nm, but always results in a decrease in magnetization near non-magnetic interfaces (resulting in a magnetically a dead layer) [3].

The temperature dependence of the magnetization in TbCo can also be adjusted by changing the ratio between the Tb and Co atoms. But the two sublattices are coupled antiferromagnetically, resulting in a very different temperature dependence than for ferromagnetic materials.

### 2.2.2 Ordering temperature of ferrimagnets

Similar to FM materials, AFM materials go through a phase transition where the antiferromagnetic alignment is lost. This is called the Néel temperature,  $T_N$ : Above  $T_N$  the material is paramagnetic, and therefore has

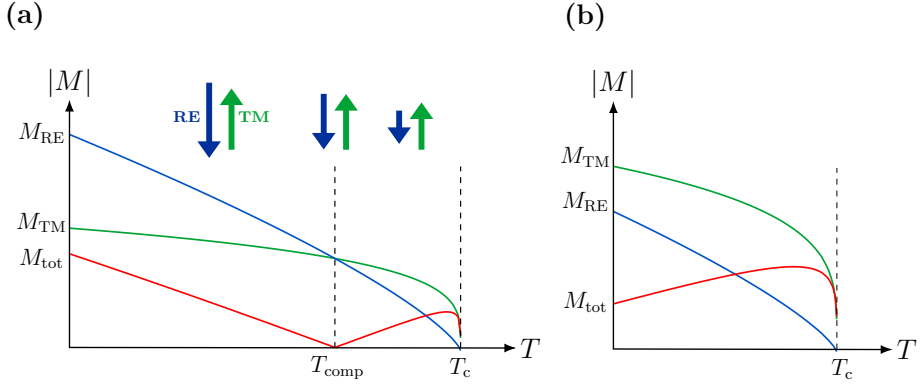


Figure 2.5: The temperature dependence of the magnetization of a ferrimagnetic material for two cases. In (a) the magnetization of the RE element,  $M_{RE}$ , exceeds the magnetization of the TM element,  $M_{TM}$ , at low temperature. There then exists a temperature  $T_{comp}$  where the magnetization of the two sublattices cancels completely, resulting in zero magnetization. The green and blue arrows represent the direction and relative size of the magnetization at different temperature regions. (b) The  $M_{RE}$  is lower than  $M_{TM}$  at all temperatures, so that there is no  $T_{comp}$ .

zero net spontaneous magnetization. Below  $T_N$ , there is antiferromagnetic ordering, and again, zero spontaneous magnetization.

In ferrimagnetic materials, the magnetic moments are antiparallel like for antiferromagnetic materials, but the magnetization is not zero at all temperatures as it is for antiferromagnetic materials. This is due to the difference in magnetic moment and temperature dependence of the two exchange coupled sublattices. The magnetization as a function of temperature is shown in Fig. 2.5 for two cases. Both elements follow the Curie law, depicted by the two green and blue solid lines, the resulting net magnetization  $M_{tot}$  of the alloy is then given by the red solid line in the figures. When the magnetization of the two oppositely aligned lattices is equal, the total magnetization cancels out completely (but still remains ordered), as is shown in Fig. 2.5(a). The temperature where this occurs is called the compensation temperature  $T_{comp}$ . Below  $T_{comp}$ , the net magnetization is dominated by the RE material. Above  $T_{comp}$ , the magnetization is dominated by the TM material.  $T_{comp}$  can be changed by adjusting the composition of the alloy or can be eliminated by choosing the appropriate ratio, as shown in Fig. 2.5(b). Near the critical temperature  $T_c$ , the magnetization of the RE drops quickly to zero, resulting in the unusual *increase* in magnetization as a function of increasing temperature.

$Tb_{20}Co_{78}$  has  $T_{comp}$  around room temperature [25]. For Tb content

around 15%, the two sublattices do not cancel at any temperature, resulting in the temperature dependence shown in Fig. 2.5(b). In the present study, we chose a composition of TbCo where there was no compensation temperature, as an attempt to simplify the temperature dependence of the magnetization. But, it turns out that Co rich TbCo has a complex phase diagram where the direction of the magnetization vector changes as a function of temperature, thickness and composition (This is the topic of paper IV). The directional dependency of the magnetization is called *magnetic anisotropy*, and this is an intrinsic property that is often related to the crystal structure. It determines which direction the spontaneous magnetization aligns with respect to the sample.

## 2.3 Magnetic anisotropy

Magnetic anisotropy refers to the directional dependency of the magnetization vector with respect to the magnetic material. Multiple factors can contribute to the anisotropy of a thin film, for example, exchange interaction,  $E_{\text{ex}}$ , shape anisotropy  $E_{\text{shape}}$ , structural anisotropy (orbital, surface/interface etc.)  $E_{\text{ani}}$ , and magnetoelastic energy  $E_{\lambda}$ . The resulting total energy is the sum of all of these different terms

$$E_{\text{tot}} = E_{\text{ex}} + E_{\text{shape}} + E_{\text{ani}} + E_{\lambda} \quad (2.4)$$

and the resulting anisotropy is therefore determined by the competition between the different energies [26]. In this section, we will discuss the origin of the shape and structural anisotropy, and how the competition between the two determines the anisotropy of thin films.

### 2.3.1 Shape anisotropy

Generally, for a magnetic thin film, the magnetization vector lies in the plane of the film. This is due to the demagnetizing energy, also called shape anisotropy, which arises due to the long range dipole-dipole interactions. The magnetostatic energy arising from the demagnetizing field is given by [9]

$$E_{\text{stray}} = \frac{1}{2} \int_V N M^2 dv \quad (2.5)$$

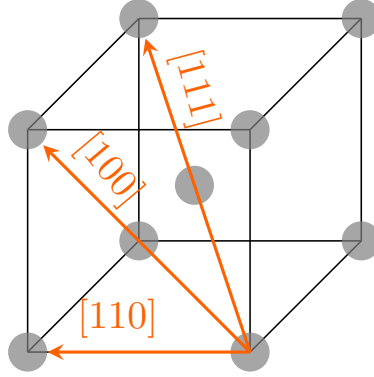


Figure 2.6: Depending on crystal axis, there can be a favorable (easy axis) or unfavorable (hard axis) alignment of the magnetization vector. For bcc iron, the easy and hard axes lie along the  $[100]$  and  $[111]$  directions, respectively.

where  $M$  is the magnetization, and  $N$  is the demagnetizing tensor, which is given by

$$N = \begin{pmatrix} N_x & 0 & 0 \\ 0 & N_y & 0 \\ 0 & 0 & N_z \end{pmatrix}. \quad (2.6)$$

For a thin film, there is no energy cost due to the stray field when the magnetization vector lies in the plane of the film, so that  $N_x = N_y = 0$ . Where as, perpendicular to the film  $N_z = 1$  [cgs units] ( $N_z = 4\pi$  [SI units]). In some cases, the anisotropy is perpendicular to the film plane, and the anisotropy  $K$  has to overcome the stray field energy. For a uniformly magnetized body, the total energy is given by Eq. 2.5,  $E_{\text{stray}} = 4\pi M_{\text{sat}}^2$ . The demagnetizing field therefore often forces the magnetization into the plane of the film, where other factors can induce additional anisotropy terms, such as crystalline order.

### 2.3.2 Magnetocrystalline anisotropy

Magnetocrystalline anisotropy refers to the preferential direction of the magnetization vector in a crystal due to its crystal structure. Fig. 2.6 shows a body centered cubic (bcc) structure, including the three principle axes. The difference in energy cost of aligning the magnetic moments along the  $[100]$  and  $[110]$  crystal directions arises from the interaction of the spin magnetic moment with the crystal lattice, through spin-orbit coupling. When no external magnetic field is applied to the system, the magnetization vector lies along the easy axis. Iron, for example, has a bcc structure, and

its easy axis lies along the [100] direction and hard axis along the [111] direction [9]. Applying an external magnetic field along the hard axis, the spin will try to orient parallel to the field to lower the Zeeman energy. The spin is, by definition, isotropic (no directional dependency), but the orbit of the electron is strongly coupled to the crystal lattice. The crystal lattice will resist the rotation of the spin, and the energy needed to overcome that energy barrier is the magnetocrystalline anisotropy energy. The anisotropy of a crystal is given by a series of directional cosines

$$E = K_0 + K_1(\alpha_1^2\alpha_2^2 + \alpha_2^2\alpha_3^2 + \alpha_3^2\alpha_1^2) + K_2(\dots) \quad (2.7)$$

where  $K_i$  ( $i = 0, 1, 2, \dots$ ), are anisotropy constants and  $\alpha_i$  is the angle between the saturation magnetization and the corresponding crystal axis. Crystals can have one or more easy axes, a material with a single easy axis is called *uni-axial*, and two easy axes are then called biaxial, etc.

In amorphous materials, there is no long range structural ordering, but they can exhibit a large and well defined anisotropy. For example, RE-TM alloys can exhibit a large magnetic anisotropy [17, 25, 27] which arises due to the non-spherical charge cloud of the  $f$  orbital [28–30]. The single ion anisotropy also relies on spin-orbit coupling, where the isotropic spin aligns itself with the external magnetic field while the orbit resists the rotation. This is called *single ion anisotropy*. For example, terbium has a large single ion anisotropy, due to the non-symmetrical  $4f$  charge cloud, compared to gadolinium which has a symmetrical charge cloud, and therefore a small single ion anisotropy.

It has also been shown that the anisotropy in alloys depends on atomic pairs [31]. For example, in TbFe amorphous alloys, there is a difference in in pair correlations between Tb-Tb, Tb-Fe, and Fe-Fe in different directions within the alloy [32]. This directional dependence of the pair correlations is induced by the growth process in a similar way as texture or a preferred orientation develops in polycrystalline films [17]. This results in a directional dependence of the magnetization, again, due to the spin-orbit interaction.

Both TbCo and CoAlZr have uniaxial magnetic anisotropy, but TbCo is a *hard* ferrimagnet with *perpendicular magnetic anisotropy* (PMA) and CoAlZr is a *soft* ferromagnet with *in-plane magnetic anisotropy* (IMA). The terms hard and soft refer to the size of the magnetic field needed to reverse the magnetization along the easy axis. The origin of the induced anisotropy in amorphous films is not fully understood, but the origin of PMA in TbCo has been linked to out-of-plane short-range structural ordering, similar to polycrystalline films [17]. The origin of the uniaxial anisotropy in CoAlZr is unknown, but it is possible to induce uniaxial anisotropy in amorphous thin films by applying a constant magnetic field

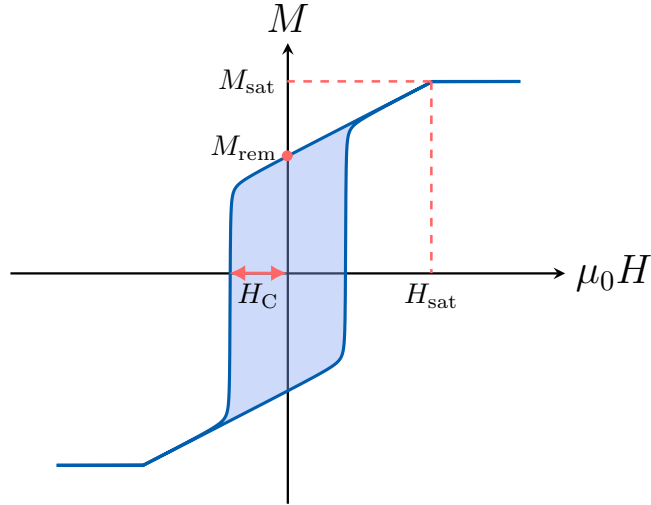


Figure 2.7: A magnetic hysteresis loop, showing the saturation magnetization  $M_{\text{sat}}$ , remanence  $M_{\text{rem}}$ , coercivity  $H_C$ , and saturation field  $H_{\text{sat}}$ .

during growth, texturing with respect to the substrate and more [27, 33–36]. The induced anisotropy in CoAlZr is discussed in detail in Paper III and the corresponding supplementary information.

### 2.3.3 Determining anisotropy in thin films with uniaxial anisotropy

As detailed in the previous section, the direction of the magnetization vector of a magnetic thin film is determined by the lowest energy state. This can be studied by measuring hysteresis loops, which are the response of the material to an external magnetic field. From comparison of hysteresis loops along different directions, we can extract the anisotropy and study magnetic reversal processes. Fig. 2.7 shows an example of a hysteresis loop, including the main parameters extracted from it. The saturation magnetization  $M_{\text{sat}}$  is the total magnetization of the sample (this assumes that the magnetization is fully aligned with the field at the maximum applied field). The magnetic remanence  $M_{\text{rem}}$  is the magnetization at zero external field. Magnetic coercivity  $H_c$  is the magnetic field needed to reverse the magnetization, and the saturation field  $H_{\text{sat}}$  is the field needed to reach  $M_{\text{sat}}$ .

Both CoAlZr and TbCo exhibit uniaxial magnetic anisotropy (UMA), where the easy axis of CoAlZr lies in the plane of the film and for TbCo it lies perpendicular to the plane. For thin films exhibiting UMA, the first

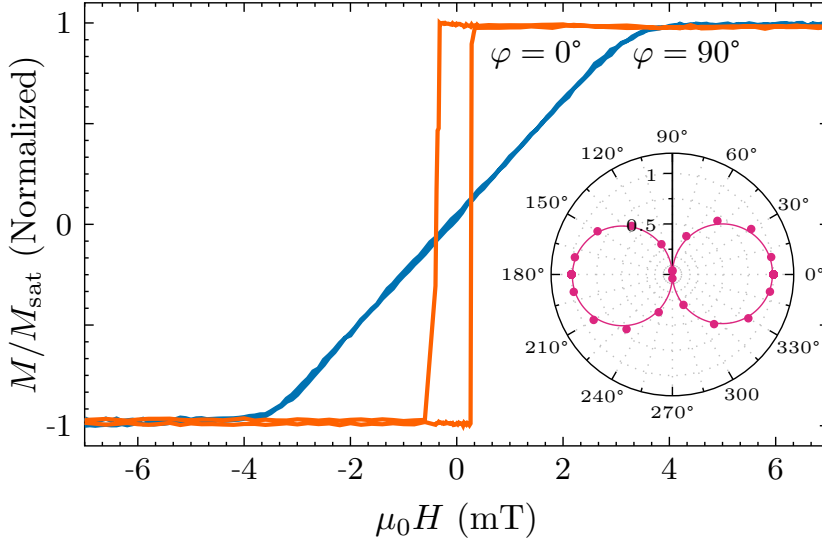


Figure 2.8: Hysteresis loop measured on  $\text{Co}_{90}(\text{AlZr})_{10}$  using MOKE. In the easy axis direction ( $\varphi = 0^\circ$ ) the saturation equals the remanence, with a single abrupt switch. The hard axis ( $\varphi = 90^\circ$ ) is perpendicular to the easy axis, and is dominated by a coherent rotation, with a zero magnetic remanence. Figure adapted from Ref. [37].

order anisotropy energy term can be written as

$$E = K \sin^2 \theta \quad (2.8)$$

where  $K$  is the anisotropy constant and  $\theta$  is the angle between the magnetization and the easy axis. Multiple factors can contribute to the magnetic anisotropy, such as bulk and surface anisotropy, strain, magnetostructural anisotropy, magnetic domains, growth field induced anisotropy, etc. For amorphous thin films, it is especially difficult to determine if there are competing anisotropy terms or not, and we therefore refer to the effective anisotropy constant  $K_{\text{eff}}$  instead of the anisotropy constant  $K$ .

Fig. 2.8 shows two hysteresis loops measured at room temperature, along the easy- and hard axis of  $\text{CoAlZr}$ . This is a magnetic response of a material with a very well defined UMA. Along the easy axis,  $\varphi = 0^\circ$ , the remanence equals the saturation and there is a single abrupt switch at  $\mu_0 H_c \approx 0.2$  mT. In the hard axis direction,  $\varphi = 90^\circ$ , the magnetization reversal takes place by coherent rotation where it reaches saturation at  $\mu_0 H_{\text{sat}} = 4$  mT. The remanence  $M_{\text{rem}}$  can be described by a periodic function

$$M_{\text{rem}} = M_{\text{sat}} |\cos(\varphi + \alpha)| \quad (2.9)$$

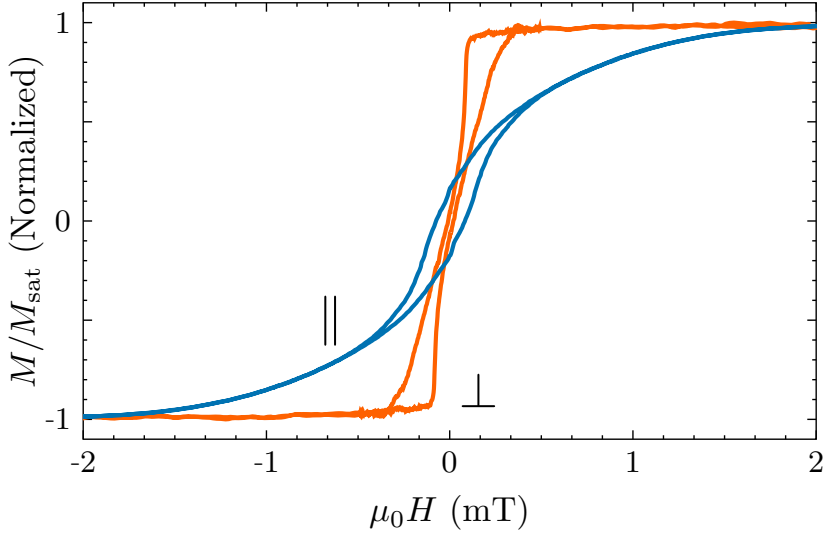


Figure 2.9: Normalized hysteresis loops measured in- and out-of-plane on  $\text{Tb}_{10}\text{Co}_{90}$  at room temperature using VSM. In the out-of-plane direction the hysteresis has zero remanence due to up-down oriented magnetic domains.

where  $\varphi$  is the azimuthal angle and  $\alpha$  is a phase offset. The inset of Fig. 2.8 shows a polar plot of  $M_{\text{rem}}/M_{\text{sat}}$  including a fit using Eq. 2.9. Here the UMA is clear, with  $M_{\text{rem}}/M_{\text{sat}} = 1$  which is separated by  $180^\circ$ .

The effective anisotropy  $K_{\text{eff}}$  is related to the work  $W$  needed to align the magnetization along the hard axis. This can be written as the integral

$$W = \mu_0 \int_0^{M_s} H dM \quad (2.10)$$

where  $H$  is the external field. This integral is the area enclosed between the easy and hard axis loops with the hysteresis averaged. In the case of  $\text{CoAlZr}$ , Eq 2.10 gives the simple result of

$$K_{\text{eff}} = \frac{\mu_0 H_{\text{sat}} M_{\text{sat}}}{2} \quad (2.11)$$

where  $M_{\text{sat}}$  is the saturation magnetization and  $H_{\text{sat}}$  is the saturation field along the hard axis [9, 38]. This result is often used to calculate  $K$  of any material that exhibits UMA, however, using Eq 2.11 directly might give exaggerated values of  $K_{\text{eff}}$ , for example in  $\text{TbCo}$  thin films.

Fig. 2.9 shows two hysteresis loops measured in- and perpendicular to the plane on  $\text{Tb}_{10}\text{Co}_{90}$  at room temperature using VSM. In the in-plane direction, the reversal takes place through coherent rotation. However, in



this case, the magnetization reversal is non-linear in the hard axis direction, and using Eq 2.11 results in roughly two times the size of  $K_{\text{eff}}$  compared to using Eq. 2.10. In the out-of-plane direction, the hysteresis loop shows a drastically different magnetic response compared to the easy axis of the CoAlZr, where the TbCo film has zero remanence and a *bow tie* shaped hysteresis loop. This magnetic response is typical for a material that exhibits magnetic domains. A magnetic domain is a region within the film where the magnetization points in a certain direction. In a film that exhibits PMA they often align perpendicular to the plane, where the uniformly magnetized regions point in alternating up-down directions, such that the magnetization cancels out. The region between the domains is called a domain wall, and within the domain wall, the anisotropy and exchange energy are no longer minimized, and as a result cost energy. This therefore also has an effect on the reversal process and thus the shape of the hysteresis loop, which will be reflected in the effective anisotropy.

The magnetic anisotropy of thin films is elusive and it is very difficult to determine its origin. The measured value of  $K_{\text{eff}}$  can include competition between multiple different factors which results in a single easy axis, although there might be intrinsic anisotropies which point in completely different directions. We observe this in both the CoAlZr and TbCo thin films, where we observe simultaneous substrate and growth field induced anisotropy in CoAlZr and bulk and surface induced anisotropy in TbCo (Paper III and IV, respectively).

### 2.3.4 Surface anisotropy

At surfaces and interfaces, the symmetry of a material is lowered, which modifies the contribution of the anisotropy with respect to the bulk [39]. The lowered symmetry at interfaces can overcome the shape anisotropy, which favours in-plane magnetization, and induce perpendicular magnetic anisotropy in ultra-thin films [40]. This can result in the change in anisotropy direction (spin reorientation) as a function of film thickness due to the competition between the surface and bulk anisotropy [41, 42].

In thin films with competing interface and bulk anisotropy, the effective anisotropy, found using Eq. 2.10, can be written as the sum of the surface,  $K_s$ , and bulk,  $K_v$ , anisotropies

$$K_{\text{eff}} = K_v - \mu_0 M^2 + nK_s/t \quad (2.12)$$

where the first term is due to the demagnetizing field,  $t$  is the total film thickness, and  $n$  refers to the number of (identical) interfaces, which is  $n = 2$  for a single layer film with identical wetting and capping layers.

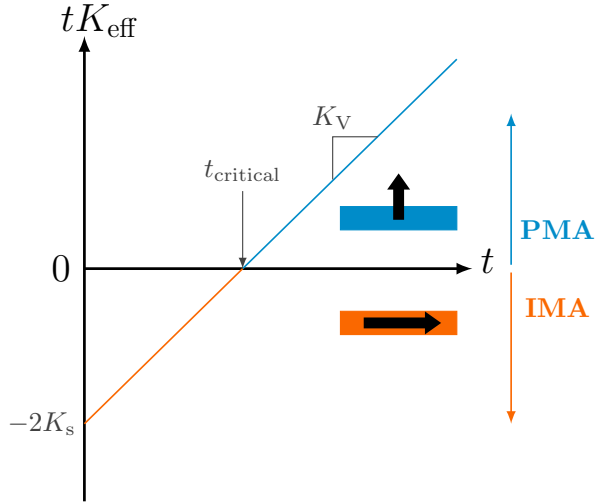


Figure 2.10: A linear relationship between  $tK_{\text{eff}}$  and film thickness  $t$  of a material exhibiting bulk anisotropy. For  $tK_{\text{eff}} < 0$  the film has IMA while  $tK_{\text{eff}} > 0$  has PMA, the crossover between IMA and PMA occurs at the critical thickness  $t_{\text{critical}}$ . The bulk anisotropy can be found from the slope of the line, intercept on the  $y$ -axis gives  $nK_s$ . The direction of the arrows in the inset represent the direction of the magnetization vector with respect to the sample.

Conventionally, a positive  $K_{\text{eff}}$  refers to PMA, and a negative  $K_{\text{eff}}$  refers to IMA. By multiplying Eq. 2.12 by the film thickness  $t$ , we get a linear relationship between  $K_{\text{eff}}t$  and  $t$ , as shown in Fig. 2.10,

$$tK_{\text{eff}} = t(K_v - \mu_0 M^2) + 2K_s \quad (2.13)$$

where the sum of the demagnetizing energy and bulk anisotropy is given by the slope of the line, and the interface anisotropy by the intercept with the  $y$ -axis.

Typically, interfaces contribute to PMA due to the aforementioned symmetry breaking. This can be seen for example in Co/Pt multilayered thin films [43] and many other systems [44–47]. PMA can also be achieved in materials with strong bulk anisotropy (RE-TM alloys) where the bulk has PMA and the surface has IMA [16, 18, 42]. This kind of behaviour will also result in a linear relationship of  $tK_{\text{eff}}$  as a function of  $t$ , but with a positive slope and negative intercept. The critical thickness,  $t_{\text{crit}}$ , there is a crossover between IMA and PMA is given by the intercept through the  $x$ -axis.

TbCo has a rich phase diagram, and we observe a spin reorientation transition (SRT), where the direction of the magnetization vector changes

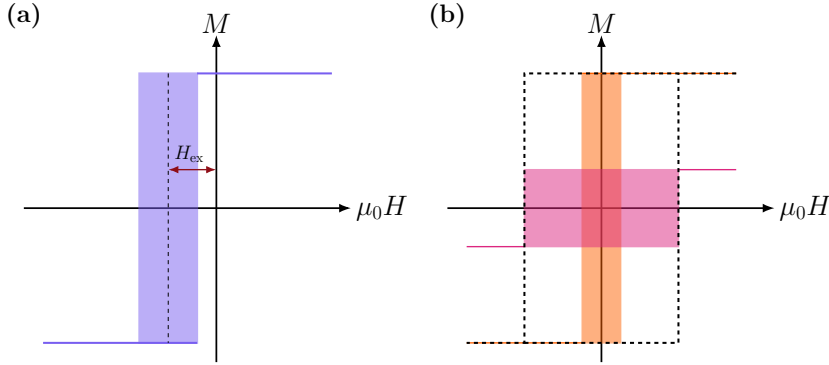


Figure 2.11: **(a)** The hysteresis loop is shifted towards negative field due to the coupling to a AFM layer. The exchange bias is measured as the distance from zero field to the center of the hysteresis loop. **(b)** Hysteresis loop of an exchange spring magnet (black dashed line), where the hysteresis loop acquires the magnetization of a soft layer (orange) but the coercivity of the hard layer (pink).

as a function of thickness, temperature and composition. Using the area method, we find that in Co rich TbCo that  $tK_{\text{eff}}$  scales linearly with thickness  $t$ . The critical thickness  $t_{\text{crit}}$  decreases and the bulk anisotropy  $K_V$  increases with increasing Tb content. This is the topic of paper IV.

## 2.4 Nanolaminates

Various magnetic properties can be brought out in single layer films by alloying together various elements, other properties can be engineered by creating heterostructures with materials of different magnetic hardness, anisotropy or magnetic ordering. In heterostructures, it is possible to obtain properties that are not present in any single layer film. These effects originate at the interfaces, and can give rise to exchange bias, exchange-spring magnets or proximity effects. Exchange coupling between different types of magnetic layers is, for example, an important part of information technology.

Exchange bias often occurs in hard/soft exchange coupled heterostructures, but the most commonly encountered example is when a ferromagnetic layer is exchange coupled to an antiferromagnetic layer [48, 49]. The exchange bias is measured as the shift in the hysteresis curve along the magnetic field axis, as shown with the red arrow in Fig. 2.11(a). Due to the shift in the hysteresis loop, a larger field is required to change the direction of the magnetization than just the coercive field of the bare FM

layer. Exchange bias is therefore often used for pinning of magnetic layers in magnetic sensors or memories [50].

Another manifestation of the exchange coupling in hard/soft layers is the exchange-spring magnet, shown in Fig. 2.11(b). This is a magnetic structure composed of a hard layer with a large anisotropy, which provides a large coercivity, and a soft layer, with a large saturation moment [51–53]. The resulting film has a single phase switching with the large coercivity of the hard layer and high saturation moment of the soft layer, resulting in an increased energy product compared to that of the individual films. Therefore exchange spring-magnets are used as permanent magnets [54]. The thickness of the soft layer to obtain a single switch mechanism, is determined by the strength of the coupling between the hard/soft layers (exchange field), but is typically in the range of 2-10 nm. The switching mechanism can be tuned by changing the thickness or anisotropy of the two layers [53, 55].

The proximity effect refers to an induced magnetization of a paramagnetic material due to the proximity of a magnetic layer [35, 56–58]. It can result in an enhanced ordering temperature [59, 60] or even long-range interlayer exchange coupling through a non-magnetic spacer layer [61]. In crystalline structures, the proximity effect is generally short ranged and the induced magnetization in a non-magnetic layer only extends a few atomic distances from the interface (for example three monolayers in Fe/V structures [56]). But recently, the proximity effect in amorphous materials was shown to be a much longer-range effect, mediating direct exchange coupling over more than an order of magnitude longer distances than for crystalline materials [58]. The induced magnetization was observed up to at least three times the intrinsic ordering temperature of the paramagnetic layer [35]. These results showed that there is great potential for tailoring the magnetic properties of amorphous heterostructures through proximity effects at interfaces. The reasons for such a long-range proximity effect in amorphous alloys are still not clear but the disordered structure of CoAlZr, discussed in paper III, may hold some clues to a possible explanation.

# Chapter 3

## Experimental methods

This chapter gives a summary of the sample fabrication and structure, and the experimental methods used to characterize the samples structurally and magnetically. To characterize the samples structurally, we used x-ray reflection and grazing incidence x-ray diffraction. Magnetic characterization was mainly done using vibrating sample magnetometry and magneto-optic Kerr effect. We also introduce polarized neutron reflectometry, where polarized neutrons are used to probe the depth profile of a magnetic structure.

### 3.1 Sample fabrication

This study relies on the fabrication of amorphous thin film heterostructures with well-defined thicknesses and composition. Magnetron sputtering is the method of choice for such structures as it offers highly controllable growth conditions, growth rate and co-sputtering from multiple sources.

#### 3.1.1 DC magnetron sputtering

Direct current magnetron sputtering is a physical vapor deposition method where the deposition occurs due to the bombardment of high energy ionized gas on to the target material. Fig 3.1(a) shows a schematic of a DC magnetron. To ionize the argon, a large negative voltage is applied between the cathode (magnetron) and anode (shield). The positively charged Ar ions are then accelerated towards the target material where their momentum is transferred to the target. The target atoms can gain enough momentum to be sputtered off the target. To sustain the plasma and increase the ionized Ar, the target is placed on top of a set of magnets. The magnetic field lines then trap the electrons, increasing the probability of collision between the electrons and gas atoms and enhancing the sputter rate. By having two or more magnetrons in the same sputter system, it is possible to create alloys and heterostructures that do not occur naturally, by co-sputtering from

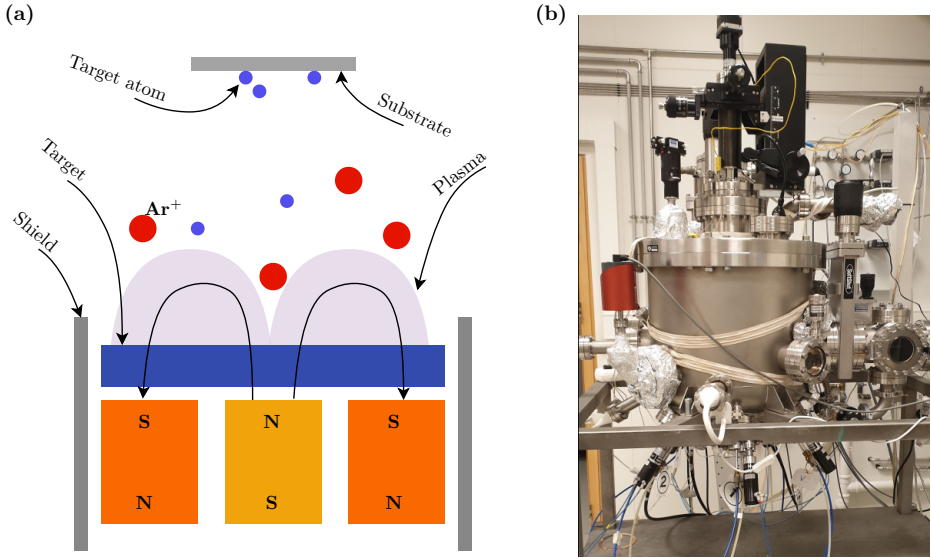


Figure 3.1: **(a)** A schematic of a DC magnetron. To start and maintain the plasma, a negative potential is applied between the shield and target, where the plasma is contained by the stray fields originating from the magnets positioned underneath the target. **(b)** The Dracula sputter system.

multiple targets sequentially and/or simultaneously.

All samples were prepared using dc magnetron sputtering in the Dracula sputtering system, shown in Fig. 3.1(b). The sputter system is an ultra high vacuum (UHV) chamber which reaches a nominal pressure below  $5 \times 10^{-9}$  mbar. It is divided by a gate valve into two chambers, the main chamber and a load lock. The main chamber is equipped with six magnetrons: three 3" and three 2" diameter. Each magnetron is water cooled and has a shutter which can be controlled manually or using a custom built LabView program. The argon pressure is controlled with a 40 sccm mass flow controller and a butterfly valve in front of the turbo pump. Due to the electrical cables connected to the heater, the sample holder rotation is limited to noncontinuous  $\pm 360^\circ$  rotation. By disconnecting the heater cables, it is possible to sputter under continuous rotation. The system is in a confocal geometry with a target-substrate distance of 15.5 cm. The angle between the magnetrons is  $72^\circ$  and they make a  $35^\circ$  angle with the substrate surface. The sixth magnetron is placed directly beneath the sample holder.

Fig. 3.2 shows the custom designed sample holder used during growth to apply a constant magnetic field. Eight SmCo magnets, four on each side, supply a constant magnetic field of 130 mT across the sample.

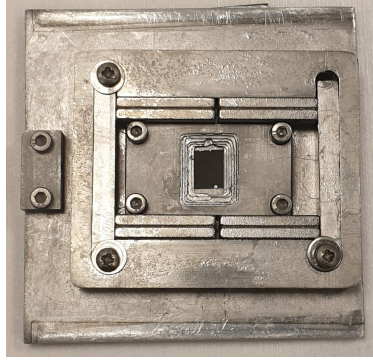


Figure 3.2: The sample holder used during deposition. Eight SmCo magnets provide a uniform magnetic field of 130 mT across the sample surface.

### 3.1.2 Calibration

The magnetic properties of both TbCo and CoAlZr are highly sensitive to composition. This means that during sample deposition, only a small deviation in the growth rate of the elemental targets can result in a drastic change in the magnetic properties of the heterostructures.

The nominal composition of the thin films is estimated by calibrating the growth rate of the elemental targets. The growth rate  $R$ , depends on the material, argon pressure, power applied to the target, size of the target, distance from the target to the substrate, strength of the magnetic field and thickness of the target. As mentioned, the magnetic properties are *very* sensitive to composition, so great care must be taken to eliminate a change in the growth rate as a function of time during the deposition period.

First, a careful calibration should be done on all the targets. This is done by growing samples at various powers for a certain amount of time  $t$  and measuring the thickness of the resulting film. From this we can measure thickness  $d$  per time,  $t$ , per power  $P$ . The growth rate depends linearly on the power applied to the targets and can be written as

$$d/t = RP \quad (3.1)$$

The slope of the linear relationship between  $d/t$  and  $P$  gives the growth rate  $R$  [nm/s·W]. When co-sputtering we sputter from two, or more, targets simultaneously. The nominal composition is then found using the growth rates from the two targets and converting them to atoms per second,  $A$  (atomic flux), for both (all) targets. To convert to  $A$ , we start by multiplying Eq. 3.1 with the density [g/cm<sup>3</sup>],

$$\rho \cdot d/t = w/t \quad [\text{g/cm}^2\text{s}] \quad (3.2)$$

the number of atoms per second per unit area is then given by

$$A = u \cdot N_A \cdot w/s \quad (3.3)$$

where  $u$  is the atomic weight and  $N_A$  is Avogadro's number. The nominal composition,  $x$ , when cosputtering from two targets is then given by

$$x_1 = A_1/(A_1 + A_2) \quad x_2 = A_2/(A_1 + A_2) \quad (3.4)$$

where  $x_1$  and  $x_2$  are the atomic percentage of targets one and two, respectively,

### 3.1.3 Sample structure

All samples are grown at room temperature with base pressure below  $5 \times 10^{-9}$  mbar. During growth the argon pressure was kept at  $(2.5 \pm 0.1) \times 10^{-3}$  mbar. To induce uniaxial magnetic anisotropy in the amorphous alloys, they were grown in a constant magnetic field of 130 mT supplied by 8 SmCo permanent magnets. All samples have a buffer layer of 2 nm and a capping layer of at least 5 nm sputtered from an Al<sub>70</sub>Zr<sub>30</sub> alloy target. A capping layer below 5 nm does not provide enough protection against oxidation, and the films degrade over time. Using a capping layer of 5 nm or thicker results in a stable film that does not show any changes in magnetic or structural properties (up to 6 years). For low substrate roughness, the substrates used for heterostructures were baked prior to growth for 30-60 minutes. Due to the critical temperature of the SmCo magnets used to supply the constant field during growth, substrate heating was limited to 200° C.

To fabricate the films in question, Co and Tb targets and Co and AlZr targets were co-sputtered. When sputtering heterostructures, the shutters were momentarily closed between layers to ensure sharp interfaces. During the growth session, the change in growth rate as a function of sputter time was closely monitored. In the beginning and end of the sputter session, a sample with identical sputter power and sputter time was grown to monitor drift in sputter rate.



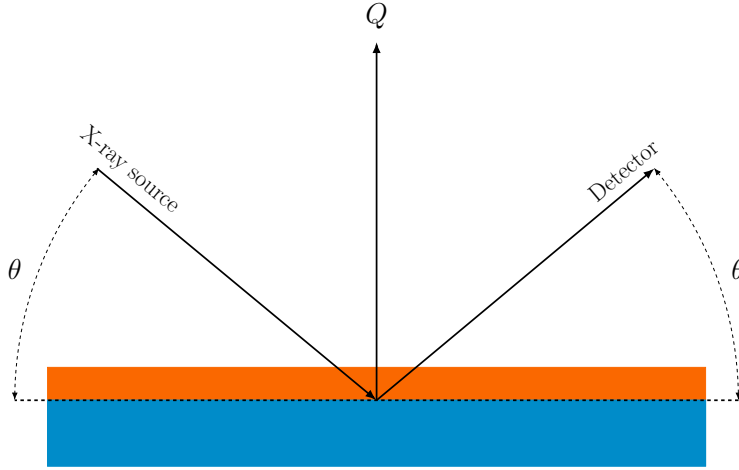


Figure 3.3: A schematic illustration of an XRR setup.

## 3.2 Structural characterization

X-ray reflectometry (XRR) measurements were performed to confirm layer thickness and low interface roughness and fitted using Panalytical X'Pert reflectivity software. The amorphous structure was confirmed with grazing incidence x-ray diffraction (GIXRD) with the incidence angle fixed at  $\omega = 1^\circ$ . All structural characterization was performed using an X'pert Pro diffractometer with Cu  $K_\alpha$  radiation, equipped with a Göbel mirror on the incidence side and a  $0.27^\circ$  parallel plate collimator on the diffracted side. Here we will introduce these two methods, but a detailed description can be found in Ref. [62].

### 3.2.1 X-ray reflectivity

XRR is a surface sensitive structural characterization method where an x-ray beam irradiates the sample at glancing angles, as shown in Fig. 3.3. By measuring the intensity of the reflected beam as a function of  $2\theta$ , where the scattering vector  $Q$  is perpendicular to the surface, the thickness, density and roughness can be measured. An example of an XRR scan is shown in Fig. 3.4, including a fit, using the X'pert Reflectivity fitting software.

The intensity oscillations (Kiessig fringes) are due to destructive and constructive interference of the reflected x-ray beams from the interfaces of the film and substrate. The periodicity of the fringes depends on the total and individual thicknesses of each layer and their density (refractive index). The thickness is estimated from the periodicity of the fringes, roughness

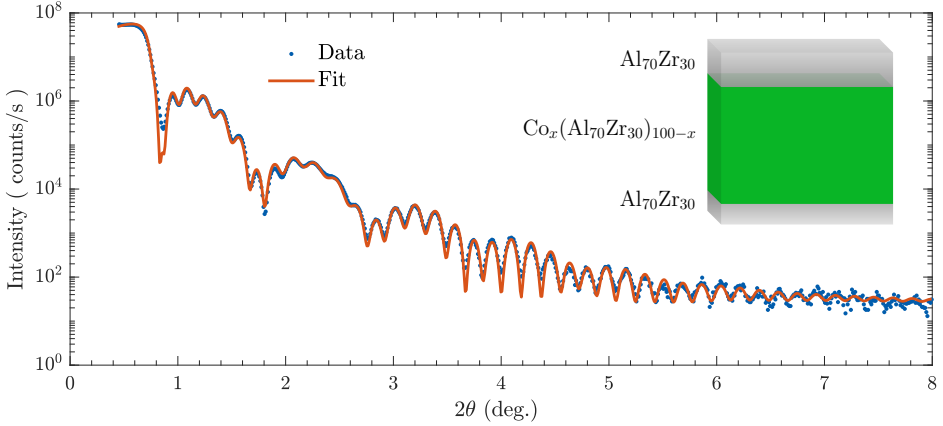


Figure 3.4: An example of an XRR measurement. The drop in intensity at  $2\theta \approx 0.7^\circ$  corresponds to the critical angle  $\theta_c$ . We observe Kiessig fringes up to  $8^\circ$  in this sample, attesting to low interface and surface roughness, typical for high quality amorphous thin films. Figure adapted from Ref. [37].

from the decay of the intensity and density from the critical angle  $\theta_c$ . Below the critical angle we get total external reflection, meaning that the x-ray is fully reflected from the surface. The angle at which the x-ray enters the material,  $\theta_c$ , depends on the material density. The decay of the intensity occurs due to internal scattering caused by roughness of interfaces and absorption, decreasing the intensity of the outgoing beam. Due to the uniform interfaces in the studied amorphous heterostructures, we have a very low roughness ( $<0.5\text{nm}$ ) and we typically observe Kiessig fringes up to  $2\theta$  angles of  $6^\circ$  to  $8^\circ$ .

In multilayered structures the intensity of the reflected beam will be intensified at certain angles corresponding to a periodicity in sample structure. This gives rise to large peaks occurring with a set interval along the  $2\theta$  scan, called Bragg peaks. The position of these peaks is given by Bragg's law

$$\sin(\theta) = \frac{n\lambda}{2\Lambda} \quad (3.5)$$

where  $\lambda$  is the wavelength of the x-ray,  $\Lambda$  is the bilayer thickness and  $n$  is the number of peak. If the thickness of the sample is uniform across the lateral dimensions, the bragg peak will be narrow and well defined. If the thickness varies as a function of lateral dimensions, the Bragg peak will be broadened.

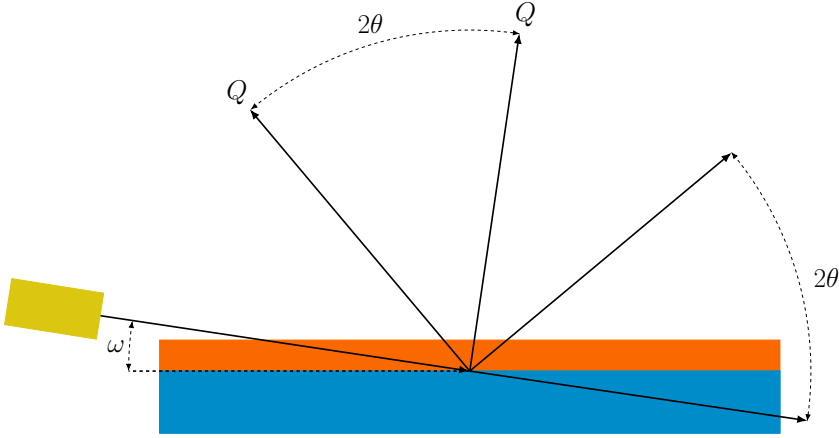


Figure 3.5: A schematic of a GIXRD setup. The incident beam is fixed at an angle  $\omega$  (exaggerated in the schematic for clarity), and the detector is moved by the angle  $2\theta$ . Illuminating the sample at a grazing angle, the volume of the sample that interacts with the beam is increased while suppressing contribution from the substrate, thereby increasing the sensitivity of the measurement. In this case, the scattering vector  $Q$  is not perpendicular to the film plane.

### 3.2.2 Grazing incidence x-ray diffraction

Amorphous materials lack periodic crystal structure and are therefore challenging to characterize structurally. Crystalline materials can be characterized using x-ray diffraction (XRD) which is typically done in a  $\theta - 2\theta$  setup where the scattering vector  $Q$  has a fixed direction throughout the measurement. Depending on the crystal structure, this will give rise to intense scattering at certain angles  $2\theta$  corresponding to the distance between lattice planes which are perpendicular to  $Q$ . Although there is no long-range periodicity in amorphous materials, there is an average distance between the atoms, which can give rise to a broad, low-intensity diffraction peak. A standard  $\theta$ - $2\theta$  XRD measurement is not ideal to detect such a feature in amorphous thin films, first due to the small interaction volume of the incoming x-ray beam and the film and second due to the small signal of the scattering originating from the disordered structure.

In order to show the lack of crystal structure of amorphous thin films a more surface sensitive method is used. Grazing incidence XRD (GIXRD) is done at a small fixed incidence angle while the detector is moved. Fig. 3.5 shows a simple schematic of the GIXRD setup. The incidence angle needs to be small enough for the scan to be surface sensitive, but has to be large enough for the beam to penetrate the sample (above the critical angle). By keeping the incidence angle  $\omega$  constant and only moving the detector over

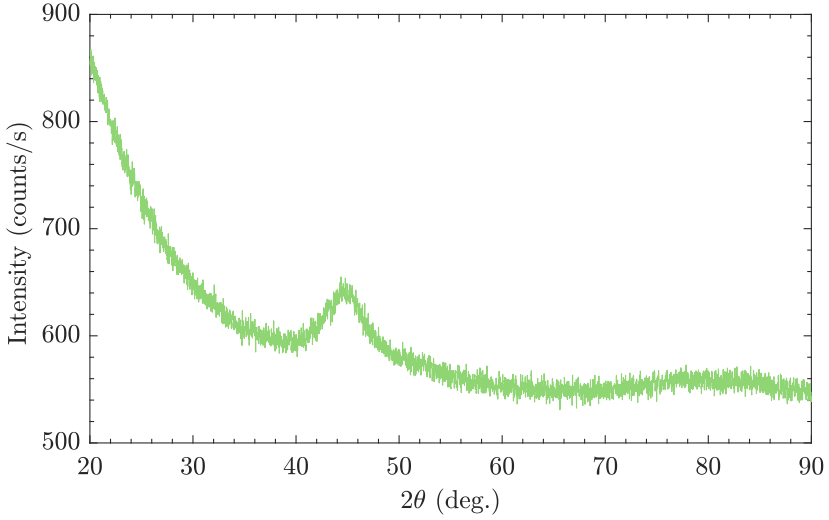


Figure 3.6: GIXRD measurement on amorphous  $\text{Co}_{90}(\text{AlZr})_{10}$  with  $\omega = 1^\circ$  showing a broad peak centered around  $2\theta = 45^\circ$ . A broad, but weak, second order peak can be seen at  $2\theta = 80^\circ$

$2\theta$ , the penetration depth and volume are constant. The incidence beam is spread over a larger area of the sample, therefore the film volume which interacts with the incoming x-ray is larger in contrast to standard XRD.

Additionally, by fixing the incidence angle, the scattering vector  $Q$  is not constant, and changes as a function of  $2\theta$ . As a result, a GIXRD measurement will only show diffraction peaks from structural features which do not have a preferred orientation. This is the case for polycrystalline materials, as they have a random orientations, therefore there will always be an orientation that corresponds to the changing  $Q$  vector. A lack of sharp diffraction peaks in GIXRD measurements is therefore a good indication of an amorphous structure, and this has been confirmed in multiple materials systems by complementary electron diffraction measurements in a transmission electron microscope [27]. Fig 3.6 shows an example of a GIXRD measurement. There is a single broad peak centered around  $2\theta = 45^\circ$ , and a much weaker second order peak at  $2\theta = 80^\circ$ .

### 3.3 Magnetic characterization

The magnetic characterization was done by measuring hysteresis loops at various temperatures and along different directions along the samples. The magneto optical Kerr effect (MOKE) is a very useful tool for obtaining hysteresis loops, as it is very sensitive to small signals (low magnetization) and hysteresis loops can be obtained very quickly (a few seconds or minutes). But MOKE does in general not give the total moment of the material, only the relative size compared to the saturation moment. To obtain the saturation moment, and reach higher fields than obtained in the MOKE, we use a vibrating sample magnetometer (VSM). Neither the MOKE nor the VSM give information on where the magnetization lies in the sample, hence to obtain this we perform polarized neutron reflectometry (PNR) measurements, which give depth resolved information of the magnetization,  $M(z)$ .

In the following sections, we will give a short introduction of these methods and describe details regarding the equipment used for this thesis.

#### 3.3.1 Vibrating sample magnetometry

The vibrating sample magnetometer is the main tool used for magnetic characterization in this study. The VSM operates by vibrating a magnetic sample between a set of conducting pick-up coils at a fixed frequency and amplitude. Due to the vibration, the coils sense a change in the magnetic flux originating from the sample's stray field, which induces a current within them, which is picked up by a lock-in-amplifier. The current is then directly proportional to the total moment of the material, which can be calibrated by measuring the signal from a calibration sample with a known magnetic moment and volume (often an yttrium iron garnet sphere). For more details see for example Ref. [63].

The VSM used here is a Cryogenic Inc. cryogen-free magnet system in a longitudinal setup (pick up coils parallel to applied field) with a maximum field of  $\pm 5$  T, a temperature range of 1.7 K - 325 K, and chamber diameter of 14 mm. The VSM has two modes, high and low field mode. The two modes are controlled by different power supplies, where the low field mode has higher field resolution, but is limited to  $\pm 20$  mT.

Special care should be taken when mounting samples in the VSM, as the position of the samples within the VSM has a drastic effect on the size of the moment. There is also a geometrical effect which arises from the sample shape, and thus the magnetic moment measured in and out of plane can vary slightly.

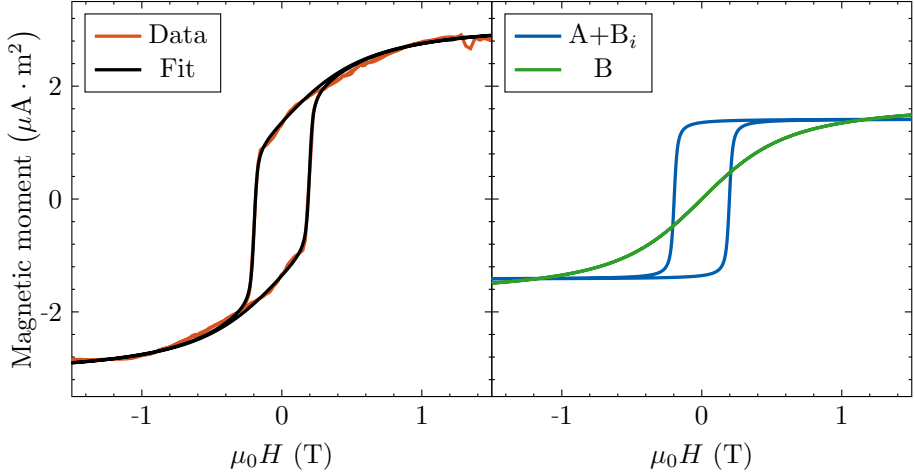


Figure 3.7: Left: Hysteresis loop including a fit using Eq. 3.6. Right: The fit in the left figure is composed of two hysteresis loops, a square loop with a sharp switch and a second S-shaped loop with zero remanence. Figure adapted from Ref. [36].

### 3.3.2 Magneto optical Kerr effect

Magneto optical Kerr effect (MOKE) is a surface sensitive magnetization characterization technique that measures the magnetic properties of materials using the reflection of a laser off the sample surface. The polarization of light can be divided into two parts: longitudinal polarization and transverse polarization, also known as S- and P-polarization. If we shine linearly polarized light onto a magnetic material, the reflected light becomes elliptically polarized. This change in polarization is the basic principle of MOKE.

First a HeNe laser ( $\lambda = 632.8$  nm) passes through a  $\lambda/4$  quartz plate, which polarizes the light. From there, it passes through a photo elastic modulator (PEM), which modulates the light at a frequency of 50 kHz. The laser is then reflected from the surface of the sample, and passes through an analyzer, which is a polarizing filter rotated  $90^\circ$  to the first polarizer, and from there to a Si amplified photodetector. The signal from the detector is passed through a lock-in-amplifier. A hysteresis loop is then recorded by measuring the size of the signal as a function of the applied magnetic field. The MOKE system used here has a maximum field of  $\pm 12$  mT, which is supplied by two Helmholtz coils. The sample can be rotated  $360^\circ$  in the azimuthal angle with respect to the applied field. A MOKE measurement does not give the sample magnetization, and therefore the hysteresis loops measured using MOKE are all normalized, as the amplitude does not carry

any significance. From the hysteresis loops we can then measure the relative change between saturation and remanence, and the coercive and saturation field. This, of course, is only useful if the applied field is large enough to saturate the sample.

### 3.3.3 Fitting hysteresis loops

In composite systems with different magnetic moments and anisotropies, the responses from different components become convoluted in a bulk magnetization measurement. In order to separate the magnetic responses, we fit the hysteresis loops with a sum of modified Langevin functions of the form

$$M = A \left( \frac{1}{\arctan \frac{H \pm H_C}{S}} - \frac{1}{\frac{H \pm H_C}{S}} \right) \quad (3.6)$$

where  $A$  is the saturation moment,  $H_C$  is the coercivity and  $S$  determines the shape of the loop. This equation does not have a theoretical basis, but can capture the parameters of multi-component hysteresis loops.

The red curve in Fig. 3.7(a) shows an example of an hysteresis loop of a TbCo/CoAlZr bilayer, measured using VSM. In this loop we have a single switch and a coherent rotation superimposed, but by fitting the hysteresis loop with two curves with different parameters, we can separate the magnetic responses. The sum of the two calculated loops is fitted to the measured hysteresis loop using the Levenberg Marquard method [64], which is a minimization method based on non-linear least squares problems.

### 3.3.4 Polarized neutron reflectometry

XRR is a powerful tool to study the structural properties of thin film heterostructures, giving the thickness of individual layers, interface roughness and density. The magnetic properties can then be measured with VSM, which give bulk magnetic properties. In many of the structures presented here, the magnetic properties vary dramatically as a function of depth within the sample. Magnetic moments, for example, gradually rotate from an in-plane direction to out-of-plane from top to bottom of the film stack or vice versa. Although bulk measurements can go a long way in characterizing the magnetic profile, a full picture cannot be drawn from analyzing bulk hysteresis loops only.

Polarized neutron reflectometry (PNR) is the perfect method to get a full picture of how the magnetic profile changes as a function of depth. In contrast to x-rays, which interact with the electron density of the material,

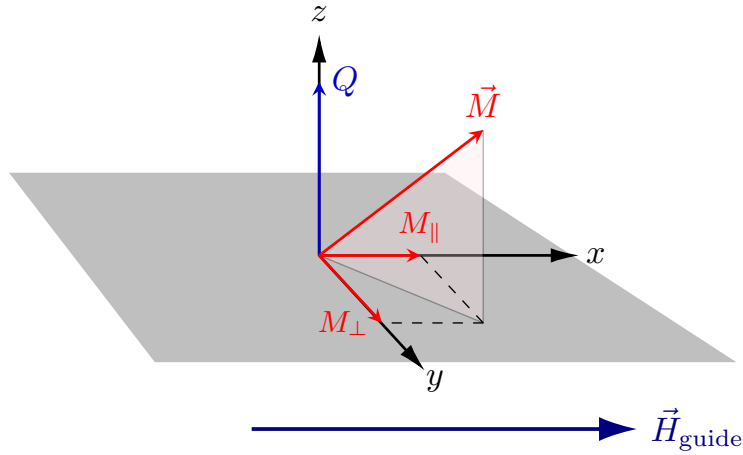


Figure 3.8: A schematic of the scattering geometry for polarized neutron reflectivity. Only the components of the magnetization vector that are perpendicular to  $Q$  contribute to the reflectivity.

the sample is irradiated with a beam of polarized neutrons. The neutrons interact with the atomic nuclei *and* the magnetic moment.

The magnetic moment of the neutrons interacts with the magnetic moment of the sample. By analyzing the spin of the neutron before and after the scattering event, it is possible to construct a three dimensional model of the magnetic profile of the heterostructure. Fig. 3.8 shows a schematic of the scattering geometry of a PNR measurement. The basic principle of PNR is the same as for XRR, i.e. measuring the intensity variations as a function of angle (or the time of flight). The incident neutrons are either polarized (spin) up ( $u$ ) or down ( $d$ ), and the intensity of the out coming neutrons with either spin up or down is detected. Depending on the purpose of the PNR measurement, any combination of the two incoming and two outgoing spin states can be detected, up-up ( $uu$ ), down-down ( $dd$ ), down-up ( $du$ ) or up-down ( $ud$ ).

The only component of the magnetization that will contribute to the scattering is the component of the magnetization which is perpendicular to the wavevector transfer  $Q$ , i.e. the magnetization that lies in the plane of the film. Magnetization that lies perpendicular to the plane is *not* detected by PNR. In the plane, only the component which is parallel to the polarization of the neutrons will contribute to the non-spin flip (NSF) while the transverse component of the magnetization will contribute to the spin-flip (SF) channels.

Let us first consider the  $uu$  and  $dd$  channels (NSF) and the case of



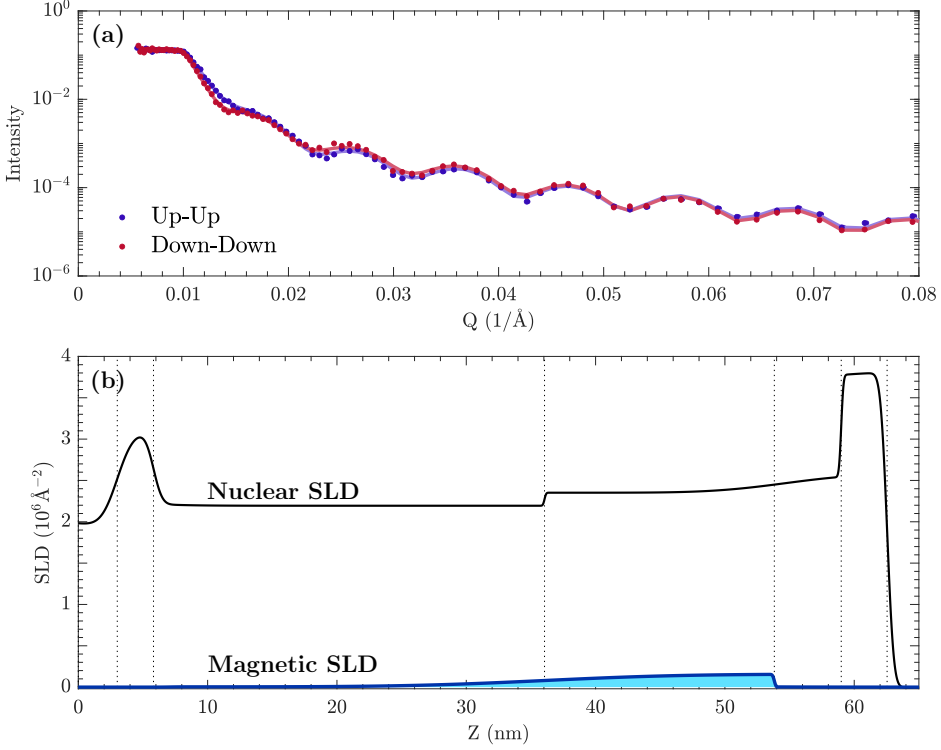


Figure 3.9: **(a)** A polarized neutron reflectivity curve measured on a TbCo/CoAlZr bilayer at remanence (guide field) including a fit (solid line) using Refl1D. **(b)** Both the magnetic and nuclear scattering length densities, mSLD and SLD respectively, that produce the fitted reflectivity curve in (a).

a uniformly magnetized thin film, with the magnetization parallel ( $uu$ ) or anti-parallel ( $dd$ ) to the polarization of the neutrons. Here, the spins will not get flipped during the reflection process, as there is no transverse component of the magnetization,  $M_{\perp}$ . The interaction of the neutrons with the film in the NSP channel can then be described by the Fermi pseudopotential

$$V_{\pm} = \frac{2\pi\hbar}{m} N (b_n \pm b_m) \quad (3.7)$$

where  $m$  is the neutron mass,  $N$  is the atomic density,  $b_n$  and  $b_m$  are the nuclear and magnetic scattering lengths, respectively [65]. The difference between the potentials in the  $uu$  and  $dd$  states then results in a difference in reflectivity curves, and a magnetized sample can be immediately recognized by a splitting at the critical edge. If there is no splitting, the scattering length density (SLD) for both  $uu$  and  $dd$  are the same, which holds true for  $M_{\parallel} = 0$ . If the magnetization lies at an in-plane angle  $\varphi$  to the polarization

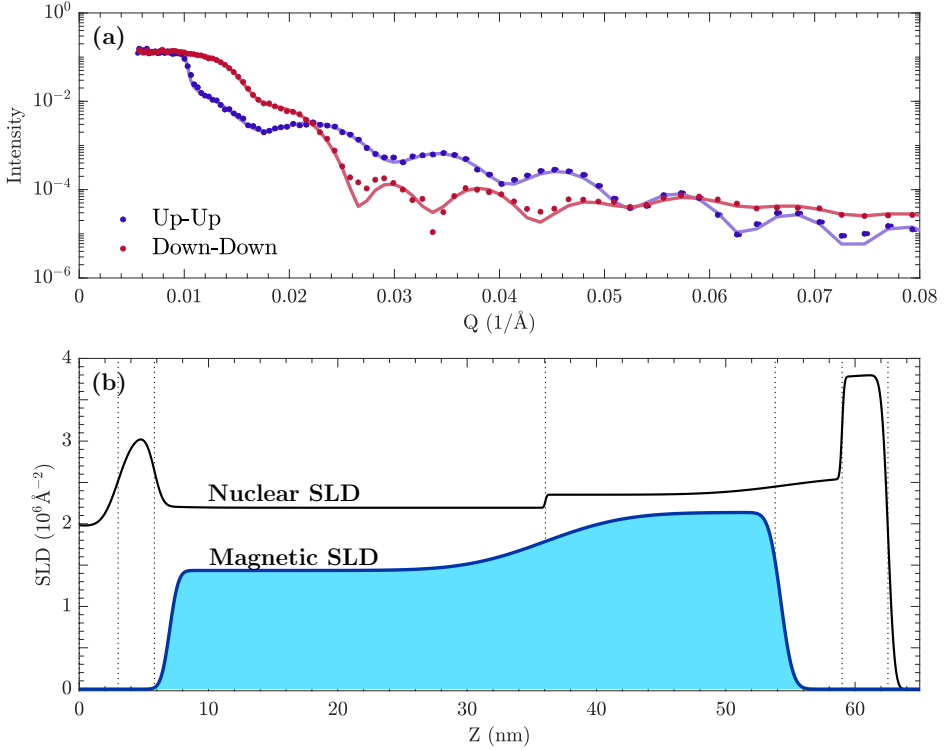


Figure 3.10: **(a)** A PNR reflectivity curve of the same sample as shown in Fig. 3.9 but with an applied in-plane field of 20mT, including a fit using Refl1D(solid line). By applying a field, the size of the magnetization that is parallel to the polarization, which modifies  $b_m$  in Eq. 3.7. **(b)** Both the magnetic and nuclear scattering length densities, mSLD and SLD respectively, Scattering length density that produce the fitted reflectivity curve in (a).

of the neutrons, the spin of the neutrons can flip from one state to another. This is called the spin flip channel, and is used to measure the transverse component of the magnetization. Fig. 3.9 shows reflectivity curves for  $uu$  and  $dd$  spin channels including the scattering length density as a function of depth. The two curves are nearly identical, with only a small splitting at the critical edge. By fitting these curves (using Refl1D), we can extract the SLD as a function of depth, shown in (b), where we can identify the position and size of the magnetization that contributes to the mSLD.

In Fig. 3.10, we have a much larger splitting at the critical edge, and the two channels produce very different reflectivity curves. From the SLD we can now identify a much higher magnetization. The difference between these two measurements is the size of the applied in-plane field. For this particular sample, there is no signal in the spin flip channel. At

remanence, the magnetization vector points perpendicular to the film plane, by applying a field, the magnetization vector is pulled into the plane. Only the projection of  $M$  parallel to the plane contributes to  $b_m$ .

For a thin film where a component of the magnetization is perpendicular to the film plane, the PNR measurement combined with a hysteresis loop, can give a full picture of the magnetic profile. From the hysteresis loop, we can measure the size of the magnetization at certain field values, and at what field the sample saturates. By performing multiple PNR measurements at different fields, all the different reflectivity curves can be fitted simultaneously. By doing this, the structural part can be fixed, and only the magnetic contribution varied.



# Chapter 4

## Competing magnetic anisotropies

Amorphous, or disordered, materials lack the long-range structural ordering which is characteristic of crystalline materials. They nonetheless possess medium-to-short range order, which usually only extends a few atomic distances. Studying these materials remains a challenge, as they can not be described by a single, or a set of unit cells. Instead, it is possible to measure the probability of finding an atom a distance  $r$  from a central atom. This is done by using X-ray scattering and absorption spectroscopy to find the atomic pair distribution function [66–70]. The short range order is very sensitive to composition and results in local variations in magnetic ordering as well as magnetic anisotropy. These effects will be described in the following, for the CoAlZr and TbCo systems.

### 4.1 Order in randomness

Due to the large difference in the atomic sizes of the elements in CoAlZr and TbCo alloys, the composition can be tuned over a very large range without crystallization. Fig. 4.1 shows GIXRD for selected compositions of TbCo and CoAlZr. For CoAlZr, the alloy becomes amorphous below 92% Co and in TbCo, the alloy is amorphous down to at least 8% Tb. In these disordered structures, the distance between the atoms is no longer periodic, which has a direct impact on the exchange constant  $J$ . The exchange constant is the magnetic coupling strength between two neighboring spins as described in section 2.1. By diluting Co with non-magnetic AlZr, the coupling between the cobalt atoms decreases, resulting in a *linear* decrease in the saturation magnetization  $M_{\text{sat}}$  and Curie temperature  $T_c$  as a function of decreasing cobalt content, shown in Fig. 4.2(a). The Curie temperature is determined, from full hysteresis loops, where the magnetic remanence decreases to zero as a function of temperature. Fig. 4.2(b) shows two  $M$  vs  $T$  curves measured on two  $\text{Co}_x(\text{AlZr})_{100-x}$  samples with 70% and 68% Co content. It is measured by cooling the sample down and measuring the magnetization as the sample is heated up, with or without an external field. The two

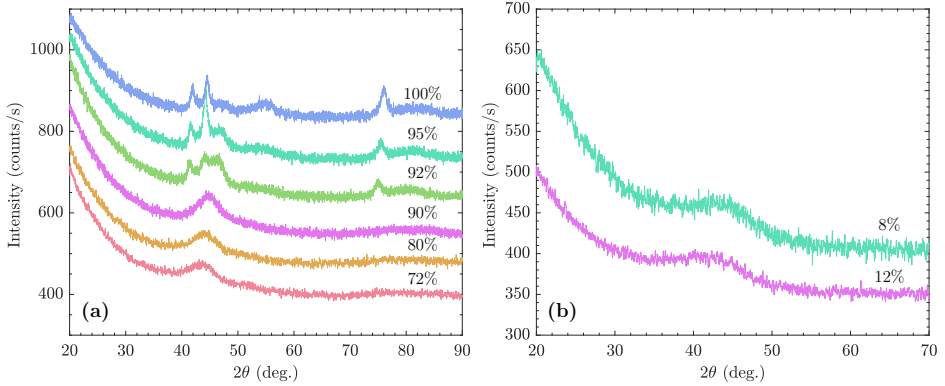


Figure 4.1: Grazing incidence x-ray diffraction measured on several compositions of (a) CoAlZr and (b) TbCo.  $\text{Co}_x(\text{AlZr})_{100-x}$  is amorphous for  $x < 92$  at.% Co. Both datasets show a typical amorphous peak around  $2\theta = 44^\circ$ . Figure (a) adapted from Ref. [37].

curves in Fig. 4.2(b) are measured at  $\mu_0 H = 20$  mT.

In these two samples, the critical temperature *appears* to be well defined, and by decreasing the Co content by just 2%, the critical temperature is reduced by half. A well defined critical temperature means well defined  $J$ , which is **not** the case in amorphous materials. Therefore, the two curves in Fig. 4.2(b) are somewhat misleading and do not give the full extent of the magnetic ordering.

The spin Hamiltonian in Eq. 2.1 assumes that the distance between the nearest neighbor atoms is fixed. According to the Bethe-Slater curve, a constant interatomic distance will lead to a uniform exchange coupling  $J$ . In crystalline materials, this is true. However, this does not hold for amorphous materials, which lack periodic structure. In amorphous materials, the interatomic distance is non-uniform, which leads to a variation in the exchange constant  $J$ . This has an effect on the critical temperature of a magnetic alloy. Furthermore, amorphous materials are not uniform, i.e. there exist regions of high and low density of the magnetic elements. This was shown by Gemma et al. [6] where within FeZr thin films, they found local variations in Fe density. The ordering temperature of a material is determined by the number of and distance to the nearest neighbour. When Fe is alloyed with a non-magnetic material, this number is truncated. From this, it is apparent that within the film there exist regions with a large difference in magnetic coupling strength, and thus temperature dependence of the magnetic coupling. Even though the critical temperature of amorphous alloys is not well defined, they still follow the (modified)

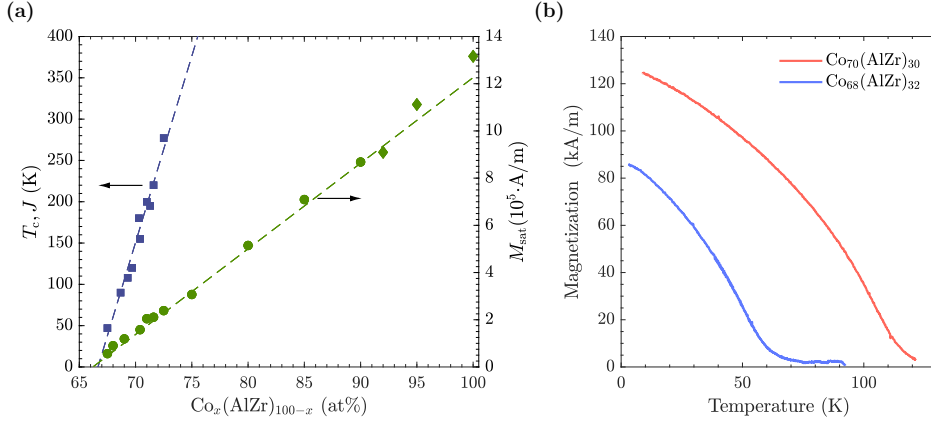


Figure 4.2: **(a)** Critical temperature (Left, blue squares) and saturation magnetization measured at 20 K (Right, green circles) as a function of cobalt composition. **(b)** Magnetization as a function of temperature, measured with applied field of 20 mT, for samples of  $\text{Co}_x(\text{AlZr})_{100-x}$  with  $x = 68$  and 70 % cobalt. Figure (a) adapted from Ref. [37].

power law from Eq. 2.3 of ferromagnetic materials [3, 35, 58].

Above the critical temperature, all long range order is lost, but the film exhibits a very high susceptibility [71]. The high susceptibility is an indicator, that even though a large volume of the film is paramagnetic, there exist regions within the film that are ferromagnetic, suspended in a non-magnetic matrix. These regions align under a very low external field, but the exchange coupling between the regions is too weak for them to remain ferromagnetically aligned when the external field is removed.

How these regions affect the magnetic properties (and electronic, transport, damping etc.) of amorphous materials is far from being fully understood, but systematic and rigorous study of these materials is slowly paving the way to a better understanding. In paper I, we study how a ferromagnetic layer of CoAlZr induces magnetization in an adjacent paramagnetic layer of CoAlZr. This is done by growing multilayers of alternating high and low  $T_c$  layers, shown schematically in Fig. 5.1(a). We find that within the low  $T_c = 100$  K layer, there is a significant proximity induced magnetization, even at room temperature. This showed that within the low  $T_c$  layer there are ferromagnetic regions which are easily polarizable, but do not retain their magnetic ordering in the single layer film.

When making these thin films, we usually apply a constant magnetic field during growth. This induces a uniaxial anisotropy, which tends to simplify analysis and data gathering. To imprint anisotropy with external magnetic field, a strong response of the magnetic material with the magnetic field

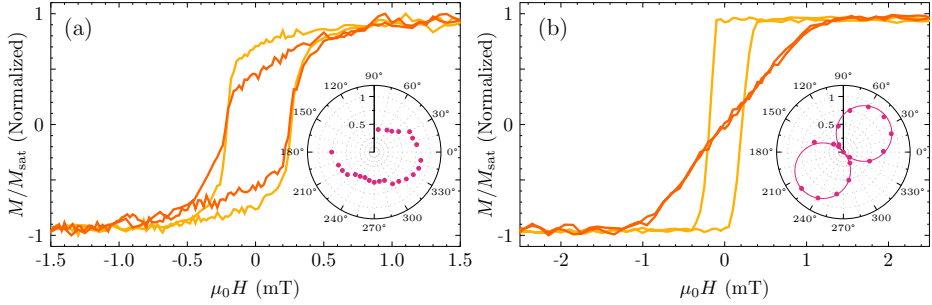


Figure 4.3: Normalized in-plane hysteresis loops measured along two orthogonal axes for  $\text{Co}_{75}(\text{AlZr})_{25}$  grown on (a) thermally oxidized Si (thick  $\text{SiO}_2$ ) and (b) Si(100) with the native oxide. In addition, both films are grown on a 2-nm-thick AlZr buffer layer, through a circular mask without an external magnetic field. Insets: Polar plots of  $M_{\text{rem}}/M_{\text{sat}}$  as a function of the azimuthal angle  $\varphi$ . The film grown on thick  $\text{SiO}_2$  is almost fully isotropic whereas the film grown on the Si(100) with native oxide has a uniaxial anisotropy along the Si[110] in-plane direction. Figure adapted from Ref. [37].

is required, i.e. if the material is not magnetic during growth, it will not interact with the external field. Due to the low  $T_c$  layer being non-magnetic during growth, its anisotropy is unknown, but could be expected to be the same as the high  $T_c$  layer.

To investigate how the field imprinted anisotropy is affected by a lower critical temperature, we grew a series of samples of 40 nm  $\text{Co}_x(\text{AlZr})_{100-x}$  with  $x = 65 - 92\%$  Co. We found that for  $x > 80\%$  Co, the sample was uniaxial with the anisotropy parallel to the growth field. But as we decreased the Co content, we measured a smooth rotation of the easy axis *away* from the applied field.

A decrease in cobalt content resulted in what appeared to be a weaker interaction with the external field. To determine where the easy axis was headed, we repeated the series except without any external field, and we found that all samples had uniaxial anisotropy along the Si[110] substrate direction. We could then eliminate the anisotropy induced by the substrate by growing samples through a circular shadow mask, with constant rotation during growth, and on a thick thermally oxidized  $\text{SiO}_2$  buffer layer. Fig. 4.3(a) and (b) shows two hysteresis loops measured on two samples, grown at the same time. Fig. 4.3(a) is grown on thick  $\text{SiO}_2$  and (b) on thin  $\text{SiO}_2$ . We therefore concluded that in the absence of any external field, the anisotropy is dictated by the Si[110] direction of the Si(100) substrate, which is angled  $45^\circ$  from the applied growth field.

We can then determine, that the anomalous rotation of the easy axis is



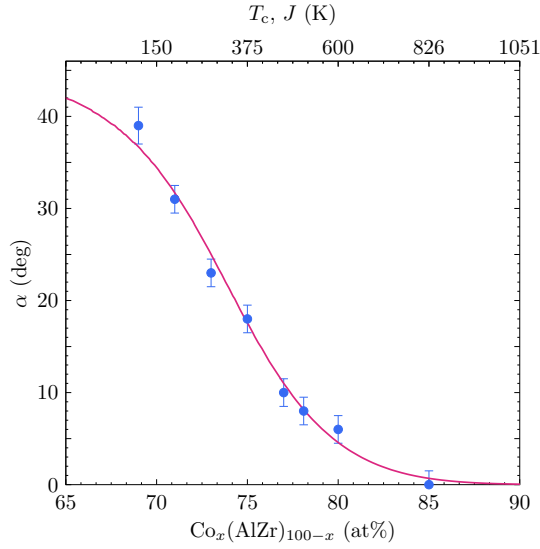


Figure 4.4: The angle  $\alpha$  between the applied field and the easy axis, as a function of cobalt composition. For high Co content, the easy axis is aligned with the growth field whereas for low Co content it is aligned with the Si substrate [110] direction. Figure adapted from Ref. [37].

approaching the Si[110] direction, as shown in Fig 4.4. But the question remains, why does the easy axis rotate smoothly as a function of cobalt content? If the critical temperature was as well defined as shown in Fig. 4.2, we would expect the anisotropy to align with the applied growth field, down to a certain Co composition. And let's say, for arguments sake, that because the samples are deposited at room temperature, that the temperature of the sample surface is also room temperature. Then the composition with  $T_c$  above room temperature will align with the field, whereas a composition with  $T_c$  below room temperature will align with the substrate. Instead, we get a smooth transition. This is a clear sign of a distribution in ordering temperature, which extends over a very large range.

Materials with two competing uniaxial anisotropy axes will in general not exhibit two superimposed anisotropies, but a single anisotropy axis, where the direction is dictated by the competition between the two anisotropies. The anomalous rotation is therefore the competition between two anisotropies, one dictated by the substrate and one by the external field. By decreasing the cobalt content, the strength of the substrate anisotropy increases and the field anisotropy decreases, causing it to shift. The total

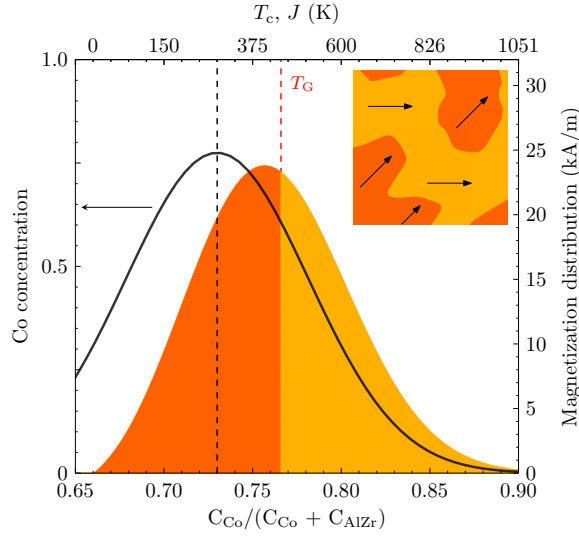


Figure 4.5: The Co concentration (black line) and magnetization distributions (orange-yellow shaded region) for the sample with  $x = 73\%$ . The area under the curve corresponds to the total magnetization of the sample. At temperatures above  $T_G$  (yellow area) the magnetization interacts with the growth field and below  $T_G$  it follows the substrate. The inset is an illustration of the regions with competing anisotropy axes. We find that the effective growth temperature is  $T_G = (450 \pm 90)$  K and  $\sigma = (5.1 \pm 0.8)$  at%. Figure adapted from Ref. [37].

anisotropy energy can be written as the sum of those two anisotropies,

$$E_{\text{total}} = H_{\text{sat}} M_A \sin^2(\pi/4 - \alpha) + H_{\text{sat}} M_B \sin^2(\alpha) \quad (4.1)$$

where  $M_A$  is the total magnetization that is aligned with the substrate, and  $M_B$  is the magnetization aligned with the applied field. Growing the samples with or without external field does not affect the saturation field, and it therefore cancels out (more details on this in the Supplementary information in paper IV). By differentiating the total energy with respect to  $\alpha$ , we can solve for  $\alpha$  and get

$$\alpha = \frac{1}{2} \arctan \frac{M_B}{M_A} \quad (4.2)$$

where  $\alpha$  is the direction of the anisotropy axis. The anisotropy is then a competition between  $M_A$  and  $M_B$ . A distribution in ordering temperature is directly related to a distribution in  $J$ , which is related to the compositional variation. We describe the compositional variation with a Gaussian function, shown with the solid black line in Fig. 4.5. The distribution of magnetization

can then be described by the Gaussian function multiplied by  $M(x)$ , which is given by the linear fit from Fig. 4.2(a). This gives the solid curve in Fig. 4.5. The area above the *effective growth temperature*,  $T_G$ , will align with the external magnetic field, while the areas below  $T_G$  will align with the substrate. By changing the composition, you are shifting the peak of the curve. The  $T_G$  determines the horizontal position of the fit in Fig. 4.5, and the slope of the line is given by the standard deviation,  $\sigma$ , of the Gaussian distribution. We can therefore determine the the distribution of the cobalt composition from the angle  $\alpha$  using Eq. 4.2, from the partial magnetizations given by the gaussian distribution. The solid line in Fig. 4.4 is calculated from Eq. 4.2, and we get a standard deviation of  $\sigma = (5.1 \pm 0.8)$  at.% Co and  $T_G = (450 \pm 90)$  K. These results are the topic of paper III.

From this we can deduce that due to the compositional variations of the amorphous magnet, we can define a local critical temperature which can span several hundreds of kelvin. And the "well defined" Curie temperature corresponds to the *mean value of the exchange constant*. Within the alloy, there is some median or most probable radial distance/orientation between the atoms, this distance/angle will have a certain exchange constant  $J$ , which we can relate to a certain global critical temperature  $T_c$ . Above this temperature, *most* of the sample will become paramagnetic, but we can still define regions that have a critical temperature above  $T_c$ . Those regions are suspended in a non-magnetic matrix and do not align ferromagnetically. However, they do polarize easily in the proximity of a magnetic layer, as we demonstrated with the multilayered structure.

In Paper III, we lightly discuss the "growth temperature". The samples were grown at room temperature, but from our fit we get a "growth temperature" much higher than 300 K. We interpret this to be the temperature at which the atoms condense at the sample surface. Perhaps this growth temperature can be changed by increasing or decreasing the sputter power, changing the kinetic energy of the atoms as they condense at the substrate surface, and thereby affecting the distribution of the Co. We attempted to affect this temperature, but found that CoAlZr crystallizes at the low temperature of 400-450 K, so increasing the substrate temperature to investigate how this would affect the regions was futile. Instead it might be of interest to examine if different growth powers could affect this (or even substrate cooling).

It is an open questions as to how these competing regions transfer to other materials, and if the same applies to other systems, for example TbCo. TbCo also exhibits competing anisotropies, but they manifest in quite a different way than for CoAlZr. TbCo has a very large perpendicular

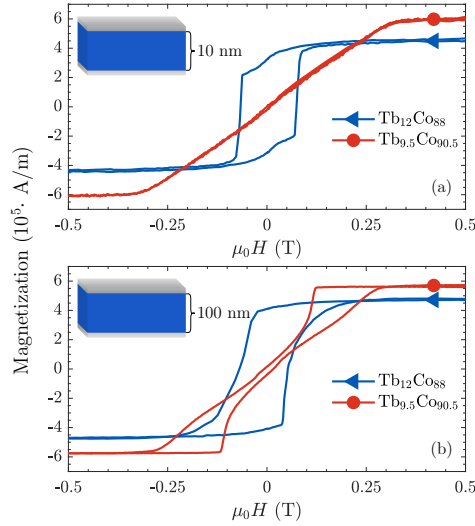


Figure 4.6: Hysteresis loops measured on two samples of **(a)** 10 nm and **(b)** 100 nm Tb<sub>x</sub>Co<sub>100-x</sub> with  $x = 9.5$  and 12%. Figure adapted from Ref. [72].

magnetic anisotropy and an antiparallel magnetic alignment of the Tb-Co atoms. The very large anisotropy is due to the highly anisotropic  $4f$  orbital of the Tb atoms, but the perpendicular magnetic anisotropy has been attributed to out-of-plane texturing [32]. The large PMA makes the TbCo a very popular alloy to work with, as the ferrimagnetic alignment makes it ideal for all-optical switching and the compensation temperature makes it ideal for spin-orbit torque devices.

To study the exchange coupling between TbCo/CoAlZr hybrid structures, we chose to use Co rich TbCo to avoid having a compensation temperature (magnetization of the two sublattices cancel out). This was done to simplify the temperature dependence of the magnetization. Instead, we found that Co rich TbCo has a very complex magnetic phase diagram, where the magnetic properties are highly sensitive to thickness, composition and temperature. This again shows that the magnetic properties of amorphous thin films are highly dependant on the composition, and only a small shift in the *mean* composition has a drastic effect on the global properties.

## 4.2 Magnetic phase diagram of TbCo

TbCo is an amorphous ferrimagnet, which can for certain thicknesses and compositions exhibit perpendicular magnetic anisotropy. It has also been reported that a certain composition and thickness limit,  $t_{\text{crit}}$ , is needed

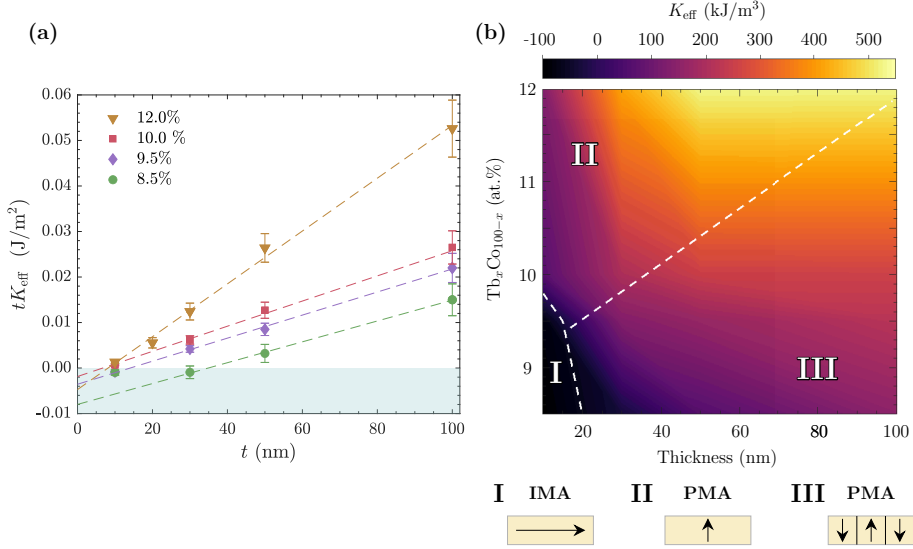


Figure 4.7: **(a)**  $tK_{\text{eff}}$  as a function of thickness  $t$  according to Eq. 2.12. **(b)** Effective anisotropy as a function of thickness and composition.  $K_{\text{eff}} < 0$  has in-plane magnetic anisotropy while  $K_{\text{eff}} > 0$  has perpendicular magnetic anisotropy. Figure adapted from Ref. [72].

for the PMA to appear [16, 73–77]. This is not surprising, as the PMA in TbCo is due to bulk anisotropy, so a certain thickness is needed before the anisotropy can overcome the demagnetizing field. Fig. 4.6(a) shows two hysteresis loops for two compositions of 10 nm Tb<sub>x</sub>Co<sub>100-x</sub>, with 12% and 9.5% Tb. The sample with 12% Tb has a well defined PMA. By decreasing the Tb content by 2.5% results in the loss of the PMA. The PMA can be recovered in the sample with 9.5% Tb by increasing its thickness. Fig. 4.6(b) shows hysteresis loops measured on 100 nm TbCo with the same compositions. Now both samples exhibit perpendicular magnetic anisotropy - although one is uniformly magnetized while the other is in a multi domain state.

The increase in anisotropy with respect to thickness is an indication that there are competing anisotropy terms: one in-plane and the other perpendicular. The anisotropy is then effectively a sum of two terms: bulk anisotropy  $K_v$  and surface anisotropy  $K_s$ . The effective anisotropy,  $K_{\text{eff}}$ , can then be written as

$$tK_{\text{eff}} = tK_v + 2K_s \quad (4.3)$$

as shown in section 2.3.3. To study how the anisotropy changes with composition, we made a series of samples for several different compositions and thicknesses. Fig. 4.7(a) shows  $tK_{\text{eff}}$  as a function of  $t$  for several

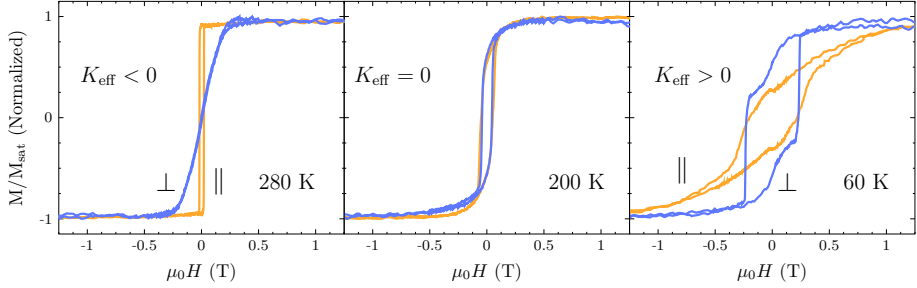


Figure 4.8: Hysteresis loops measured on 10 nm  $\text{Tb}_{9.5}\text{Co}_{90.5}$  at 60, 200 and 280 K. At 60 K the sample exhibits PMA with coercive field  $\approx 250\text{mT}$ , as the temperature is increased the magnetostatic energy increases with decreasing  $K_{\text{eff}}$ . At 200 K the hysteresis loops in and out-of-plane are identical, above 200 K the sample no longer exhibits any PMA and the magnetization vector has fully rotated into the plane with a single switch hysteresis loop in plane and S-shape loop out-of-plane with zero remanence. Figure adapted from Ref. [72].

compositions. We find that  $tK_{\text{eff}}$  scales linearly with thickness  $t$  in all cases, where the bulk anisotropy,  $K_v$  (slope), increases as a function of increasing Tb. The critical thickness,  $t_{\text{crit}}$  (intersect through  $x$ -axis), decreases with increasing Tb content. This shows that at the Co rich limit of TbCo, the magnetostatic energy, interface anisotropy and bulk anisotropy are all at equal strength, leading to a rich "phase diagram". These results are summarized in Fig. 4.7(b), showing a contour plot of the effective anisotropy  $K_{\text{eff}}$  as a function of composition and thickness. Here we can define three different regions in the figure: (I) Samples that exhibit in-plane anisotropy, (II) Samples with perpendicular magnetic anisotropy with uniform magnetization (single domain) (III) Perpendicular magnetic anisotropy with multiple domains.

Lowering the temperature causes  $K_{\text{eff}}$  to increase linearly for all samples [78]. At 20 K all samples are *uniformly perpendicularly magnetized*. Samples that have IMA at room temperature go through a spin-reorientation transition (SRT) at a certain temperature which depends on thickness and composition. A SRT is the change in the direction of the magnetization vector as a function of temperature, thickness or composition [42]. Fig. 4.8 shows in- and out-of-plane hysteresis loops, measured at 60 K, 200 K and 280 K on 10 nm  $\text{Tb}_{9.5}\text{Co}_{90.5}$ . At 60 K the film has PMA with coercivity of 250 mT and in-plane saturation field of 1 T. Increasing the temperature causes the saturation field and coercivity to decrease, until at  $T = 200\text{ K}$  when the two directions are indistinguishable, i.e. the sample is isotropic. Above 200 K the anisotropy of the film has evolved into IMA. The in-plane hysteresis loop has low coercivity and a single switch, and the out-of-plane

hysteresis loop has zero remanence and saturation field of 250 mT. The SRT temperature increases with thickness and composition, and can be tuned to go through the SRT at room temperature (not shown).





# Chapter 5

## Hybrid structures

We have demonstrated that the compositional variations in CoAlZr lead to an extremely large variation of the exchange coupling strength, and therefore critical temperature, within the CoAlZr layers. We have also shown that the magnetic properties of TbCo are highly composition and thickness dependent. The magnetic properties can be further enhanced and altered by layering materials with different properties. Due to uniform interfaces and the lack of lattice mismatch amorphous materials make excellent candidates for magnetic heterostructures. The interlayer exchange coupling between magnetic layers brings out properties that do not exist in single layer films. This includes the long-range magnetic interactions [58] and tunable exchange stiffness [79] in an amorphous spring-magnet.

The following chapter is divided into two sections, as we focus on two types of systems: First, CoAlZr multilayers of alternating high- and low- $T_c$  layers, where we explore the long-range magnetic proximity effect in a paramagnetic (low- $T_c$ ) CoAlZr layer due to the proximity of a ferromagnetic (high- $T_c$ ) CoAlZr layer. Second, we investigate bilayers of TbCo/CoAlZr, where the two layers have crossed perpendicular and in-plane magnetic anisotropy.

### 5.1 Giant magnetic proximity effect

In Ref.[58], it was shown that a 40-nm-thick paramagnetic CoAlZr layer ( $T_c = 105\text{ K}$ ), sandwiched between two ferromagnetic layers, could mediate exchange coupling between the two ferromagnetic layers at room temperature, which is three times its intrinsic ordering temperature. They found that there were two distinct coupling regimes: below and above the  $T_c$ . To gain further insight into the proximity induced magnetization of amorphous alloys, we made a series of multilayered samples of alternating high and low  $T_c$  layers. The multilayer in Fig. 5.1(a) shows a schematic of the sample structure and the magnetization profile at 20 K. Layer A has a high critical temperature (around 800 K) and layer B has a critical

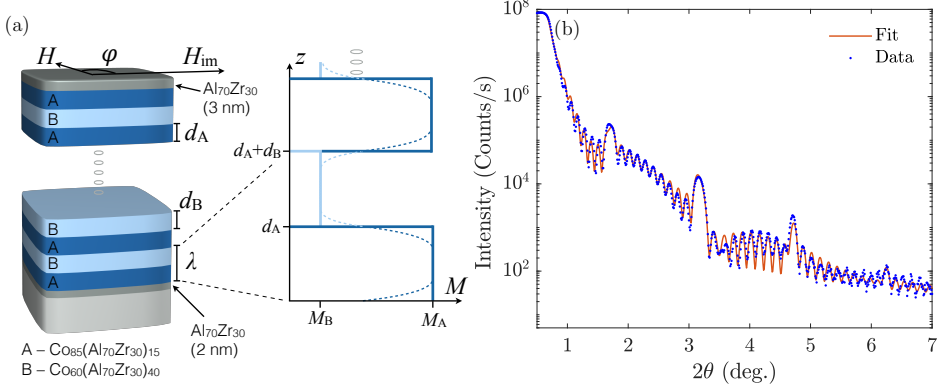


Figure 5.1: **(a)** A schematic of the sample structure (left) and an illustration of the magnetization profile below the critical temperature of layer B. **(b)** XRR measurement, including a fit, on sample with  $d_B = 5$  nm and  $d_A = 1$  nm, showing a well defined peak arising due to the periodicity in the sample structure. Figure adapted from Ref. [35].

temperature of 105 K. To investigate the extent of the proximity effect, we made a series of samples with the thickness of layer A fixed at  $d_A = 5$  nm and B varied between  $d_B = 2.5$  to 10 nm.

We can write the total magnetization of the samples as the weighted average of the magnetization

$$M_{\text{avg}} = d_A(M_A - M_B)\frac{1}{\lambda} + M_B \quad (5.1)$$

where  $M_{\text{avg}}$  is the average saturation magnetization,  $\lambda$  is the bilayer thickness, and  $M_A$  and  $M_B$  is the magnetization corresponding to layers A and B, respectively. If there is no proximity induced magnetization, then the magnetization will scale linearly as a function of  $1/\lambda$  and the intercept at the  $y$ -axis will be positive below  $T_c^B$  and zero above  $T_c^B$ . Fig. 5.2(a) shows the magnetization as a function of  $1/\lambda$  for several temperatures, both below and above the critical temperature. Strikingly, the intercept never goes to zero, even at 300 K. This showed that there is a proximity induced magnetization at three times the intrinsic ordering temperature of the low- $T_c$  layer. This proximity induced magnetization does not appear to decay as a function of distance from the interfaces, attested by the linear dependence of  $M_{\text{avg}}$  as a function of  $1/\lambda$ . The intercept through the  $y$ -axis in the linear fit in Fig. 5.2(a) then gives information about the size of the magnetization in layer B. This is shown in Fig. 5.2(b) as a function of temperature. The magnetization decreases as a function of increasing temperature, but is non-zero over the entire studied temperature range.

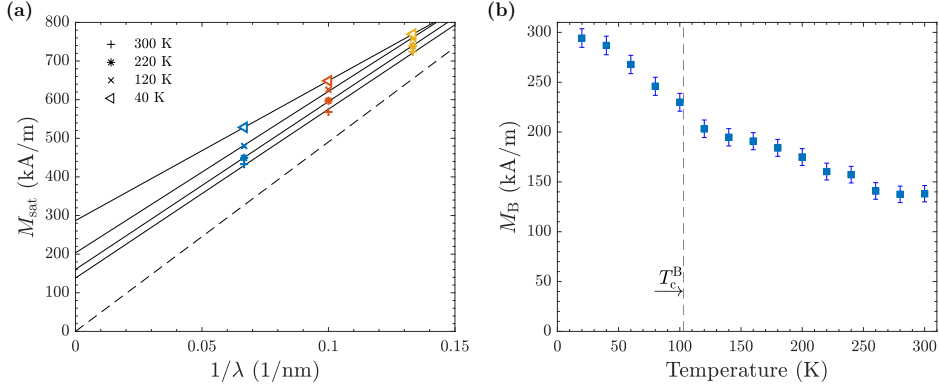


Figure 5.2: **(a)** The saturation magnetization as a function of inverse bilayer thickness for several temperatures, both above and below  $T_c^B$ . The solid lines are fitted to the data, and the dashed line is calculated according to Eq. 5.1 with  $M_B = 0$ . **(b)** The intercept from the linear fit from **(a)** as a function of temperature, which corresponds to the magnetization of layer B, according to Eq. 5.1. Figure adapted from Ref. [35].

However, there is a critical point in the curve at a temperature somewhat above  $T_B$  reminiscent of the ferromagnetic to paramagnetic phase transition. This shows the dual impact of the magnetic proximity effect; first, it enhances the ordering temperature of the B layer and, second, it induces a new magnetically ordered state with a very large extension, which survives to much higher temperatures.

## 5.2 Exchange spring magnets

In the hybrid amorphous structures discussed in the previous section, as well as in Refs. [33, 58, 79, 80], the magnetic anisotropy always lies in the plane of the film. It is therefore interesting to examine coupling between amorphous magnetic layers with crossed magnetic anisotropies, in- and perpendicular to the plane. The exchange-spring behaviour and the extent and type of induced magnetization is unknown, as well as what effect this has on the imprinted magnetic anisotropy.

To study the exchange coupling in TbCo/CoAlZr hybrid structures, shown schematically in Figure 5.3(a), we prepared a series of samples with a fixed TbCo thickness and varying the thickness of the CoAlZr between 5–80 nm. The CoAlZr has a small, but well defined IMA, while the TbCo has a large PMA. We chose to use Co rich TbCo, with 9.5 Tb at%, to avoid having a compensation temperature, where the magnetization of the two sublattices cancels out. By fixing the thickness of the TbCo layer, and

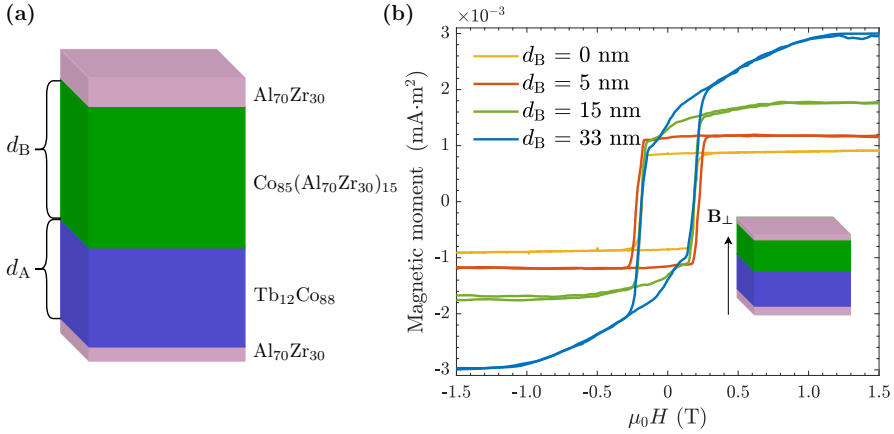


Figure 5.3: **(a)** Schematic of the sample structure. The thickness of the TbCo layer is fixed at  $d_A = 30$  nm and the thickness of the CoAlZr layer is varied from  $d_B = 5 - 80$  nm. **(b)** Hysteresis loops measured out-of-plane at 20 K using VSM. Figure adapted from Ref. [36].

varying the thickness of the CoAlZr layer, we can study how the exchange coupling decays with distance from the TbCo interface.

Fig. 5.3(b) shows out-of-plane hysteresis loops for several thicknesses of CoAlZr, including a single 30 nm TbCo layer as a reference, measured at 20 K. The reference layer has a single switch and the remanence equals the saturation moment. With increasing thickness of the CoAlZr, the out-of-plane response gradually evolves from the square response characteristic of a PMA material to a mixed easy and hard axes response. But, notably for 5 nm CoAlZr there is no hard axis response, and the *entire* CoAlZr layer switches in unison with the TbCo. This is therefore an ideal spring-magnet, where the coercivity of the TbCo layer is not affected by the CoAlZr layer. The magnetic response measured using VSM is the mixture of the response from the TbCo and CoAlZr layer. In an attempt to deconvolute the two responses, we use Eq. 3.6 to fit the out-of-plane hysteresis loops. By doing so we can show that the magnetization reversal is a combination of a single abrupt switch and a single S-shaped loop. The saturation magnetization of these two loops as a function of  $d_B$  shows that there is a region, corresponding to 7.5 nm CoAlZr, that is pinned out of plane and switches in unison with the TbCo. We also observe that there is a reduction and increase in out-of-plane saturation field and in-plane coercivity, respectively, up to 33 nm CoAlZr. This is a long range influence, which is due to the direct exchange coupling between the two layers. As we showed in Chapter 4, the magnetic anisotropy of TbCo is highly tunable.

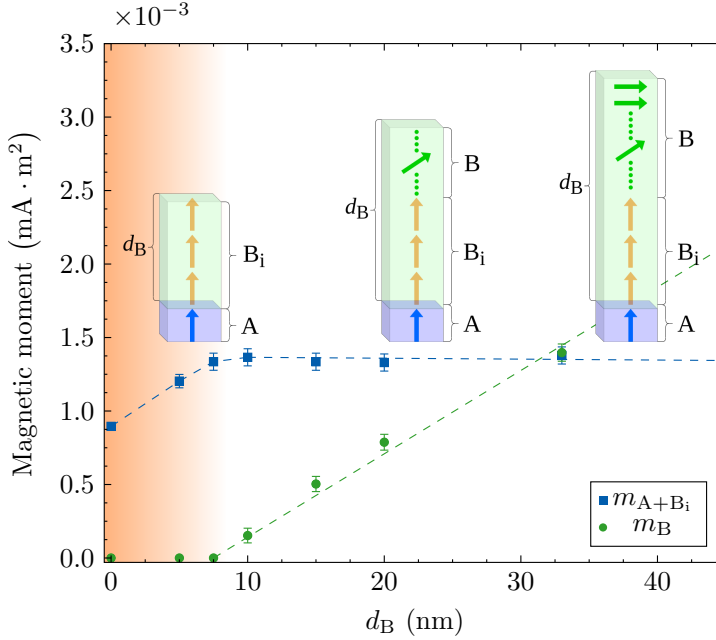


Figure 5.4: Saturation moment as a function of CoAlZr thickness, corresponding to abrupt (blue squares) and hard response (green circles) of the hysteresis loops shown in Fig. 5.3. Up until  $d_B = 7.5$  nm there is no contribution from the hard axis loop, indicating that at least 7.5 nm of the soft CoAlZr switches with the TbCo. The dashed lines are a guide to the eye and extend to  $d_B = 80$  nm (not shown). The insets schematically illustrate the different magnetic components.

Combined with these results, we have demonstrated that amorphous thin films are highly malleable, as the effective anisotropy can easily be tuned both in- and out-of-plane.

As mentioned in the experimental chapter, the VSM does not give information on the depth profile of the magnetization. The spin structure illustrated in Fig. 5.4 is therefore not a definite representation of the depth dependence of the magnetization. For an accurate depth profile, it is ideal to perform PNR. The PNR gives information about the *in-plane* component of the magnetization, we therefore do PNR measurements as a function of in-plane field on a bilayer of 30 nm TbCo/ 20 nm CoAlZr at room temperature. The bilayers have PMA, where the magnetization is pinned out of plane, the magnetic SLD (mSLD) will therefore be the projection of the magnetization onto the plane. The mSLD can be found by fitting the *uu* and *dd* PNR curves, and the angle  $\varphi$  can be calculated using simple algebra from the saturated (680 mT) mSLD profile.

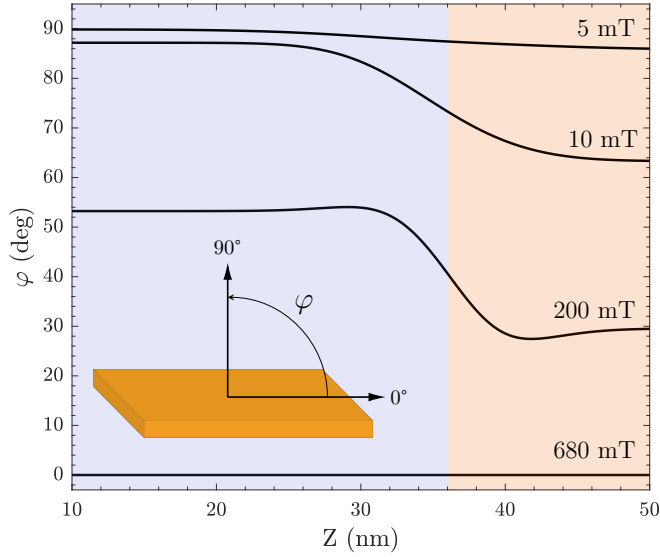


Figure 5.5: The angle of the magnetization  $\varphi$  as a function of depth at various fields, measured on a bilayer 30 nm TbCo/ 20 nm CoAlZr at room temperature.

The results are summarized in Fig. 5.5, which shows the angle of the magnetization as a function of depth, where  $\varphi = 90^\circ$  is perpendicular to the plane and  $\varphi = 0^\circ$  is in-plane, parallel to the guide field. At 5 mT, the magnetization is aligned nearly  $90^\circ$  to the film plane, showing that the magnetic moments of the entire stack are oriented perpendicular to the plane. At 20 mT, the TbCo layer is only minimally tilted towards the applied field ( $5 < \text{degrees}$ ), whereas the CoAlZr is tilted by  $23^\circ$  into the plane. When increasing the field to 200 mT, the in-plane saturation field at the TbCo/CoAlZr is strongly reduced, but notably above the interface the  $\varphi(z)$  plateaus. The constant magnetization as a function of depth clearly shows that the decay length of the exchange coupling between the two layers is much larger than 20 nm. At 680 mT the sample is saturated in-plane, and the magnetization is parallel to the guide field (Paper V).

## Chapter 6

### Concluding thoughts

Magnetism is an emergent property of a collective system, with multiple interacting atoms where each atom can carry a magnetic moment. Without the interaction between atoms there is no magnetization, Curie temperature or magnetic anisotropy. The collective behaviour becomes evident when making very thin magnetic layers. At the interfaces, the number of nearest neighbors each atom has might be eight while the number of nearest neighbors in the bulk is twelve. As a result, the atoms at the interface interact, through the exchange interaction, with fewer atoms and therefore the magnetization of the interface is lower compared to the bulk. This is called a finite size effect, and it is purely an interface effect.

If we have a large block and cleave it, we would expect the total magnetic moment to be divided between the two blocks. Removing a single atom will then certainly lead to the reduction of the total moment corresponding to one atom. If we continue to pluck individual atoms until we have a thin slab, the magnetic moment would decrease linearly as a function of atom removed. What if instead of removing an atom we randomly replace each and individual one with a non-magnetic one. Will we observe the same thing? Is there a fundamental difference between *removing* a magnetic atom vs. *replacing* it with a non-magnetic atom?

Amorphous magnetic metals must contain at least two different elements, either by alloying two or more magnetic materials together, or alloy with something that is non-magnetic. When alloying with a non-magnetic element, we are replacing the magnetic element with a non-magnetic one. The two elements are not uniformly mixed, but there will be regions where there is more of the non-magnetic element and vice versa. By replacing with something non-magnetic, we have not only reduced the moment by one atom but the magnetic elements now have fewer neighbors to interact with. Since the elements are randomly distributed throughout the film, the exchange interaction will vary depending on density, and therefore the magnetization, Curie temperature and magnetic anisotropy. The magnetic properties of amorphous metals are therefore not uniquely defined, but

rather given by a random distribution. The observed magnetic properties of an amorphous thin film are the *average* material properties. However, locally we can define areas where all of these properties deviate from the average.

Although for the most part, the average magnetic properties of amorphous materials are largely similar, reported values of anisotropy, magnetization, critical temperature etc. do vary between different scientific groups. Is this simply due to difference in calibration methods or might different setups produce a unique distribution? The random distribution of elements at first glance does not sound like a feasible control variable. But there might be a way to partially control it and to affect the distribution of the elements within the alloy. Perhaps by changing the kinetic energy of the atoms as they condense at the substrate surface.

The modulations in composition are intrinsic to amorphous materials, and the emerging magnetic properties of amorphous films are a result of competition and interactions between regions of various magnetic properties. Therefore, the distribution of the magnetic properties must be taken into account when working with amorphous magnets, for example when imprinting anisotropy using external field, or exchange coupling or proximity effects in more complex heterostructures [81, 82].

I hope that this work can shed some light on the complex nature of magnetic amorphous alloys, and add to our growing knowledge of what determines their elusive magnetic properties. We now understand, in some way, how the magnetic properties of these fascinating materials can manifest, although there are many questions that are left unanswered. But it should come as no surprise that the 2021 Nobel prize in physics was awarded for work on complex systems [1].



# Bibliography

- <sup>1</sup>The Nobel Prize in Physics 2021, *Nobelprize.org*, Nobel Prize Outreach AB. Accessed March 2022, <https://www.nobelprize.org/prizes/physics/2021/summary/>.
- <sup>2</sup>P. T. Korelis, A. Liebig, M. Bjorck, B. Hjorvarsson, H. Lidbaum, K. Leifer, and A. R. Wildes, “Highly amorphous Fe<sub>90</sub>Zr<sub>10</sub> thin films, and the influence of crystallites on the magnetism,” *Thin Solid Films* **519**, 404–409 (2010).
- <sup>3</sup>P. T. Korelis, P. E. Jönsson, A. Liebig, H.-E. Wannberg, P. Nordblad, and B. Hjörvarsson, “Finite-size effects in amorphous Fe<sub>90</sub>Zr<sub>10</sub>/Al<sub>75</sub>Zr<sub>25</sub> multilayers,” *Phys. Rev. B* **85**, 214430 (2012).
- <sup>4</sup>F. Magnus, R. Moubah, A. H. Roos, A. Kruk, V. Kapaklis, T. Hase, B. Hjorvarsson, and G. Andersson, “Tunable giant magnetic anisotropy in amorphous SmCo thin films,” *Applied Physics Letters* **102**, 162402 (2013).
- <sup>5</sup>F. Magnus, M. E. Brooks-Bartlett, R. Moubah, R. A. Procter, G. Andersson, T. P. A. Hase, S. T. Banks, and B. Hjörvarsson, “Long-range magnetic interactions and proximity effects in an amorphous exchange-spring magnet,” *Nature Communications* **7**, 11931 (2016).
- <sup>6</sup>R. Gemma, M. t. Baben, A. Pundt, V. Kapaklis, and B. Hjörvarsson, “The impact of nanoscale compositional variation on the properties of amorphous alloys,” *Scientific Reports* **10**, 11410 (2020).
- <sup>7</sup>*Periodic Table of Chemical Elements | TikZ example*, [Online; accessed 1. Apr. 2022], <https://texample.net/tikz/examples/periodic-table-of-chemical-elements>.
- <sup>8</sup>S. J. Blundell, *Magnetism in condensed matter* (Oxford University Press, 2014).
- <sup>9</sup>B. D. Cullity and C. D. Graham, *Introduction to magnetic materials* (IEEE press/Wiley, 2009).
- <sup>10</sup>J. C. Slater, “Cohesion in monovalent metals,” *Phys. Rev.* **35**, 509–529 (1930).
- <sup>11</sup>J. C. Slater, “Atomic shielding constants,” *Phys. Rev.* **36**, 57–64 (1930).

- <sup>12</sup>E. C. Stoner and R. Whiddington, “Collective electron specific heat and spin paramagnetism in metals,” *Proceedings of the Royal Society of London. Series A - Mathematical and Physical Sciences* **154**, 656–678 (1936).
- <sup>13</sup>D. Jiles, *Introduction to magnetism and magnetic materials* (CRC Press, Taylor, and Francis Group, 2016).
- <sup>14</sup>T. Mizoguchi, “Amorphous Magnetic Materials,” in *Physics and Engineering Applications of Magnetism* (Springer Series in Solid-State Series, 1991), pp. 178–194.
- <sup>15</sup>J. Rhyne and T. McGuire, “Magnetism of rare-earth elements, alloys, and compounds,” *IEEE Transactions on Magnetics* **8**, 105–130 (1972).
- <sup>16</sup>A. Ciuciulkaite, K. Mishra, M. V. Moro, I.-A. Chioar, R. M. Rowan-Robinson, S. Parchenko, A. Kleibert, B. Lindgren, G. Andersson, C. S. Davies, A. Kimel, M. Berritta, P. M. Oppeneer, A. Kirilyuk, and V. Kapaklis, “Magnetic and all-optical switching properties of amorphous  $\text{Tb}_x\text{Co}_{100-x}$  alloys,” *Phys. Rev. Materials* **4**, 104418 (2020).
- <sup>17</sup>F. Hellman and E. M. Gyorgy, “Growth-induced magnetic anisotropy in amorphous Tb-Fe,” *Phys. Rev. Lett.* **68**, 1391–1394 (1992).
- <sup>18</sup>A. K. Sahoo, J. A. Chelvane, and J. Mohanty, “Role of film thickness and disorder in tuning perpendicular magnetic anisotropy in GdTb-FeCo alloy films,” *Physica Scripta* **96**, 035803 (2021).
- <sup>19</sup>R. Cardias, A. Szilva, A. Bergman, I. D. Marco, M. I. Katsnelson, A. I. Lichtenstein, L. Nordström, A. B. Klautau, O. Eriksson, and Y. O. Kvashnin, “The Bethe-Slater curve revisited; new insights from electronic structure theory,” *Sci. Rep.* **7**, 1–11 (2017).
- <sup>20</sup>N. W. Ashcroft and N. D. Mermin, *Solid state physics* (Holt-Saunders, 1976).
- <sup>21</sup>G. A. T. Allan, “Critical temperatures of ising lattice films,” *Phys. Rev. B* **1**, 352–356 (1970).
- <sup>22</sup>F. Huang, G. J. Mankey, M. T. Kief, and R. F. Willis, “Finite-size scaling behavior of ferromagnetic thin films,” *Journal of Applied Physics* **73**, 6760–6762 (1993).
- <sup>23</sup>Y. Takehashi, *Modern theory of magnetism in metals and alloys*, Vol. 175, Springer Series in Solid-State Sciences (Springer Berlin Heidelberg, 2013).
- <sup>24</sup>K. Yamauchi and T. Mizoguchi, “The magnetic moments of amorphous metal-metalloid alloys,” *Journal of the Physical Society of Japan* **39**, 541–542 (1975).

- 
- <sup>25</sup>A. Frisk, F. Magnus, S. George, U. B. Arnalds, and G. Andersson, “Tailoring anisotropy and domain structure in amorphous TbCo thin films through combinatorial methods,” *Journal of Physics D: Applied Physics* **49**, 35005 (2015).
- <sup>26</sup>A. Hubert and S. R., *Magnetic domains: the analysis of magnetic microstructure* (Springer, 2008).
- <sup>27</sup>F. Magnus, R. Moubah, A. H. Roos, A. Kruk, V. Kapaklis, T. Hase, B. Hjörvarsson, and G. Andersson, “Tunable giant magnetic anisotropy in amorphous SmCo thin films,” *Applied Physics Letters* **102** (2013).
- <sup>28</sup>J. Rhyne and T. McGuire, “Magnetism of rare-earth elements, alloys, and compounds,” *IEEE Transactions on Magnetism* **8**, 105–130 (1972).
- <sup>29</sup>M. Mansuripur, “Magnetization reversal, coercivity, and the process of thermomagnetic recording in thin films of amorphous rare earth–transition metal alloys,” *Journal of Applied Physics* **61**, 1580–1587 (1987).
- <sup>30</sup>Y. Suzuki, S. Takayama, F. Kirino, and N. Ohta, “Single ion model for perpendicular magnetic anisotropy in RE-TM amorphous films,” *IEEE Transactions on Magnetism* **23**, 2275–2277 (1987).
- <sup>31</sup>M. Kateb, J. T. Gudmundsson, and S. Ingvarsson, “Effect of atomic ordering on the magnetic anisotropy of single crystal Ni<sub>80</sub>Fe<sub>20</sub>,” *AIP Advances* **9**, 035308 (2019).
- <sup>32</sup>V. G. Harris, K. D. Aylesworth, B. N. Das, W. T. Elam, and N. C. Koon, “Structural origins of magnetic anisotropy in sputtered amorphous Tb-Fe films,” *Physical Review Letters* **69**, 1939–1942 (1992).
- <sup>33</sup>H. Raanaei, H. Nguyen, G. Andersson, H. Lidbaum, P. Korelis, K. Leifer, and B. Hjörvarsson, “Imprinting layer specific magnetic anisotropies in amorphous multilayers,” *Journal of Applied Physics* **106**, 023918 (2009).
- <sup>34</sup>F. Magnus, R. Moubah, V. Kapaklis, G. Andersson, and B. Hjörvarsson, “Magnetostriptive properties of amorphous SmCo thin films with imprinted anisotropy,” *Physical Review B - Condensed Matter and Materials Physics* **89**, 1 (2014).
- <sup>35</sup>K. A. Thórarinsdóttir, H. Palonen, G. K. Palsson, B. Hjörvarsson, and F. Magnus, “Giant magnetic proximity effect in amorphous layered magnets,” *Phys. Rev. Materials* **3**, 054409 (2019).
- <sup>36</sup>K. A. Thórarinsdóttir, T. Hase, B. Hjörvarsson, and F. Magnus, “Amorphous exchange-spring magnets with crossed perpendicular and in-plane anisotropies,” *Phys. Rev. B* **103**, 014440 (2021).

- <sup>37</sup>K. A. Thórarinsdóttir, N. Strandqvist, V. V. Sigurjónsdóttir, E. B. Thorsteinsson, B. Hjörvarsson, and F. Magnus, “Finding order in disorder: magnetic coupling distributions and competing anisotropies in an amorphous metal alloy,” *APL Materials* **10**, 041103 (2022).
- <sup>38</sup>M. T. Johnson, P. J. H. Bloemen, F. J. A. den Broeder, and J. J. de Vries, “Magnetic anisotropy in metallic multilayers,” *Reports on Progress in Physics* **59**, 1409–1458 (1996).
- <sup>39</sup>L. Néel, “Anisotropie magnétique superficielle et surstructures d’orientation,” *J. Phys. Radium* **15**, 225–239 (1954).
- <sup>40</sup>H. J. G. Draaisma and W. J. M. de Jonge, “Surface and volume anisotropy from dipole-dipole interactions in ultrathin ferromagnetic films,” *Journal of Applied Physics* **64**, 3610–3613 (1988).
- <sup>41</sup>B. M. S. Teixeira, A. A. Timopheev, R. Schmidt, M. R. Soares, M. Seifert, V. Neu, and N. A. Sobolev, “Transfer of spin reorientation in a NdCo<sub>5</sub>/Fe bilayer,” *J. Phys. D: Appl. Phys.* **49**, 315002 (2016).
- <sup>42</sup>P. Sharma, H. Kimura, and A. Inoue, “Observation of unusual magnetic behavior: Spin reorientation transition in thick Co–Fe–Ta–B glassy films,” *Journal of Applied Physics* **100**, 083902 (2006).
- <sup>43</sup>K. Chesnel, A. S. Westover, C. Richards, B. Newbold, M. Healey, L. Hindman, B. Dodson, K. Cardon, D. Montealegre, J. Metzner, T. Schneider, B. Böhm, F. Samad, L. Fallarino, and O. Hellwig, “Morphological stripe-bubble transition in remanent magnetic domain patterns of Co/Pt multilayer films and its dependence on Co thickness,” *Phys. Rev. B* **98**, 224404 (2018).
- <sup>44</sup>C.-F. Pai, M.-H. Nguyen, C. Belvin, L. H. Vilela-Leão, D. C. Ralph, and R. A. Buhrman, “Enhancement of perpendicular magnetic anisotropy and transmission of spin-Hall-effect-induced spin currents by a Hf spacer layer in W/Hf/CoFeB/MgO layer structures,” *Applied Physics Letters* **104**, 082407 (2014).
- <sup>45</sup>M. Arora, R. Hübner, D. Suess, B. Heinrich, and E. Girt, “Origin of perpendicular magnetic anisotropy in Co/Ni multilayers,” *Phys. Rev. B* **96**, 024401 (2017).
- <sup>46</sup>T. Liu, J. W. Cai, and L. Sun, “Large enhanced perpendicular magnetic anisotropy in CoFeB/MgO system with the typical Ta buffer replaced by an Hf layer,” *AIP Advances* **2**, 032151 (2012).

- 
- <sup>47</sup>D.-T. Ngo, D.-T. Quach, Q.-H. Tran, K. Møhave, T.-L. Phan, and D.-H. Kim, “Perpendicular magnetic anisotropy and the magnetization process in CoFeB/Pd multilayer films,” *Journal of Physics D: Applied Physics* **47**, 445001 (2014).
- <sup>48</sup>J. Nogués, J. Sort, V. Langlais, V. Skumryev, S. Suriñach, J. Muñoz, and M. Baró, “Exchange bias in nanostructures,” *Physics Reports* **422**, 65–117 (2005).
- <sup>49</sup>J. Nogués and I. K. Schuller, “Exchange bias,” *Journal of Magnetism and Magnetic Materials* **192**, 203–232 (1999).
- <sup>50</sup>V. Skumryev, S. Stoyanov, Y. Zhang, G. Hadjipanayis, D. Givord, and J. Nogués, “Beating the superparamagnetic limit with exchange bias,” *Nature* **423**, 850–853 (2003).
- <sup>51</sup>E. Kneller and R. Hawig, “The exchange-spring magnet: a new material principle for permanent magnets,” *IEEE Transactions on Magnetics* **27**, 3588–3560 (1991).
- <sup>52</sup>E. E. Fullerton, J. Jiang, and S. Bader, “Hard/soft magnetic heterostructures: model exchange-spring magnets,” *Journal of Magnetism and Magnetic Materials* **200**, 392–404 (1999).
- <sup>53</sup>Z. J. Guo, J. S. Jiang, J. E. Pearson, S. D. Bader, and J. P. Liu, “Exchange-coupled Sm–Co/Nd–Co nanomagnets: correlation between soft phase anisotropy and exchange field,” *Applied Physics Letters* **81**, 2029–2031 (2002).
- <sup>54</sup>E. Kneller and R. Hawig, “The exchange-spring magnet: a new material principle for permanent magnets,” *IEEE Transactions on Magnetics* **27**, 3588–3560 (1991).
- <sup>55</sup>S.-s. Yan, J. Barnard, F.-t. Xu, J. Weston, and G. Zangari, “Critical dimension of the transition from single switching to an exchange spring process in hard/soft exchange-coupled bilayers,” *Physical Review B* **64**, 184403 (2001).
- <sup>56</sup>A. Scherz, P. Pouloupoulos, H. Wende, G. Ceballos, K. Baberschke, and F. Wilhelm, “Thickness dependence of the V induced magnetic moment in Fe/V/Fe(110) trilayers,” *Journal of Applied Physics* **91**, 8760–8762 (2002).
- <sup>57</sup>O. Rader, E. Vescovo, J. Redinger, S. Blügel, C. Carbone, W. Eberhardt, and W. Gudat, “Fe-induced magnetization of Pd: The role of modified Pd surface states,” *Phys. Rev. Lett.* **72**, 2247–2250 (1994).

- <sup>58</sup>F. Magnus, M. E. Brooks-Bartlett, R. Moubah, R. A. Procter, G. Andersson, T. Hase, S. T. Banks, and B. Hjörvarsson, “Long-range magnetic interactions and proximity effects in an amorphous exchange-spring magnet,” *Nature Communications* **7**, 11931 (2016).
- <sup>59</sup>U. Bovensiepen, F. Wilhelm, P. Srivastava, P. Poulopoulos, M. Farle, A. Ney, and K. Baberschke, “Two susceptibility maxima and element specific magnetizations in indirectly coupled ferromagnetic layers,” *Phys. Rev. Lett.* **81**, 2368–2371 (1998).
- <sup>60</sup>K. Lenz, S. Zander, and W. Kuch, “Magnetic proximity effects in anti-ferromagnet/ferromagnet bilayers: the impact on the néel temperature,” *Phys. Rev. Lett.* **98**, 237201 (2007).
- <sup>61</sup>N. J. Gökemeijer, T. Ambrose, and C. L. Chien, “Long-range exchange bias across a spacer layer,” *Phys. Rev. Lett.* **79**, 4270–4273 (1997).
- <sup>62</sup>M. Birkholz and C. Genzel, “Residual stress analysis,” in *Thin Film Analysis by X-Ray Scattering* (John Wiley & Sons, Ltd, 2005) Chap. 6, pp. 239–295.
- <sup>63</sup>S. Foner, “Versatile and sensitive vibrating-sample magnetometer,” *Review of Scientific Instruments* **30**, 548–557 (1959).
- <sup>64</sup>M. Newville, T. Stensitzki, D. B. Allen, and A. Ingargiola, *LMFIT: Non-Linear Least-Square Minimization and Curve-Fitting for Python*, version 0.8.0, Sept. 2014.
- <sup>65</sup>H. Dachs, *Neutron Diffraction (Topics in Current Physics, 6)* (Springer, Berlin, Germany, Dec. 2011).
- <sup>66</sup>H. W. Sheng, W. K. Luo, F. M. Alamgir, J. M. Bai, and E. Ma, “Atomic packing and short-to-medium-range order in metallic glasses,” *Nature* **439**, 419–425 (2006).
- <sup>67</sup>H. W. Sheng, H. Z. Liu, Y. Q. Cheng, J. Wen, P. L. Lee, W. K. Luo, S. D. Shastri, and E. Ma, “Polyamorphism in a metallic glass,” *Nature Materials* **6**, 192–197 (2007).
- <sup>68</sup>D. Ma, A. D. Stoica, and X. L. Wang, “Power-law scaling and fractal nature of medium-range order in metallic glasses,” *Nature Materials* **8**, 30–34 (2008).
- <sup>69</sup>A.-C. Dippel, M. Roelsgaard, U. Boettger, T. Schneller, O. Gutowski, and U. Ruett, “Local atomic structure of thin and ultrathin films via rapid high-energy X-ray total scattering at grazing incidence,” *IUCrJ* **6**, 290–298 (2019).

- 
- <sup>70</sup>S. George, K. Kádas, P. E. Jönsson, G. Muscas, F. Magnus, O. Eriksson, A. Delin, and G. Andersson, “Local structure in amorphous  $\text{Sm}_x\text{Co}_{1-x}$ : a combined experimental and theoretical study,” *Journal of Materials Science* **55**, 1–11 (2020).
- <sup>71</sup>J. Deisenhofer, D. Braak, H.-A. K. v. Nidda, J. Hemberger, R. M. Eremina, V. A. Ivanshin, A. M. Balbashov, G. Jug, A. Loidl, T. Kimura, and Y. Tokura, “Observation of a Griffiths Phase in Paramagnetic  $\text{La}_{1-x}\text{Sr}_x\text{MnO}_3$ ,” *Physical Review Letters* **95**, 257202 (2005).
- <sup>72</sup>K. Thórarinsdóttir, B. Thorbjarnardóttir, U. Arnalds, and F. Magnus, “Tuneable spin reorientation transitions in Co-rich TbCo amorphous thin films,” Submitted under review **X** (2022).
- <sup>73</sup>K. Ueda, M. Mann, C.-F. Pai, A.-J. Tan, and G. S. D. Beach, “Spin-orbit torques in Ta/Tb<sub>x</sub>Co<sub>100-x</sub> ferrimagnetic alloy films with bulk perpendicular magnetic anisotropy,” *Applied Physics Letters* **109**, 232403 (2016).
- <sup>74</sup>J. Finley and L. Liu, “Spin-orbit-torque efficiency in compensated ferrimagnetic cobalt-terbium alloys,” *Phys. Rev. Applied* **6**, 054001 (2016).
- <sup>75</sup>M. S. El Hadri, M. Hehn, P. Pirro, C.-H. Lambert, G. Malinowski, E. E. Fullerton, and S. Mangin, “Domain size criterion for the observation of all-optical helicity-dependent switching in magnetic thin films,” *Phys. Rev. B* **94**, 064419 (2016).
- <sup>76</sup>S.-G. Je, J.-C. Rojas-Sánchez, T. H. Pham, P. Vallobra, G. Malinowski, D. Lacour, T. Fache, M.-C. Cyrille, D.-Y. Kim, and S.-B. Choe, “Spin-orbit torque-induced switching in ferrimagnetic alloys: experiments and modeling,” *Applied Physics Letters* **112**, 062401 (2018).
- <sup>77</sup>A. Ceballos, M. Charilaou, M. Molina-Ruiz, and F. Hellman, “Coexistence of soft and hard magnetic phases in single layer amorphous Tb–Co thin films,” *Journal of Applied Physics* **131**, 033901 (2022).
- <sup>78</sup>M. Hennes, A. Merhe, X. Liu, D. Weder, C. v. K. Schmising, M. Schneider, C. M. Günther, B. Mahieu, G. Malinowski, M. Hehn, D. Lacour, F. Capotondi, E. Pedersoli, I. P. Nikolov, V. Chardonnet, E. Jal, J. Lüning, and B. Vodungbo, “Laser-induced ultrafast demagnetization and perpendicular magnetic anisotropy reduction in a  $\text{Co}_{88}\text{Tb}_{12}$  thin film with stripe domains,” *Phys. Rev. B* **102**, 174437 (2020).
- <sup>79</sup>F. Magnus, U. B. Arnalds, H. Palonen, G. K. Pálsson, H. Ali, K. Leifer, and B. Hjörvarsson, “Tuneable exchange-spring stiffness in amorphous magnetic trilayer structures,” *Journal of Physics: Condensed Matter* **33**, 445803 (2021).

- <sup>80</sup>R. A. Procter, F. Magnus, G. Andersson, C. Sánchez-Hanke, B. Hjörvarsson, and T. Hase, “Magnetic leverage effects in amorphous SmCo/CoAlZr heterostructures,” *Applied Physics Letters* **107**, 062403 (2015).
- <sup>81</sup>L. Fallarino, B. J. Kirby, and E. E. Fullerton, “Graded magnetic materials,” *J. Phys. D: Appl. Phys.* **54**, 303002 (2021).
- <sup>82</sup>Z. Zheng, Y. Zhang, V. Lopez-Dominguez, L. Sánchez-Tejerina, J. Shi, X. Feng, L. Chen, Z. Wang, Z. Zhang, K. Zhang, B. Hong, Y. Xu, Y. Zhang, M. Carpentieri, A. Fert, G. Finocchio, W. Zhao, and P. Khalili Amiri, “Field-free spin-orbit torque-induced switching of perpendicular magnetization in a ferrimagnetic layer with a vertical composition gradient,” *Nat. Commun.* **12**, 1–9 (2021).



# Abbreviations

AFM	Antiferromagnetic
bcc	Body-centered cubic
DOS	Density of states
DC	Direct current
FM	Ferromagnetic
GIXRD	Grazing incidence x-ray diffraction
IMA	In-plane magnetic anisotropy
MOKE	Magneto-optic Kerr effect
mSLD	Magnetic scattering length density
NSF	Non-spin flip
PM	Paramagnetic
PMA	Perpendicular magnetic anisotropy
PNR	Polarized neutron reflectometry
RE	Rare-earth
SLD	Scattering length density
SF	Spin flip
SRT	Spin reorientation transition
TM	Transition metal
UHV	Ultra high vacuum
UMA	Uniaxial magnetic anisotropy
VSM	Vibrating sample magnetometer
XRD	X-ray diffraction
XRR	X-ray reflectivity



## Chapter 7

### Original papers



# Paper I

## **Giant magnetic proximity effect in amorphous layered magnets**

K.A. Thórarinsdóttir, H. Palonen, G.K. Pálsson, B. Hjörvarsson, F. Magnus

Physical Review Material, **3**,054409 (2019)



## Giant magnetic proximity effect in amorphous layered magnets

K. A. Thórarinsdóttir,<sup>1</sup> H. Palonen,<sup>2</sup> G. K. Palsson,<sup>2</sup> B. Hjörvarsson,<sup>2</sup> and F. Magnus<sup>1,2,\*</sup>

<sup>1</sup>*Science Institute, University of Iceland, Dunhaga 3, IS-107 Reykjavik, Iceland*

<sup>2</sup>*Department of Physics and Astronomy, Uppsala University, Box 530, SE-75121 Uppsala, Sweden*



(Received 12 December 2018; revised manuscript received 8 April 2019; published 21 May 2019)

Here we study the magnetic proximity effect in amorphous layered magnets of alternating high- and low- $T_c$  materials using magnetometry and polarized neutron reflectivity. By altering the thickness of either the high- or low- $T_c$  layer we are able to extract the induced magnetic moment in the low- $T_c$  layer directly and study how it scales with thickness. We observe that the ordering temperature of the low- $T_c$  layer is enhanced and above which a second magnetically ordered state with a very large extension is observed. This induced magnetic state survives to a temperature at least three times that of the ordering temperature of the low- $T_c$  layer and the induced magnetization is approximately constant throughout at least a 10-nm-thick layer. The induced magnetic region within the low- $T_c$  layer does not depend on the thickness of the adjacent high- $T_c$  layer.

DOI: 10.1103/PhysRevMaterials.3.054409

### I. INTRODUCTION

The magnetic proximity effect refers to an induced magnetic ordering in an intrinsically nonmagnetic material which is brought about by proximity to a magnetic material [1,2]. It is typically observed in composite or layered structures, where one component is ferromagnetic (FM) or antiferromagnetic (AFM) and the other is paramagnetic (PM) or has a lower ordering temperature [3]. The influence of such a proximity effect can be diverse. In FM-PM systems a magnetization can be induced in the PM material and in FM-FM or FM-AFM systems the ordering temperature ( $T_c$  or  $T_N$ ) can be enhanced [4–6]. The induced magnetization can in turn result in nonoscillatory interlayer exchange coupling across metallic spacers [7] as well as spring-magnetic behavior and long-range exchange bias through intrinsically paramagnetic layers [5].

Nanoscale magnetic devices such as magnetic memory, sensors, and logic devices are typically composed of layers of coupled magnetic and nonmagnetic materials [8,9]. Magnetic proximity effects will inevitably influence the performance of such devices and must be taken into account in their design [3]. Layering of different types of magnetic materials is also a powerful way to tune or enhance their overall magnetic properties [10]. In this context, the proximity effect can, for example, be used to increase the ordering temperature of dilute magnetic semiconductors [11], control interlayer coupling [5] or induce ferromagnetism or more complex spin textures in topological insulators [12–14]. Therefore, it is important to gain a better understanding of the magnetic proximity effect and determine its size and extension in technologically important systems.

The proximity effect arises because of magnetic interactions between atoms across the interface and hybridization of interface states [2]. It has generally been considered to

be short-ranged, typically extending only a few atomic layers into the nonmagnetic material [2,3,15]. For example, in the much studied Fe/V system the magnetic moment in the V has an exponential decay length of approximately 0.3 nm [15] but by replacing the V with an FeV alloy the decay length can be extended to 1.7 nm [16]. A somewhat larger proximity effect is found in high susceptibility paramagnets such as Pd and Pt where the induced magnetization can extend up to a few nanometers into the paramagnet [17–19]. Recently, however, it has been shown indirectly that in amorphous heterostructures the effect can extend several tens of nanometers into the nonmagnetic material [5]. This is achieved by tuning the composition of the amorphous alloys such that they are on the verge of ferromagnetism or have a low ferromagnetic ordering temperature. By using amorphous materials it is possible to tune the intrinsic ordering temperature without significantly affecting the interface structure since there is no lattice mismatch at the interfaces [20,21]. In addition, the density modulations inherent in such disordered alloys could contribute to the long range of the proximity effect [22,23].

Here we study the magnetic proximity effect in amorphous multilayers which are composed of alternating high- and low- $T_c$  layers by a combination of magnetometry and polarized neutron reflectivity. This allows us to measure directly the magnetization which is induced in the low- $T_c$  layers above their intrinsic ordering temperature and determine how the region of induced magnetization scales with the layer thickness. The results show that proximity effects can induce an almost constant magnetization with a remarkably long extension in an intrinsically paramagnetic amorphous material.

### II. EXPERIMENTAL METHODS AND DESIGN

The samples were grown at room temperature by dc magnetron sputtering in a sputtering chamber with a base pressure below  $5 \times 10^{-10}$  Torr. The sputtering gas was Ar of 99.9999% purity and the growth pressure was 2.0 mTorr. Si(100) substrates with the native oxide layer were used. The substrates

\*fridrikm@hi.is

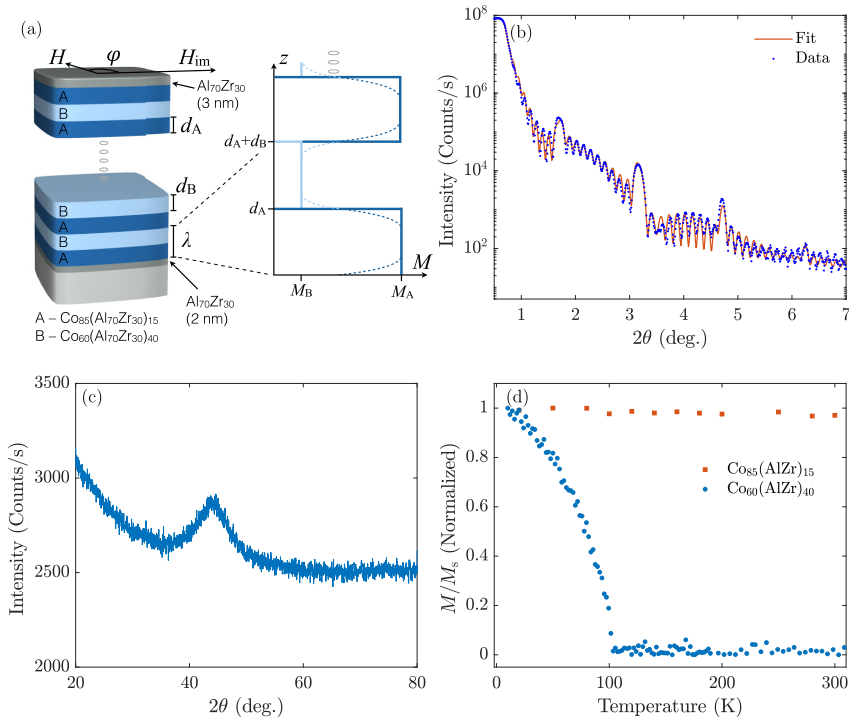


FIG. 1. (a) A schematic of the sample structure (left) and the magnetization profile of one bilayer, below  $T_c^B$  (right). The solid lines are a simple constant magnetization approximation, whereas the dashed lines represent a smoothly varying magnetization across the interfaces. (b) x-Ray reflectivity of the multilayer with  $d_B = 5$  nm and  $d_A = 1$  nm including a fit. (c) A representative grazing incidence x-ray diffraction scan of a multilayer sample showing a broad characteristic amorphous peak. (d) Remanent magnetization for Co<sub>85</sub>(Al<sub>70</sub>Zr<sub>30</sub>)<sub>15</sub> (layer A) and Co<sub>60</sub>(Al<sub>70</sub>Zr<sub>30</sub>)<sub>40</sub> (layer B) showing an ordering temperature of  $T_c^B = 103 \pm 5$  K for the Co<sub>60</sub>(Al<sub>70</sub>Zr<sub>30</sub>)<sub>40</sub>. The data are normalized to the saturation magnetization at 10 K.

were annealed in vacuum at 550 °C for 30 minutes prior to growth. First, a 2-nm-thick buffer layer of Al<sub>70</sub>Zr<sub>30</sub> was deposited on the substrate from an Al<sub>70</sub>Zr<sub>30</sub> alloy target (purity 99.9%). Subsequently, a multilayer of Co<sub>85</sub>(Al<sub>70</sub>Zr<sub>30</sub>)<sub>15</sub> (layer A) and Co<sub>60</sub>(Al<sub>70</sub>Zr<sub>30</sub>)<sub>40</sub> (layer B) was grown by cosputtering from Co (purity 99.9%) and Al<sub>70</sub>Zr<sub>30</sub> targets, always beginning and ending with a Co<sub>85</sub>(Al<sub>70</sub>Zr<sub>30</sub>)<sub>15</sub> layer. Between layers, the shutters in front of all magnetrons were closed momentarily while the power applied to the Co magnetron was changed to obtain the desired composition. The composition was determined by careful rate calibrations for each magnetron. All samples were capped with a 3-nm layer of AlZr. The sample structure is shown schematically in Fig. 1(a). The room temperature growth, choice of compositions, and the use of an Al<sub>70</sub>Zr<sub>30</sub> buffer layer ensures that the films are fully amorphous and that the interfaces are sharp [24,25]. x-Ray reflectivity (XRR) and grazing incidence x-ray diffraction (GIXRD) measurements were performed to confirm this. A PANalytical X'pert Pro diffractometer was used, equipped with a Göbel mirror on the incident side and a parallel plate collimator on the diffracted side. Characteristic XRR and GIXRD measurements are shown in Figs. 1(b) and 1(c), respectively. The XRR shows clear multilayer Bragg peaks which arise due to the periodicity in the sample density,

as well as Kiessig thickness fringes up to at least  $2\theta = 7^\circ$ , attesting to the low surface and interface roughnesses. Fitting of the XRR data using the layer model shown in Fig. 1(a) gives interface widths of approximately 0.4-nm rms and confirms that the actual thicknesses agree with the nominal ones. We can therefore rule out intermixing between layers or interlayer coupling due to interface roughness (orange peel coupling). The GIXRD (performed with the incidence angle fixed at  $\omega = 1^\circ$ ) shows a single broad peak centered at approximately  $2\theta = 45^\circ$ , characteristic of an amorphous structure (see, for example, Ref. [26]).

The difference in cobalt content results in different intrinsic ordering temperatures of layers A and B when grown separately. Layer A has an ordering temperature  $T_c^A$  which is well above room temperature, whereas layer B has an ordering temperature of  $T_c^B = 103 \pm 5$  K, as shown by the temperature dependence of the remanent magnetization of each layer in Fig. 1(d). Below the ordering temperatures of both layers they are both ferromagnetic but the magnetization of layer B will be significantly lower than that of A, as shown schematically in Fig. 1(a). In the temperature regime between the two ordering temperatures there will be an induced magnetization in the B layer due to the proximity to the A layer but its size, extension, and profile is unknown. In order to study these



factors, two thickness series of the layers were produced: (i) with the layer A thickness fixed at  $d_A = 5$  nm and the B-layer thickness  $d_B$  in the range 2.5 to 10 nm (hereafter referred to as the B-layer series) and (ii) with the B-layer thickness fixed at 5 nm and the A-layer thickness in the range 1 to 10 nm (hereafter referred to as the A-layer series). In addition, a uniaxial in-plane anisotropy was induced in the A layers by applying a magnetic field of approximately  $H_{\text{im}} = 0.1$  T during growth [24,25]. The total magnetic moment of the multilayers was measured using vibrating sample magnetometry (VSM) in a longitudinal geometry. Full hysteresis curves were measured parallel to the plane of the films at each temperature and the saturation moment at 20 mT extracted.

Polarized neutron reflectivity (PNR) measurements were carried out on the Super ADAM beamline at the Institut Laue–Langevin to study the magnetization profile of the multilayers. The neutron wavelength was 5.183 Å and the measurements were performed at 120 K (somewhat above  $T_c^B$ ). A guide field of 1.5–3.0 mT was used to maintain the neutron polarization parallel to the plane of the films and an electromagnet was used to saturate the sample along the in-plane easy axis, which was in all cases parallel to the guide field. The data was normalized by a monitor to account for fluctuations in the neutron flux and to correct for points measured for different lengths of time. A constant slit opening for the entire data set was chosen such that the sample was overilluminated which was corrected for before fitting. Fitting of the data was performed in the GenX software package [27] using the layer model depicted in Fig. 1(a).

### III. RESULTS AND DISCUSSION

Representative magnetic hysteresis curves for the multilayers can be seen in Fig. 2(a) where the magnetization is measured at an in-plane angle of  $\varphi = 0^\circ$  and  $\varphi = 90^\circ$  with respect to the growth field. The uniaxial anisotropy imprinted by the growth field results in a square hysteresis loop for  $\varphi = 0^\circ$  (the easy axis) and a linear hysteresis loop with zero remanence along  $\varphi = 90^\circ$  (the hard axis). The measurements shown in the figure are for the sample with  $d_B = 5$  nm and  $d_A = 10$  nm at room temperature but the general shape of the hysteresis curves is the same at all temperatures and for all samples.

The saturation (20 mT) magnetization extracted from such hysteresis loops as a function of temperature is shown in Fig. 2(b) for the B-layer series. For the sample with  $d_B = 10$  nm, a clear change in slope  $dM/dT$  is seen at approximately 140 K, which is somewhat above the intrinsic ordering temperature of the B layer. This indicates that the multilayer has an ordering temperature that is above  $T_c^B$ , although the exact temperature cannot be pinpointed with the current data. For thinner B layers (2.5 nm and 5.0 nm) the magnetization appears to decrease monotonously with increasing temperature and there is no clear sign of a magnetic phase transition. This is strong evidence of a large magnetic proximity effect. However, it is difficult to determine with any certainty from this data presentation how the magnetization of the B layer changes because of the relative size of the magnetization of the A and B layers.

The scaling of the magnetization with  $d_B$  gives an insight into the size and extension of the induced magnetization in the

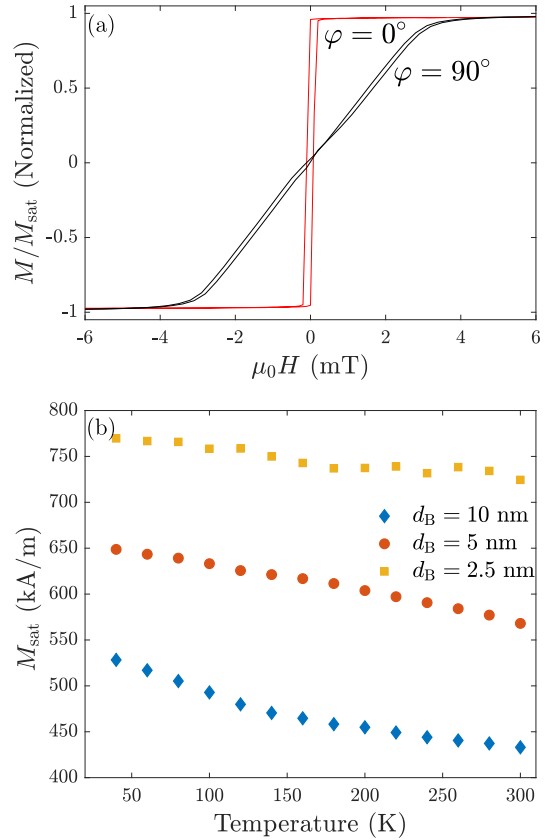


FIG. 2. (a) Room-temperature magnetization, normalized by the saturation magnetization, versus applied in-plane magnetic field for the multilayer with  $d_B = 5$  nm and  $d_A = 10$  nm. The field is oriented either parallel (red) or perpendicular (black) to the applied growth field, resulting in an easy or hard axis response, respectively. (b) The saturation magnetization of the B-layer thickness series as a function of temperature.

B layer. The simplest model to describe the magnetization of the layers is to assume that it is constant within each layer. This is depicted in Fig. 1(a) with the solid blue lines. In this case, the average magnetization of a bilayer of thickness  $\lambda = d_A + d_B$  is given by the weighted average of the magnetization of the two layers, which can be expressed as

$$M_{\text{avg}} = d_A(M_A - M_B)\frac{1}{\lambda} + M_B, \quad (1)$$

where  $M_{\text{avg}}$  is the average saturation magnetization of the bilayer and  $M_A$  and  $M_B$  the saturation magnetizations of layers A and B, respectively [16].

Figure 3(a) shows the measured magnetization, plotted as a function of the inverse bilayer thickness for the B-layer series. The linear dependence with a nonzero intercept at all temperatures is striking and fully consistent with Eq. (1). The variation in the slope is due only to a variation in the

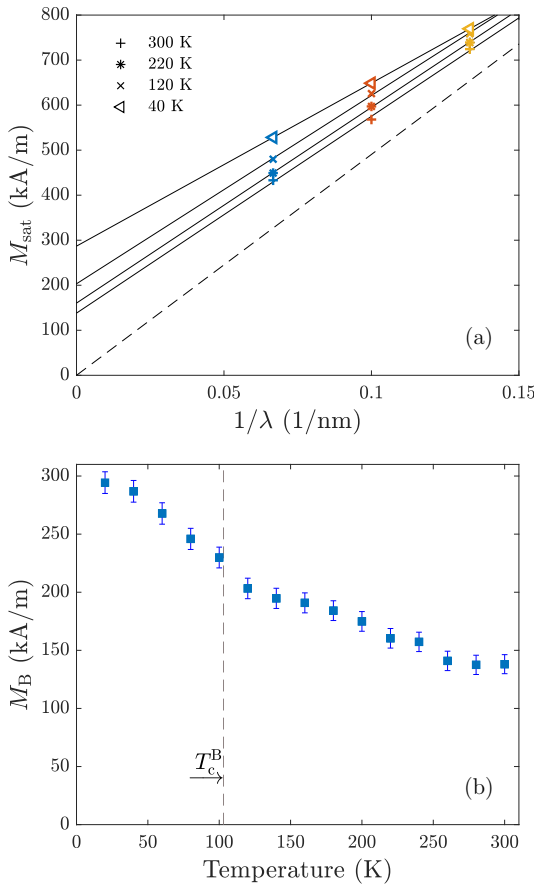


FIG. 3. (a) The saturation magnetization versus the inverse bi-layer thickness for a selection of temperatures for the B-layer thickness series. The solid lines are fits to the data and the dashed line is the linear model [Eq. (1)] with  $M_B$  set to zero (no proximity effect). (b) The magnetization of the B layer,  $M_B$ , extracted from the intercept of the fitted lines in (a). The intercept corresponds to  $M_B$  according to the linear model [Eq. (1)].

magnetization of layer B since both  $M_A$  and  $d_A$  are constant in this thickness series. The slope is positive due to the fact that  $M_B < M_A$  and increases with increasing temperature, in line with a decreasing  $M_B$ . The intercept yields  $M_B$  directly which should reduce to zero above  $T_c^B$  in the absence of a proximity effect, as shown by the dashed line in the figure (where we use the measured “bulk” value of  $M_A$ ). This is clearly not the case, even at room temperature, showing that there is a proximity induced magnetization in layer B at three times its intrinsic ordering temperature. Furthermore, an exponentially decaying profile of the induced magnetization would be expected away from the interfaces [5], which would result in a nonlinear scaling of  $M$  with  $\lambda^{-1}$  [16]. This is not observed in Fig. 3(a), meaning that the magnetization is indeed approximately constant throughout the entire thickness

of the layer at all temperatures. Therefore, either the decay length is significantly longer than the largest B-layer thickness (10 nm) or the magnetization decays to a constant value with a decay length much smaller than the smallest  $d_B$ . This scenario is depicted schematically in Fig. 2(a) with the dashed lines.

The temperature dependence of the magnetization of layer B is shown in Fig. 3(b). The values are extracted from the intercepts of the linear fits in Fig. 3(a). The magnetization decreases with increasing temperature, as expected, but is nonzero at all measured temperatures as previously noted. However, there is a critical point in the curve at a temperature somewhat above  $T_c^B$  reminiscent of the ferromagnetic to paramagnetic phase transition which occurs in B on layer its own at  $T_c^B$ . This shows the dual impact of the magnetic proximity effect; first, it enhances the ordering temperature of the B layer and, second, it induces a new magnetically ordered state with a very large extension, which survives to much higher temperatures.

This dual impact of the proximity effect is consistent with a previous study of a similar amorphous heterostructure composed of a B layer sandwiched by an A layer and a SmCo hard magnet layer [5]. This study showed that the proximity effect resulted in both spring-magnet behavior and exchange bias but the two had very different temperature dependence and extension. Below the enhanced ordering temperature they had an induced ferromagnetic state with a significant spin stiffness which could sustain a spring-magnet effect. At higher temperatures they had a magnetic state with a significant moment but negligible spin stiffness (a super-paramagnetic-like state) which could cause an exchange bias on an adjacent magnetic layer. In the multilayers studied here we do not have a spring-magnet effect or exchange bias since all layers have a small anisotropy and the structure switches as a whole. However, we are able to detect the induced magnetization directly for the two different magnetic phases. The large extension of the proximity effect and the resulting complex magnetic phase diagram can be explained by the amorphous structure and composition of the films. In general, the hybridization of the 3d band of the ferromagnet across the interface will decay rapidly away from the interface on a length scale of a few atomic layers. However, the ordering temperature of the B layer is strongly dependent on the amount of Co and therefore a small increase in the density of states can be sufficient to enhance it significantly. In addition, the inherent local variation in the concentration of the magnetic element within the amorphous alloy means that it will inevitably have local variations in  $T_c$  with interconnected regions of high and low magnetic coupling strength [22]. An effective field from the adjacent ferromagnets can therefore polarize the amorphous alloy far above its intrinsic ferromagnetic ordering temperature.

The temperature dependence of the magnetization of the A-layer thickness series is presented in the inset of Fig. 4(a). Note that the sample  $d_A = d_B = 5$  nm is common to both thickness series. There is no inflection around  $T_c^B$  for any of the samples, and the magnetic moment decreases monotonously. This indicates that the induced magnetization in layer B does not depend on the thickness of the source layer.

The scaling of the magnetization of the A series with  $\lambda^{-1}$  can be seen in Fig. 4(b). Assuming a constant magnetization

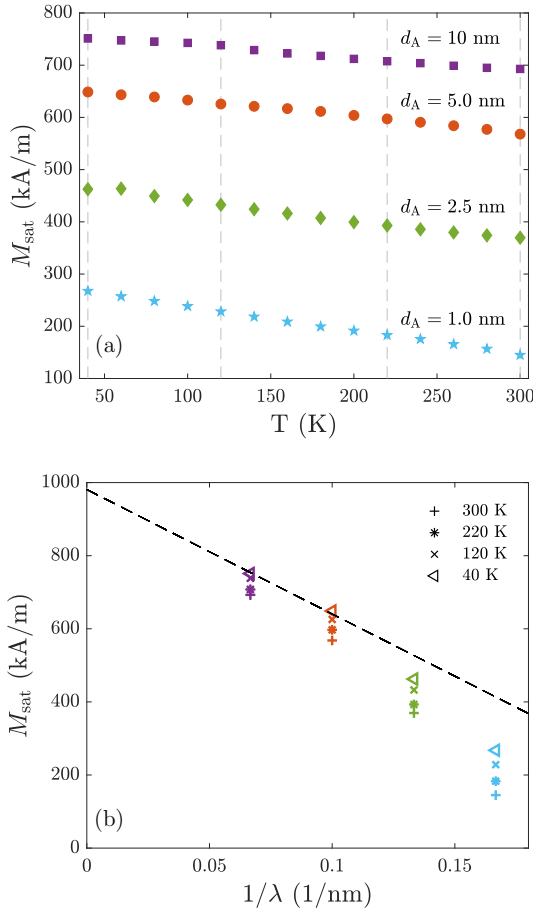


FIG. 4. (a) The magnetization of the A-layer thickness series as a function of temperature. The magnetization decreases monotonously with increasing temperature. (b) The bilayer thickness dependence of the magnetization of the A series for selected temperatures. The magnetization does not vary linearly with thickness over the entire thickness range. The vertical dashed gray lines in (a) mark the temperatures shown in (b).

throughout the A layer, we would arrive at an expression for the average magnetization identical to Eq. (1), but with labels “A” and “B” reversed. However, the magnetization does not scale linearly with the inverse bilayer thickness. The dotted line in the figure shows the simple linear model using the measured bulk value for  $M_A$  and the value for  $M_B$  extracted from Fig. 3(b), at 40 K. The samples with thicker A layers (5 nm and 10 nm) follow the model well but for smaller thicknesses (1.0 nm and 2.5 nm) the magnetization is lower than expected. This is a sign of a finite-size effect, where the magnetization in layer A is suppressed close to its interfaces [26], as shown schematically in Fig. 2(a). From the thickness where the data diverge from the dotted line, we can infer that the magnetically suppressed interface layer is between 1.25

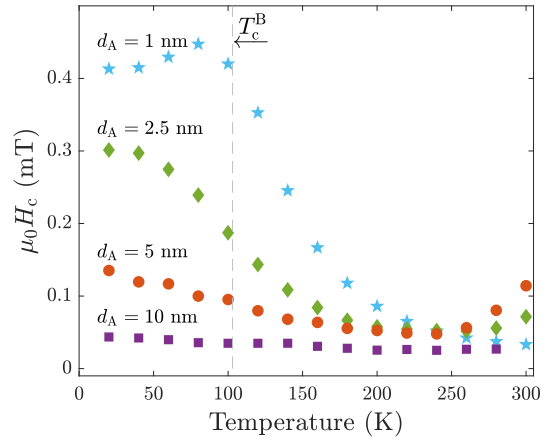


FIG. 5. The coercivity as a function of temperature for the A sample series. The gray vertical line marks the intrinsic  $T_c^B$ .

and 2.5 nm in thickness. A similar trend is not observed in the B-layer series since the magnetization at the B-layer side of the interfaces is in all cases enhanced by the proximity to the A layers. It is also worth noting that the magnetic proximity effect actually alters the finite-size effect, since the magnetization in the A layer does not go to zero at the interfaces as it would at an interface with a fully nonmagnetic material.

The temperature dependence of the coercivity of the A-layer series is shown in Fig. 5. In all cases we see a single-step switching, i.e., with both the A and B layers switching simultaneously, as shown in Fig. 2(a). For  $d_A = 10$  nm the coercive field is very small (approximately 0.05 mT) and constant throughout the entire temperature range. For smaller  $d_A$  the coercive field at 20 K increases due to the decreasing total magnetic moment of the A layers and the decreasing magnetization of the multilayer as a whole. This results in a decreasing torque from the applied field and therefore a higher field is required to switch the magnetization. At higher temperatures the coercive field of these samples decreases until it reaches a similar  $H_c$  as for the sample with  $d_A = 10$  nm. The drop in  $H_c$  occurs in those cases in a temperature region extending well above  $T_c^B$ , where for  $d_A = 1$  nm the enhancement in coercivity extends up to approximately 200 K.

Above  $T_c^B$  the A layers should switch independently of each other and their coercivity be determined by their intrinsic coercivity and finite-size effects. Below  $T_c^B$  the coercive field will be governed by the interplay between the coercivity of the B layers and the A layers. The B layers have an unknown coercivity and anisotropy since both properties may be strongly affected by the proximity of the A layers during growth. What we observe is that for thin  $d_A$ , the increase in the coercive field extends to much higher temperatures than expected. This must be due to a ferromagnetic ordering and spin stiffness in the intrinsically paramagnetic B layer due to the proximity of the ferromagnetic A layer which is sufficient to alter the overall coercivity of the multilayer.

The VSM measurements suggest that the magnetization of layer B within the multilayer can be well approximated

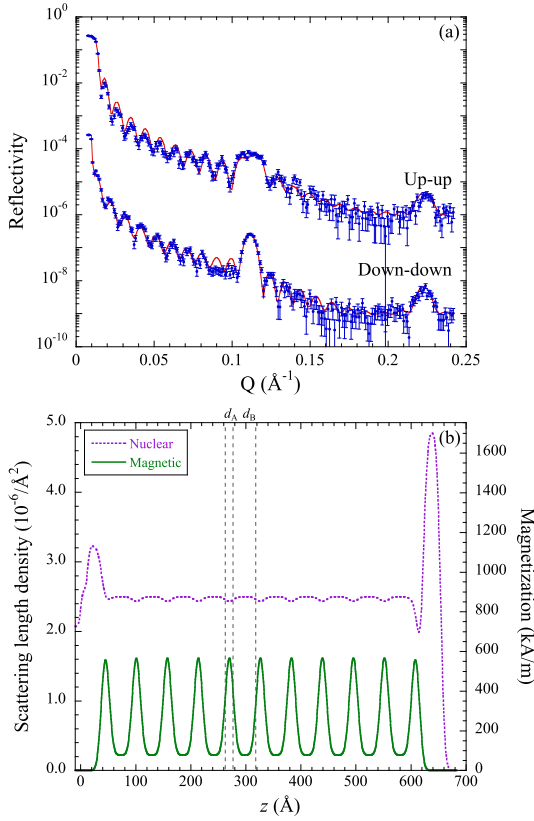


FIG. 6. (a) PNR measurements of the multilayer sample with  $d_A = 1.0$  nm and  $d_B = 5.0$  nm (blue dots), including fits (red lines), for the up-up and down-down spin channels, taken at 120 K. (b) Nuclear and magnetic scattering length density as a function of depth, producing the fits shown in (a).

by a constant value throughout its thickness. Yet they also show that finite-size effects reduce the magnetization of the A layers close to their interfaces. To investigate the profile of the magnetization in the A and B layers further and confirm the size of the magnetization in layer B, we have carried out PNR measurements. PNR gives depth resolved information about the magnetic moment of the sample and is therefore ideally suited for the study of magnetization profiles in layered structures. The reflectivity curves for the up-up and down-down spin channels are shown in Fig. 6(a) for the sample with nominally  $d_A = 1.0$  nm and  $d_B = 5.0$  nm, collected at a temperature of 120 K. Clear multilayer (Bragg) peaks are observed corresponding to both the nuclear and magnetic periodicity of the multilayer. Fitting in GenX yields thickness values of 1.3 and 4.3 nm for the A and B layers, respectively, and interface widths of approximately 0.6 nm. In addition, a 1.3 nm  $\text{SiO}_2$  is included on the substrate and a 3.2-nm surface oxide on the capping layer. The densities of each layer are fitted and allowed to vary by approximately 10% from the calculated values to allow for the slight reduction in density

due to the amorphous structure. This agrees well with the XRR results, although the interface widths are slightly higher in the PNR fit.

The fact that the up-up and down-down spin channels are different shows that there is indeed a magnetic contribution to the scattering length density (SLD). The full nuclear and magnetic SLDs obtained by fitting in GenX are shown in Fig. 6(b) as a function of depth  $z$ . A constant magnetization is assumed throughout the B-layers, in line with the simple magnetization model above [Eq. (1)], but the interface roughness is allowed to vary, producing the smoothly changing magnetic SLD across the interfaces. Since there is little nuclear contrast between layers A and B the roughness has a minimal effect on the nuclear SLD, whereas the strong magnetic contrast means that the roughness affects the magnetic SLD strongly. Therefore, although the same interface roughness is applied to both the nuclear and magnetic SLDs, the fitting is more sensitive to the magnetic interface profile than the structural (or nuclear) interface profile. The smoothly varying magnetic SLD is therefore a good approximation of the proximity induced magnetization profile across the interfaces, which explains why the PNR yields slightly higher interface widths than XRR. Nonetheless, layer thicknesses obtained in this way are consistent with XRR measurements and one bilayer is highlighted with the vertical dashed lines in the figure. The model fits the data well and the best fit is obtained with a nonzero moment in the middle of the B layers which confirms that the B layers carry a magnetic moment above  $T_c^B$ . The magnetic SLD can be converted to units of magnetization as shown in the figure. By integrating the magnetization over the thickness of layers A and B we can determine that the average magnetization in the layers is  $M_A = 510$  kA/m and  $M_B = 150$  kA/m.  $M_A$  is somewhat lower than the measured bulk value of 980 kA/m due to the finite-size effect and  $M_B$  is quite consistent with the value determined by applying the linear model to the VSM data in Fig. 3(b). These values correspond to an average magnetic moment per Co atom of  $0.75 \mu_B$  and  $0.35 \mu_B$  in the A and B layers, respectively. By integrating over the entire magnetization profile we find that the total magnetization is 230 kA/m which is in good agreement with the magnetization measured by VSM at 120 K.

#### IV. CONCLUSIONS

The magnetic proximity effect was investigated in multilayered structures of alternating  $\text{Co}_{60}(\text{Al}_{70}\text{Zr}_{30})_{40}$  (low  $T_c$ ) and  $\text{Co}_{85}(\text{Al}_{70}\text{Zr}_{30})_{15}$  (high  $T_c$ ). By fixing the thickness of the high- $T_c$  layer, the range of the induced magnetic ordering due to the proximity effect in the low- $T_c$  layer was determined by VSM measurements. The size of the induced magnetization is approximately constant throughout a 10-nm-thick  $\text{Co}_{60}(\text{Al}_{70}\text{Zr}_{30})_{40}$  layer, even at three times its intrinsic ordering temperature  $T_c^B$ . However, PNR measurements show that there is an interface region of smoothly varying magnetization between the layers but this region is small compared to the smallest B-layer thickness studied. Although the low- $T_c$  layer carries a magnetic moment in the entire temperature range studied, there are signs of a magnetic phase transition at a temperature somewhat above  $T_c^B$ . This indicates that there are two different magnetic phases induced by the proximity effect,

with different temperature dependence and extension. These results demonstrate the intricacies of magnetic proximity effects in amorphous metals and how they can fundamentally alter the behavior of such materials in layered structures. Much is still unknown about the nature of the induced magnetization such as its dynamic properties and the potential for controlling its size and extension with parameters other than temperature. Besides the obvious need to take magnetic proximity effects into account in the design of magnetic nanostructures, there

is great potential for using them to enhance the properties of low- $T_c$  materials or for tuning of magnetic properties in heterostructures.

### ACKNOWLEDGMENTS

This work was supported by the Icelandic Centre for Research, Grant No. 174271-051, the University of Iceland Research Fund, and the Swedish Research Council (VR).

- [1] R. M. White and D. J. Friedman, Theory of the magnetic proximity effect, *J. Magn. Magn. Mater.* **49**, 117 (1985).
- [2] M. J. Zuckermann, The proximity effect for weak itinerant ferromagnets, *Solid State Commun.* **12**, 745 (1973).
- [3] P. K. Manna and S. M. Yusuf, Two interface effects: Exchange bias and magnetic proximity, *Phys. Rep.* **535**, 61 (2014).
- [4] U. Bovensiepen, F. Wilhelm, P. Srivastava, P. Pouloupoulos, M. Farle, A. Ney, and K. Baberschke, Two Susceptibility Maxima and Element Specific Magnetizations in Indirectly Coupled Ferromagnetic Layers, *Phys. Rev. Lett.* **81**, 2368 (1998).
- [5] F. Magnus, M. E. Brooks-Bartlett, R. Moubah, R. A. Procter, G. Andersson, T. P. A. Hase, S. T. Banks, and B. Hjörvarsson, Long-range magnetic interactions and proximity effects in an amorphous exchange-spring magnet, *Nat. Commun.* **7**, 11931 (2016).
- [6] R. W. Wang and D. L. Mills, Onset of long-range order in superlattices: Mean-field theory, *Phys. Rev. B* **46**, 11681 (1992).
- [7] N. J. Gökemeijer, T. Ambrose, and C. L. Chien, Long-Range Exchange Bias Across a Spacer Layer, *Phys. Rev. Lett.* **79**, 4270 (1997).
- [8] W. J. Gallagher and S. S. P. Parkin, Development of the magnetic tunnel junction MRAM at IBM: From first junctions to a 16-Mb MRAM demonstrator chip, *IBM J. Res. Dev.* **50**, 5 (2006).
- [9] S. S. P. Parkin, Giant magnetoresistance in magnetic nanostructures, *Annu. Rev. Mater. Sci.* **25**, 357 (1995).
- [10] R. H. Victora and X. Shen, Composite media for perpendicular magnetic recording, *IEEE Trans. Magn.* **41**, 537 (2005).
- [11] C. Song, M. Sperl, M. Utz, M. Ciorga, G. Woltersdorf, D. Schuh, D. Bougeard, C. H. Back, and D. Weiss, Proximity Induced Enhancement of the Curie Temperature in Hybrid Spin Injection Devices, *Phys. Rev. Lett.* **107**, 056601 (2011).
- [12] Q. L. He, X. Kou, A. J. Grutter, G. Yin, L. Pan, X. Che, Y. Liu, T. Nie, B. Zhang, S. M. Disseler, B. J. Kirby, W. Ratcliff II, Q. Shao, K. Murata, X. Zhu, G. Yu, Y. Fan, M. Montazeri, X. Han, J. A. Borchers, and K. L. Wang, Tailoring exchange couplings in magnetic topological-insulator/antiferromagnet heterostructures, *Nat. Mater.* **16**, 94 (2016).
- [13] Z. Jiang, C.-Z. Chang, C. Tang, P. Wei, J. S. Moodera, and J. Shi, Independent tuning of electronic properties and induced ferromagnetism in topological insulators with heterostructure approach, *Nano Lett.* **15**, 5835 (2015).
- [14] P. Wei, F. Katmis, B. A. Assaf, H. Steinberg, P. Jarillo-Herrero, D. Heiman, and J. S. Moodera, Exchange-Coupling-Induced Symmetry Breaking in Topological Insulators, *Phys. Rev. Lett.* **110**, 186807 (2013).
- [15] M. A. Tomaz, W. J. Antel Jr, W. L. O'Brien, and G. R. Harp, Induced V moments in Fe/V(100), (211), and (110) superlattices studied using x-ray magnetic circular dichroism, *J. Phys.: Condens. Matter* **9**, L179 (1997).
- [16] H. Palonen, F. Magnus, and B. Hjörvarsson, Double magnetic proximity in Fe<sub>0.32</sub>V<sub>0.68</sub> superlattices, *Phys. Rev. B* **98**, 144419 (2018).
- [17] L. Cheng, Z. Altounian, D. H. Ryan, J. O. Ström-Olsen, M. Sutton, and Z. Tun, Pd polarization and interfacial moments in Pd-Fe multilayers, *Phys. Rev. B* **69**, 144403 (2004).
- [18] W. L. Lim, N. Ebrahim-Zadeh, J. C. Owens, H. G. E. Hentschel, and S. Urazhdin, Temperature-dependent proximity magnetism in Pt, *Appl. Phys. Lett.* **102**, 162404 (2013).
- [19] O. Rader, E. Vescovo, J. Redinger, S. Blügel, C. Carbone, W. Eberhardt, and W. Gudat, Fe-Induced Magnetization of Pd: The Role of Modified Pd Surface States, *Phys. Rev. Lett.* **72**, 2247 (1994).
- [20] C.-M. Choi, J.-O. Song, and S.-R. Lee, Thermal stability of magnetic tunnel junctions with new amorphous zral-alloy films as the under and capping layers, *IEEE Trans. Magn.* **41**, 2667 (2005).
- [21] P. Sharma, H. Kimura, and A. Inoue, Magnetic behavior of cosputtered Fe-Zr amorphous thin films exhibiting perpendicular magnetic anisotropy, *Phys. Rev. B* **78**, 134414 (2008).
- [22] R. Gemma, M. t. Baben, A. Pundt, V. Kapaklis, and B. Hjörvarsson, Consequences of randomness: Compositional contours in amorphous alloys, [arXiv:1811.03354](https://arxiv.org/abs/1811.03354).
- [23] R. A. Procter, F. Magnus, G. Andersson, C. Sánchez-Hanke, B. Hjörvarsson, and T. Hase, Magnetic leverage effects in amorphous SmCo/CoAlZr heterostructures, *Appl. Phys. Lett.* **107**, 062403 (2015).
- [24] F. Magnus, R. Moubah, A. H. Roos, A. Kruk, V. Kapaklis, T. Hase, B. Hjörvarsson, and G. Andersson, Tunable giant magnetic anisotropy in amorphous SmCo thin films, *Appl. Phys. Lett.* **102**, 162402 (2013).
- [25] H. Raanaei, H. Nguyen, G. Andersson, H. Lidbaum, P. Korelis, K. Leifer, and B. Hjörvarsson, Imprinting layer specific magnetic anisotropies in amorphous multilayers, *J. Appl. Phys.* **106**, 023918 (2009).
- [26] P. T. Korelis, P. E. Jönsson, A. Liebig, H.-E. Wannberg, P. Nordblad, and B. Hjörvarsson, Finite-size effects in amorphous Fe<sub>90</sub>Zr<sub>10</sub>/Al<sub>75</sub>Zr<sub>25</sub> multilayers, *Phys. Rev. B* **85**, 214430 (2012).
- [27] M. Björck and G. Andersson, GenX: An extensible X-ray reflectivity refinement program utilizing differential evolution, *J. Appl. Crystallogr.* **40**, 1174 (2007).



# Paper II

## **Exchange-spring magnets with crossed perpendicular and in-plane anisotropies**

K.A. Thórarinsdóttir, T. Hase, B. Hjörvarsson, F. Magnus

Physical Review B, **103**,014440 (2021)





# Amorphous exchange-spring magnets with crossed perpendicular and in-plane anisotropies

K. A. Thórarindóttir<sup>1</sup>,<sup>\*</sup> T. Hase,<sup>2</sup> B. Hjörvarsson,<sup>3</sup> and F. Magnus<sup>1,\*</sup>

<sup>1</sup>*Science Institute, University of Iceland, Dunhaga 3, IS-107 Reykjavik, Iceland*

<sup>2</sup>*Department of Physics, University of Warwick, Coventry CV4 7AL, United Kingdom*

<sup>3</sup>*Department of Physics and Astronomy, Uppsala University, Box 530, SE-75121 Uppsala, Sweden*



(Received 8 September 2020; accepted 13 January 2021; published 25 January 2021)

We study the magnetic coupling in a thin film bilayer exchange-spring magnet composed of an amorphous Tb<sub>10</sub>Co<sub>90</sub> layer with a large perpendicular anisotropy and an amorphous Co<sub>85</sub>(Al<sub>70</sub>Zr<sub>30</sub>)<sub>15</sub> layer with uniaxial in-plane anisotropy. The CoAlZr is directly exchange coupled to the TbCo with an interface region of at least 7.5 nm within which the CoAlZr magnetization is perpendicular to the plane and switches with the underlying TbCo. The influence of the coupling extends up to 30 nm into the CoAlZr resulting in an effective tilted anisotropy. The coercivity of the CoAlZr is greatly enhanced due to the coupling and is tuneable over a large range by varying its thickness.

DOI: [10.1103/PhysRevB.103.014440](https://doi.org/10.1103/PhysRevB.103.014440)

## I. INTRODUCTION

Exchange-spring magnets are composite systems where a hard magnetic layer is coupled through interfacial exchange coupling to a magnetically softer layer. The resulting composite can have the high remanent magnetization of the soft layer as well as the high coercive field of the hard layer. The high energy product is beneficial both for permanent magnets and magnetic storage media. Exchange-spring magnets, where both layers have in-plane magnetic anisotropy (IMA), have been studied extensively [1–3], and it has been shown that the switching properties can be tuned by varying the anisotropy and thickness of the two layers [4,5] as well as the interface structure [6,7]. Spring magnets with perpendicular magnetic anisotropy (PMA) have also been studied and are used in perpendicular magnetic recording [8,9].

In any recording media there is a tradeoff between achieving thermal stability and low switching fields (write fields) when increasing areal density. As the size of the magnetic grains is reduced beyond a certain limit they become thermally unstable and this is referred to as the superparamagnetic limit [10]. Perpendicular recording has allowed materials with higher anisotropy to be used, thus increasing stability compared to longitudinal media [9]. However, a drawback to using a fully PMA layer in magnetic recording media is the high switching field needed to reverse the magnetization. A potential solution to this limitation is to use heat-assisted switching, where the material is temporarily heated to its ordering temperature to reduce its coercive field [11]. Another suggestion to increase areal density and lower the switching field is to use thin films with tilted magnetization [12]. Thin films where the magnetic moment is tilted from the film plane have been achieved by growing magnetic layers on curved nanoislands [13,14] by growing the film such that the film

grains are at an angle from the substrate [15] or by making composite systems with mixed magnetic anisotropies [16,17].

In the present study, we examine the magnetic properties of amorphous heterostructures composed of two exchange coupled layers with IMA and PMA. Amorphous materials are highly uniform and free of point defects and step edges, which makes them ideally suited to magnetic heterostructures [18]. The magnetic anisotropy of amorphous thin films can be tuned both by growing the samples in a constant magnetic field or tailoring their composition [19]. Furthermore, strong interfacial exchange coupling has been demonstrated in amorphous heterostructures resulting, for example, in large magnetic proximity effects [3] and magnetic leverage effects [20]. Therefore, there is great potential for engineering amorphous heterostructures so that they display a specific complex magnetic response [3]. Here, we examine how the PMA of a TbCo layer results in a tilted magnetization of a coupled soft CoAlZr layer with imprinted uniaxial IMA. TbCo is known to have a strong growth induced PMA and exhibit all-optical magnetic switching [21]. We determine the range of the direct exchange coupling between the two layers and its effect on the overall magnetic response of the composite system. We find that the extension of the coupled region is large which can be used to control the effective anisotropy of the bilayer.

## II. EXPERIMENTAL METHODS AND DESIGN

The samples were grown using dc magnetron sputtering in a sputtering chamber with a base pressure below  $5 \times 10^{-9}$  mbar. The sputtering gas was Ar of 99.9999% purity and growth pressure  $2.00 \times 10^{-3}$  mbar. The Si(001) substrates (with the native oxide layer intact) were annealed in vacuum at 200 °C for 30 min prior to growth. First, a 2-nm-thick buffer layer of Al<sub>70</sub>Zr<sub>30</sub> was deposited from an Al<sub>70</sub>Zr<sub>30</sub> alloy target. Next, a bilayer of Tb<sub>10</sub>Co<sub>90</sub> and Co<sub>85</sub>(Al<sub>70</sub>Zr<sub>30</sub>)<sub>15</sub> was grown by co-sputtering from Co (purity 99.9%), Tb (purity 99.9%),

\*fridrikm@hi.is

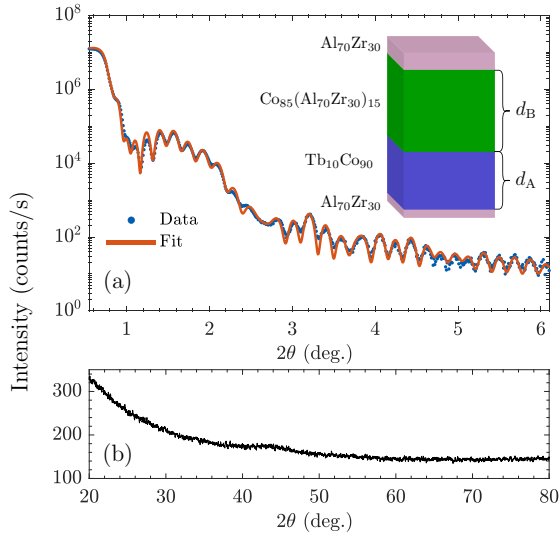


FIG. 1. (a) A representative XRR measurement including a fit, showing the low interface roughness of the bilayers. The inset shows a schematic of the sample structure corresponding to the measurement, where  $d_A = 30$  nm and  $d_B = 15$  nm. (b) A GIXRD measurement of the same sample, showing a single broad peak at approximately  $2\theta = 45^\circ$ . The measurement is representative of the entire sample series.

and  $\text{Al}_{70}\text{Zr}_{30}$  alloy targets. Finally, all samples were capped with 4-nm  $\text{Al}_{70}\text{Zr}_{30}$ . The sample structure is shown in the inset of Fig. 1(a).

The amorphous atomic structure of the samples was confirmed using grazing incidence x-ray diffraction (GIXRD) and the layer thicknesses and interface roughnesses determined by x-ray reflectivity (XRR). Characteristic XRR, including a fit, and GIXRD are shown in Figs. 1(a) and 1(b), respectively. The XRR shows Kiessing fringes up to at least  $2\theta = 6^\circ$ , confirming low interface roughness. Fitting the data confirms that the actual thicknesses agree with the nominal ones. A typical root-mean-square interface roughness is 0.6 nm between the TbCo and CoAlZr layers, allowing us to rule out intermixing effects. The GIXRD shows a single broad peak at approximately  $2\theta = 45^\circ$  which is characteristic of amorphous structures [19]. More information on the structural characterization methods can be found in Ref. [22].

Vibrating sample magnetometry (VSM) in a longitudinal geometry was used for magnetic characterization. All measurements were carried out at 20 K with applied fields up to 5 T. VSM measures the projection of the total magnetic moment along the measurement axis. In multicomponent magnetic samples the hysteresis loops obtained in this way can be composed of two or more different magnetic responses superimposed.

The samples were grown in a constant in-plane magnetic field of approximately 130 mT which induces a uniaxial in-plane magnetic anisotropy (IMA) in the CoAlZr layer. To study how the strong PMA from the TbCo affects the soft IMA CoAlZr, a series of samples were grown with the TbCo

thickness fixed at 30 nm and the CoAlZr thickness ranging between 5 and 80 nm. For a few thicknesses, additional samples were made with a 2.5-nm-thick AlZr spacer layer inserted between the TbCo and CoAlZr layers. This allows us to separate the effects of direct exchange coupling and stray field coupling on the magnetic response [17]. It has been demonstrated previously that there is no interlayer exchange coupling through amorphous  $\text{Al}_{70}\text{Zr}_{30}$  layers of this thickness through either RKKY coupling or proximity induced magnetism [23].

### III. RESULTS AND DISCUSSION

Out-of-plane and in-plane hysteresis loops of single CoAlZr and TbCo layers are shown in Figs. 2(a) and 2(b), respectively. The CoAlZr has a square hysteresis loop along its in-plane easy axis, defined by the applied growth field, with a low coercive field ( $<10$  mT) while in the perpendicular in-plane direction the remanence is zero (not shown). In the out-of-plane direction it has a high saturation field of 1.1 T and zero remanence. This shows that it has a small but well-defined uniaxial IMA.

The TbCo has a square hysteresis loop in the out-of-plane direction with  $H_c = 190$  mT. In the in-plane direction the saturation field is above the highest available field of 5 T. Therefore it has a large PMA, although the small nonzero remanence in the in-plane direction suggests that there is a small component of the film with less well defined anisotropy, which increases when growing the samples in a constant in-plane magnetic field [24]. TbCo and TbFe are ferrimagnets which are known to have a strong PMA. It has been suggested that the origin of the PMA in amorphous TbFe thin films is short-range structural ordering, similar to texturing in polycrystalline films, which is a result of minimization of the surface energy during deposition [25]. The structural and magnetic anisotropy is strongly correlated, where the Tb-Fe pair correlations are found to be larger out-of-plane, while Fe-Fe and Tb-Tb correlations are greater in-plane [26]. A similar effect can be expected in TbCo. The antiparallel alignment of the Tb and Co magnetic moments results in a compensation temperature (where the magnetization is zero and the coercivity diverges) when the magnetic moments cancel. This compensation temperature varies with composition [24].

Putting the TbCo and CoAlZr layers together with a non-magnetic AlZr spacer layer we obtain the magnetic response shown in Fig. 2(c). The hysteresis loop measured out of plane is a sum of the square easy-axis loop corresponding to the TbCo and the hard-axis loop of the CoAlZr. This is clear from the fact that the coercivity matches that of the TbCo and the saturation field matches that of the CoAlZr. Additionally, there is a small step at roughly 10 mT, corresponding to approximately 2% of the total CoAlZr moment. Since there is no direct exchange coupling, the step has to originate from magnetic anisotropy. During growth we apply a magnetic field of 130 mT parallel to the film plane, but in addition the CoAlZr layer experiences a large stray field from the TbCo. On this length scale, the stray field is uniform, so the total field is approximately uniform and tilted at an unknown angle with respect to the plane. CoAlZr is susceptible to field imprinting of anisotropy during growth [3], and therefore a small tilting

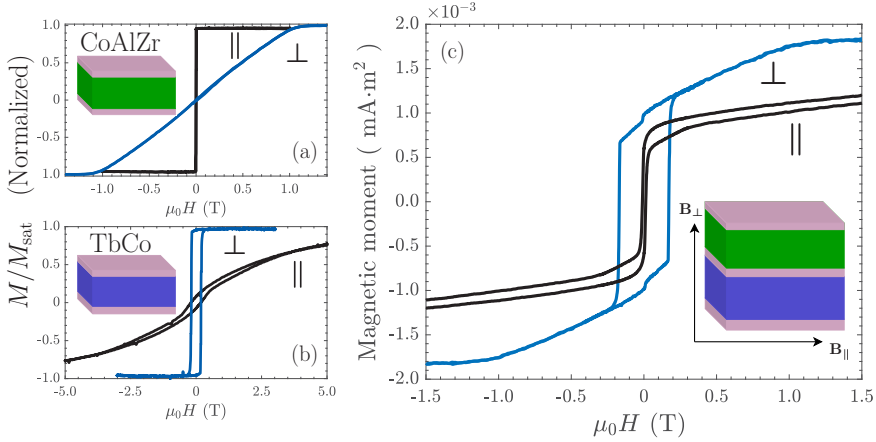


FIG. 2. Magnetic hysteresis loops measured by VSM in the out-of-plane and in-plane directions on (a) a single layer of CoAlZr and (b) a single layer of TbCo. The TbCo has a well-defined PMA whereas the CoAlZr has a clear uniaxial IMA. (c) The magnetic response of a TbCo(30 nm)/AlZr(2.5 nm)/CoAlZr(15 nm) sample, measured both in-plane and out-of-plane by VSM. The AlZr spacer layer decouples the two magnetic layers such that they switch independently. Data are shown between  $-1.5$  T to  $1.5$  T for clarity, with the measurement extending to  $\pm 5$  T.

of the anisotropy out of the plane can result. From the size of the magnetization step we estimate that the in-plane easy axis is tilted out of the plane by approximately  $1^\circ$ . The in-plane measurement is a sum of a square loop with a low coercive field and a hard-axis loop with a slight opening and saturation field above 5 T. At zero field, the remanence measured in-plane and out-of-plane corresponds to the magnetic moment of the CoAlZr and TbCo layers, respectively. This shows that the two layers switch independently when there is no direct exchange coupling and the effect of the stray field from the TbCo on the CoAlZr is minimal.

Samples without an AlZr spacer layer have direct coupling between the two magnetic layers. A schematic of this sample structure is shown in the inset of Fig. 1(a). The TbCo thickness  $d_A$  is fixed at 30 nm for all samples and the CoAlZr thickness  $d_B$  ranges from 5 nm to 80 nm. Figures 3(a) and 3(b) show hysteresis loops out-of-plane and in-plane, respectively, for various  $d_B$ , including the single TbCo layer for reference ( $d_B = 0$ ). With increasing thickness of the CoAlZr the out-of-plane response gradually evolves from the square response characteristic of a PMA material to a mixed easy and hard axis response. Similarly, the in-plane hysteresis loops acquire an increasingly large component which switches abruptly at low field with an associated increase in the remanent magnetization.

The hysteresis loops in Fig. 3 are the response of a multicomponent system with different anisotropies and magnetic moments. In order to separate these different responses we fit the hysteresis loops with a sum of modified Langevin functions of the form

$$M = A \left( \frac{1}{\tanh \frac{H \pm H_C}{S}} - \frac{1}{\frac{H \pm H_C}{S}} \right), \quad (1)$$

where  $A$  is the saturation moment,  $H_C$  is the coercive field,  $S$  determines the shape of the loop, and  $H$  is the applied field. The equation has no theoretical basis but can capture the

key parameters defining complex magnetic hysteresis loops. The fit is unique in cases where one or more square loops and an S-shaped (hard axis) loop is combined but can yield nonunique solutions when separating hysteresis loops that are a mixture of many hard responses saturating at different fields. By fitting the measured data with Eq. (1), we are able to separate the contribution from the two layers and extract robust values for the saturation moment and coercivity. In the out-of-plane direction, we find that for the smallest  $d_B$  only one hyperbolic function is required to fit the magnetic response, but for larger  $d_B$  a sum of two hyperbolic functions is needed to obtain a satisfactory fit. An example of this case is shown in Figs. 4(a) and 4(b). The total response is composed of a square loop with a large remanence and coercivity and a smooth S-shaped loop with zero remanence and a high saturation field. The low field step seen in Fig. 2(c) does not appear in the coupled system due to the strong direct exchange coupling between the TbCo and CoAlZr which dominates over the effect of the stray field.

Figure 4(c) shows the saturation moment of the two components forming the out-of-plane response plotted as a function of  $d_B$ . For the smallest CoAlZr thicknesses, there is only a square component and its saturation moment increases with increasing  $d_B$ . Above a certain threshold, the S-shape component appears and its saturation moment increases linearly with increasing  $d_B$  and the square component remains constant. This shows that part of the CoAlZr layer, below a threshold thickness, is strongly coupled to the TbCo layer and acts as an extension to the PMA layer. This is further borne out by the fact that the remanence of the square component equals its saturation moment, showing that this CoAlZr interface layer remains out-of-plane in the absence of an applied field. As the thickness of the CoAlZr exceeds the threshold, the magnetic moment within the CoAlZr layer beyond this threshold falls back into the film plane. By extrapolating the linear dependence of the saturation moment of the

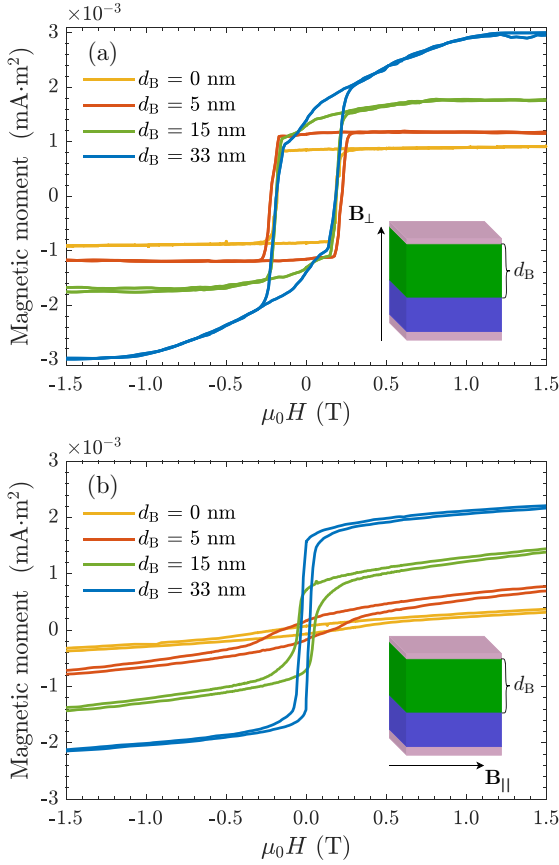


FIG. 3. The magnetic response of TbCo/CoAlZr bilayers with crossed anisotropies measured by VSM. (a) Out-of-plane hysteresis loops. (b) In-plane hysteresis loops, parallel to the growth field direction (in-plane easy axis). The data shown are between  $\pm 1.5$  T for clarity, with the measurements extending to  $\pm 5$  T.

CoAlZr we can determine the thickness of the interface layer, which is strongly coupled to the TbCo to be  $(7.5 \pm 0.2)$  nm. The excess out-of-plane saturation moment can similarly be determined to be  $(4.4 \pm 0.4) \times 10^{-4}$  mA m<sup>2</sup> which corresponds to a CoAlZr layer of thickness  $8.4 \pm 0.7$  nm.

Although the CoAlZr interface layer switches in unison with the TbCo layer when the field is applied perpendicular to the plane, it clearly has a magnetic response which is distinct from the TbCo. This becomes clear by studying the in-plane hysteresis loops in Fig. 3(b). These loops are composed of at least two “hard” loops, and an increasingly large “soft” loop emerges beyond  $d_B = 7.5$  nm. Due to nonuniqueness of the fit we cannot with certainty ascribe a magnetic moment separately to the two “hard” responses. However, the fitting allows us to identify three different regions of the sample. The first [labelled ‘A’ in the insets of Fig. 4(c)] is the PMA TbCo layer with a large in-plane saturation field ( $\approx 4.5$  T) and a small in-plane remanence. The second (labelled ‘B<sub>i</sub>’)

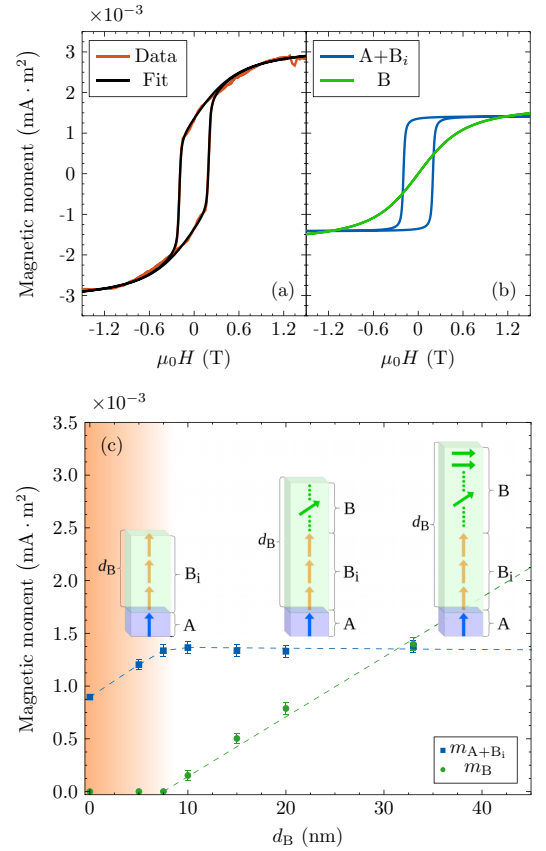


FIG. 4. (a) The hysteresis loop of a bilayer with  $d_B = 33$  nm (red) perpendicular to the plane. The data is fitted using Eq. 1 resulting in the solid black line. The fit is composed of two loops, shown in (b), a square loop and an S-shaped loop, corresponding to different components of the bilayer. (c) The saturation moment of the different components extracted from fitting the VSM data, as depicted in (a) and (b). The (blue) squares and (green) circles correspond to the square and S-loop, respectively. Up until  $d_B = 7.5$  nm there is no contribution from the hard axis loop, indicating that at least 7.5 nm of the soft CoAlZr switches with the TbCo. The dashed lines are a guide to the eye and extend to  $d_B = 80$  nm (not shown). The insets show the different magnetic components schematically.

corresponds to the CoAlZr interface region up to  $d_B = 7.5$  nm, with a weaker effective PMA characterized by an intermediate in-plane saturation field. The third (labelled ‘B’) is the CoAlZr beyond  $d_B = 7.5$  nm, where a crossover from PMA to IMA occurs. These different magnetic regions are depicted in a simple schematic in the insets of Fig. 4(c). We stress that the schematic is not a definitive representation of the remanent spin state of the bilayers and does not depict domain structure. In fact, the remanent state is metastable and depends on the field history of the sample.

Although the interface region B<sub>i</sub> has a thickness of approximately 7.5 nm the influence of the exchange coupling

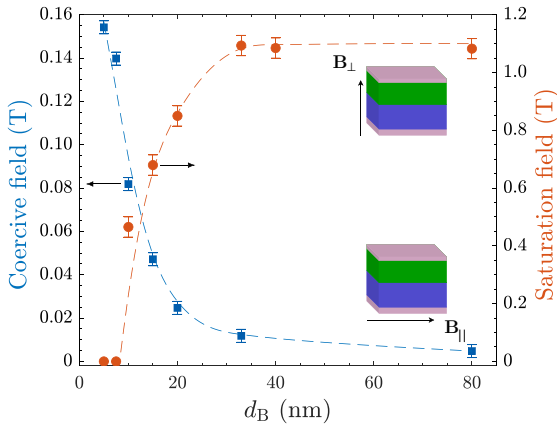


FIG. 5. (Left) Coercive field of hysteresis loops measured in-plane [Fig. 3(c)] as a function of thickness. For thin  $d_B$  the coercivity is enhanced by two orders of magnitude compared to bulk CoAlZr. (Right) The saturation field of the S-shape (hard axis) component loop from the out-of-plane measurement [Fig. 3(b)] plotted as a function of  $d_B$ . The field required to saturate the CoAlZr out-of-plane is significantly reduced for thicknesses below  $d_B = 33$  nm. Dashed lines are a guide to the eye.

between the TbCo and CoAlZr layers extends far beyond this thickness. Figure 5 shows the saturation field of the S-shape (hard axis) component of the *out-of-plane* hysteresis loops [Fig. 3(a)] and the coercive field when measuring *in-plane* [Fig. 3(b)], for different CoAlZr thicknesses  $d_B$ . These parameters reflect the influence that the coupling to the TbCo has on the properties of the CoAlZr. The influence of the coupling will decay with distance from the interface and the field required to rotate the CoAlZr moments out of the plane will vary continuously from the interface to the surface. The out-of-plane saturation field is therefore a measure of the strength of the coupling between the TbCo and the surface of the CoAlZr. For small  $d_B$  they are strongly coupled and the saturation field is strongly reduced, allowing the moments of the CoAlZr to be rotated perpendicular to the plane in

relatively small fields. This influence decreases with increasing  $d_B$  but only reaches the “bulk” value for CoAlZr (determined by shape anisotropy) for  $d_B > 33$  nm. This long-range influence is a result of the direct exchange coupling and not stray field coupling as demonstrated in the samples with a nonmagnetic spacer. This is further supported by the coercive field of the in-plane hysteresis loops. For small  $d_B$  the in-plane coercive field of the CoAlZr is enhanced by two orders of magnitude compared to its “bulk” value. For increasing  $d_B$  the coercive field decreases sharply but does not approach the bulk value until  $d_B > 33$  nm. This demonstrates the strong coupling in a bilayer system with crossed anisotropies and how it can be used to tune the switching properties and effective anisotropy both in-plane and perpendicular to the plane.

#### IV. CONCLUSIONS

A series of amorphous samples with crossed magnetic anisotropies was investigated in bilayered systems of TbCo (30 nm)/CoAlZr (5–80 nm). Due to the strong direct exchange coupling between the layers, a 7.5 nm thick region of the CoAlZr layer is pinned perpendicular to the plane and acts as an extension of the TbCo. The coercive field of the normally soft CoAlZr layer is strongly enhanced throughout a distance of at least 30 nm from the TbCo/CoAlZr interface, and in this region it acquires an effective tilted anisotropy. These results demonstrate the power of combining amorphous magnetic layers with widely different magnetic properties. The combination of seamless interfaces and susceptibility to field imprinting of anisotropy results in an unusually long-range coupling between the layers. This could be used for engineering high density magnetic recording media with tilted anisotropy as well as in spintronic devices using all-optical or spin-orbit torque-induced magnetic switching.

#### ACKNOWLEDGMENT

This work was supported by the Icelandic Centre for Research, Grant No. 174271-051, and the University of Iceland Research Fund.

- [1] E. E. Fullerton, J. S. Jiang, C. Rehm, C. H. Sowers, S. D. Bader, J. B. Patel, and X. Z. Wu, High coercivity, epitaxial Sm-Co films with uniaxial in-plane anisotropy, *Appl. Phys. Lett.* **71**, 1579 (1997).
- [2] E. E. Fullerton, J. S. Jiang, M. Grimsditch, C. H. Sowers, and S. D. Bader, Exchange-spring behavior in epitaxial hard/soft magnetic bilayers, *Phys. Rev. B* **58**, 12193 (1998).
- [3] F. Magnus, M. E. Brooks-Bartlett, R. Moubah, R. A. Procter, G. Andersson, T. P. A. Hase, S. T. Banks, and B. Hjörvarsson, Long-range magnetic interactions and proximity effects in an amorphous exchange-spring magnet, *Nat. Commun.* **7**, 11931 (2016).
- [4] S.-S. Yan, J. A. Barnard, F.-T. Xu, J. L. Weston, and G. Zangari, Critical dimension of the transition from single switching to an exchange spring process in hard/soft exchange-coupled bilayers, *Phys. Rev. B* **64**, 184403 (2001).
- [5] Z. J. Guo, J. S. Jiang, J. E. Pearson, S. D. Bader, and J. P. Liu, Exchange-coupled Sm-Co/Nd-Co nanomagnets: correlation between soft phase anisotropy and exchange field, *Appl. Phys. Lett.* **81**, 2029 (2002).
- [6] Y. Liu, S. G. E. te Velthuis, J. S. Jiang, Y. Choi, S. D. Bader, A. A. Parizzi, H. Ambaye, and V. Lauter, Magnetic structure in Fe/Sm-Co exchange spring bilayers with intermixed interfaces, *Phys. Rev. B* **83**, 174418 (2011).
- [7] Y. Choi, J. S. Jiang, J. E. Pearson, S. D. Bader, J. J. Kavich, J. W. Freeland, and J. P. Liu, Controlled interface profile in Sm-Co-Fe exchange-spring magnets, *Appl. Phys. Lett.* **91**, 072509 (2007).
- [8] S. M. Watson, T. Hauet, J. A. Borchers, S. Mangin, and E. E. Fullerton, Interfacial magnetic domain wall formation in perpendicular-anisotropy, exchange-spring films, *Appl. Phys. Lett.* **92**, 202507 (2008).

- [9] A. Berger, N. Supper, Y. Ikeda, B. Lengsfeld, A. Moser, and E. E. Fullerton, Improved media performance in optimally coupled exchange spring layer media, *Appl. Phys. Lett.* **93**, 122502 (2008).
- [10] R. Wood, The feasibility of magnetic recording at 1 terabit per square inch, *IEEE Trans. Magn.* **36**, 36 (2000).
- [11] R. E. Rottmayer, S. Batra, D. Buechel, W. A. Challener, J. Hohlfield, Y. Kubota, L. Li, B. Lu, C. Mihalcea, K. Mountfield *et al.*, Heat-assisted magnetic recording, *IEEE Trans. Magn.* **42**, 2417 (2006).
- [12] J. P. Wang, Y. Y. Zou, C. H. Hee, T. C. Chong, and Y. F. Zheng, Approaches to tilted magnetic recording for extremely high areal density, *IEEE Trans. Magn.* **39**, 1930 (2003).
- [13] M. Albrecht, G. Hu, I. L. Guhr, T. C. Ulbrich, J. Boneberg, P. Leiderer, and G. Schatz, Magnetic multilayers on nanospheres, *Nat. Mater.* **4**, 203 (2005).
- [14] M. Albrecht, Magnetic films on nanoparticle arrays, *The Open Surface Science Journal* **4**, 42 (2012).
- [15] B. Ma, H. Wang, H. Zhao, C. Sun, R. Acharya, and Jian-ping Wang, Structural and magnetic properties of a core-shell type L10 FePt/Fe exchange coupled nanocomposite with tilted easy axis, *J. Appl. Phys.* **109**, 083907 (2011).
- [16] S. Łazarski, W. Skowroński, J. Kanak, Ł. Karwacki, S. Zietek, K. Grochot, T. Stobiecki, and F. Stobiecki, Field-free spin-orbit-torque switching in Co/Pt/Co multilayer with mixed magnetic anisotropies, *Phys. Rev. Applied* **12**, 014006 (2019).
- [17] D. Markó, F. Valdés-Bango, C. Quirós, A. Hierro-Rodríguez, M. Vélez, J. I. Martín, J. M. Alameda, D. S. Schmool, and L. M. Álvarez Prado, Tunable ferromagnetic resonance in coupled trilayers with crossed in-plane and perpendicular magnetic anisotropies, *Appl. Phys. Lett.* **115**, 082401 (2019).
- [18] P. T. Korelis, A. Liebig, M. Björck, B. Hjörvarsson, H. Lidbaum, K. Leifer, and A. R. Wildes, Highly amorphous Fe<sub>90</sub>Zr<sub>10</sub> thin films, and the influence of crystallites on the magnetism, *Thin Solid Films* **519**, 404 (2010).
- [19] F. Magnus, R. Moubah, A. H. Roos, A. Kruk, V. Kapaklis, T. Hase, B. Hjörvarsson, and G. Andersson, Tunable giant magnetic anisotropy in amorphous SmCo thin films, *Appl. Phys. Lett.* **102**, 162402 (2013).
- [20] R. A. Procter, F. Magnus, G. Andersson, C. Sánchez-Hanke, B. Hjörvarsson, and T. Hase, Magnetic leverage effects in amorphous smco/coalzr heterostructures, *Appl. Phys. Lett.* **107**, 062403 (2015).
- [21] A. Ciuculkaite, K. Mishra, M. V. Moro, I.-A. Chioar, R. M. Rowan-Robinson, S. Parchenko, A. Kleibert, B. Lindgren, G. Andersson, C. S. Davies, A. Kimel, M. Berritta, P. M. Oppeneer, A. Kirilyuk, and V. Kapaklis, Magnetic and all-optical switching properties of amorphous Tb<sub>x</sub>Co<sub>100-x</sub> alloys, *Phys. Rev. Materials* **4**, 104418 (2020).
- [22] K. A. Thórarinsdóttir, H. Palonen, G. K. Palsson, B. Hjörvarsson, and F. Magnus, Giant magnetic proximity effect in amorphous layered magnets, *Phys. Rev. Materials* **3**, 054409 (2019).
- [23] Yu Fu, I. Barsukov, H. Raanaei, M. Spasova, J. Lindner, R. Meckenstock, M. Farle, and B. Hjörvarsson, Tailored magnetic anisotropy in an amorphous trilayer, *J. Appl. Phys.* **109**, 113908 (2011).
- [24] A. Frisk, F. Magnus, S. George, U. B. Arnalds, and G. Andersson, Tailoring anisotropy and domain structure in amorphous TbCo thin films through combinatorial methods, *J. Phys. D* **49**, 035005 (2015).
- [25] F. Hellman and E. M. Gyorgy, Growth-Induced Magnetic Anisotropy in Amorphous Tb-Fe, *Phys. Rev. Lett.* **68**, 1391 (1992).
- [26] V. G. Harris, K. D. Aylesworth, B. N. Das, W. T. Elam, and N. C. Koon, Structural Origins of Magnetic Anisotropy in Sputtered Amorphous Tb-Fe Films, *Phys. Rev. Lett.* **69**, 1939 (1992).



# Paper III

## **Finding order in disorder: Magnetic coupling distribution and competing anisotropies in an amorphous metal alloy**

K.A. Thórarinsdóttir, N. Strandqvist, V.V. Sigurjónsdóttir, E.B. Thorsteins-  
son, B. Hjörvarsson, F. Magnus

Applied Physics Letter Materials (2022)








# Finding order in disorder: Magnetic coupling distributions and competing anisotropies in an amorphous metal alloy

Cite as: APL Mater. 10, 041103 (2022); doi: 10.1063/5.0078748

Submitted: 15 November 2021 • Accepted: 7 March 2022 •

Published Online: 4 April 2022



K. A. Thórarinsdóttir,<sup>1,a)</sup>  N. Strandqvist,<sup>2</sup> V. V. Sigurjónsdóttir,<sup>1</sup> E. B. Thorsteinsson,<sup>1</sup> B. Hjörvarsson,<sup>2</sup>  and F. Magnus<sup>1,b)</sup> 

## AFFILIATIONS

<sup>1</sup> Science Institute, University of Iceland, Dunhaga 3, IS-107 Reykjavik, Iceland

<sup>2</sup> Department of Physics and Astronomy, Uppsala University, Box 530, SE-75121 Uppsala, Sweden

<sup>a)</sup> Author to whom correspondence should be addressed: [kth106@hi.is](mailto:kth106@hi.is)

<sup>b)</sup> Electronic mail: [fridrikm@hi.is](mailto:fridrikm@hi.is)

## ABSTRACT

Amorphous metals have unusual magnetic properties that arise due to the disordered atomic arrangement. We show that  $\text{Co}_x(\text{Al}_{70}\text{Zr}_{30})_{100-x}$  ( $65 < x < 92$  at. %) amorphous alloys have a distribution in the local magnetic coupling and ordering temperature, which can be explained by nanoscale composition variations. We use competing anisotropies induced by the substrate and an applied field during growth to probe the Co concentration distribution. Only regions with high enough Co concentration develop a magnetic anisotropy along the magnetic field during growth, whereas regions of low Co concentration have an anisotropy dictated by the substrate. A Gaussian distribution in the Co concentration of width 5.1 at. % is obtained from the variation in anisotropy. The results demonstrate the importance of composition variations for emergent magnetic properties and have far reaching implications for the properties of disordered materials in general.

© 2022 Author(s). All article content, except where otherwise noted, is licensed under a Creative Commons Attribution (CC BY) license (<http://creativecommons.org/licenses/by/4.0/>). <https://doi.org/10.1063/5.0078748>

## I. INTRODUCTION

Metallic glasses have long been a source of fascination due to their elusive structure and range of unusual properties.<sup>1,2</sup> Amorphous materials have a disordered atomic arrangement that makes them difficult to characterize structurally.<sup>3,4</sup> Unlike in crystalline materials, which are composed of periodically arranged atoms, the atoms in amorphous materials can be in a range of local environments with different coordination and interatomic distances. This means that linking the local structure of amorphous materials to emergent physical properties can be a highly tedious task.

Significant progress has been made in recent years toward characterizing the local atomic order in amorphous metals. X-ray scattering and absorption spectroscopy techniques have been employed to extract the atomic pair distribution functions that give information about the interatomic distances and coordination numbers.<sup>4–8</sup> In addition, direct observations of a local atomic order in amorphous

metals have been enabled by nano-beam electron diffraction<sup>9</sup> and atomic electron tomography.<sup>10</sup> These measurements have revealed a short-to-medium range order in the form of repeating single or multiple interconnected atomic clusters but without the long-range periodicity of crystalline solids. However, a recent study has shown by atom probe tomography, that local composition variations can exist in a binary metallic glass over a length-scale of several nanometers.<sup>11</sup> This far exceeds the typical size of atomic clusters and introduces a new length scale to consider in the study of disorder in materials.

Composition variations on the nanoscale may result in a spatial dependence of local properties that are unique to disordered materials. The width of the composition distribution could be highly dependent on the growth kinetics,<sup>12</sup> which may explain the wide disparity in the reported properties of nominally similar amorphous metal samples.<sup>13–15</sup> Furthermore, competing interactions between these regions of varying composition have the potential to shape

the overall response of the material. However, it is challenging to identify such competing interactions and probe the associated composition variations, which explains the limited data on the issue.

The most significant applications of metallic glasses to date are in soft magnets. This is because amorphous metals can have very low coercivity and, therefore, low hysteretic losses.<sup>2</sup> Nonetheless, amorphous metals can have a significant magnetic anisotropy.<sup>15,16</sup> Magnetic anisotropy is usually associated with a crystal anisotropy, but in amorphous metals, this cannot be the case. Despite the absence of crystalline order, short-to-medium range structural correlations can result in a substantial magnetostructural anisotropy.<sup>15,17</sup> Such correlations can be induced by various means, such as choice of the substrate, interface effects, and growth or annealing in a magnetic field.<sup>15,18,19</sup> Large magnetic proximity effects, where a magnetization is induced in a non-magnetic material due to proximity to a magnetic material,<sup>20–22</sup> have also been observed in amorphous heterostructures.<sup>23,24</sup> In the case of both anisotropy and the proximity effect, local composition variations have been suggested to play a crucial role,<sup>23–25</sup> but direct evidence of this has been lacking.

Here, we demonstrate that the magnetic properties of the amorphous alloy CoAlZr are shaped by local variations in its magnetic ordering temperature and anisotropy. We attribute these variations to a distribution in the concentration of the magnetic element Co and use the resulting effective anisotropy to determine the width of the Co atomic concentration distribution.

## II. METHODS

The samples were grown using dc magnetron sputtering in a sputtering chamber with a base pressure below  $5 \times 10^{-9}$  mbar. The sputtering gas was Ar of 99.9999% purity, and the growth pressure was  $2.40 \times 10^{-3}$  mbar. Si(100) substrates, with the native oxide layer intact, were used with no substrate heating. First, a buffer layer of 2-nm Al<sub>70</sub>Zr<sub>30</sub> was deposited from an Al<sub>70</sub>Zr<sub>30</sub> alloy target. Next, 40 nm of Co<sub>x</sub>(Al<sub>70</sub>Zr<sub>30</sub>)<sub>100–x</sub> ( $60 < x < 95$  at. %) was grown by co-sputtering from Co (99.9%) and Al<sub>70</sub>Zr<sub>30</sub> (99.9%) alloy targets. Finally, all samples were capped with 5-nm Al<sub>70</sub>Zr<sub>30</sub>. Samples were grown both with and without a uniform external magnetic field of 130 mT, parallel to the film plane.

The magneto-optical Kerr effect (MOKE) and vibrating sample magnetometry (VSM), both in a longitudinal setup, were used for magnetic characterization at room temperature and low temperatures, respectively. Structural characterization was done using a PANalytical X'pert Pro diffractometer, equipped with a Göbel mirror on the incident side and a parallel plate collimator on the diffracted side. The atomic arrangement (amorphous or polycrystalline) was determined using grazing incidence x-ray diffraction (GIXRD) with the incident angle fixed at  $\omega = 1^\circ$ . Layer thickness and interface roughness were measured using x-ray reflectivity (XRR), and XRR scans were fitted using the X'pert reflectivity software.

## III. RESULTS AND DISCUSSION

### A. Sample structure

A series of thin films of Co<sub>x</sub>(Al<sub>70</sub>Zr<sub>30</sub>)<sub>100–x</sub> with  $x$  in the range 60–100 at. % was studied. The films were bounded by thin layers of amorphous AlZr to ensure identical top and bottom interfaces

and prevent oxidation of the magnetic film. The sample structure is shown schematically in the inset of Fig. 1(a). XRR measurements were carried out to examine the layering of the samples, as shown in Fig. 1(a). Kiessig fringes are observed up to at least  $2\theta = 8^\circ$  confirming the well-defined layer thickness characteristic of amorphous films. Fitting the XRR data allows us to determine the thickness of each layer as well as the layer density and root-mean-square interface roughness, which is of the order of 0.5 nm. Figure 1(b) shows GIXRD measurements for several samples with the Co content ranging from 72 to 100 at. %. For the Co content 92% and above, there are small peaks present corresponding to hcp Co crystallites. The peaks are superimposed onto the broad peak centered at  $2\theta = 45^\circ$ . For  $x \leq 90$ , no sharp peaks are observed, and the GIXRD only shows the single broad peak typically found for amorphous materials.<sup>23,26</sup>

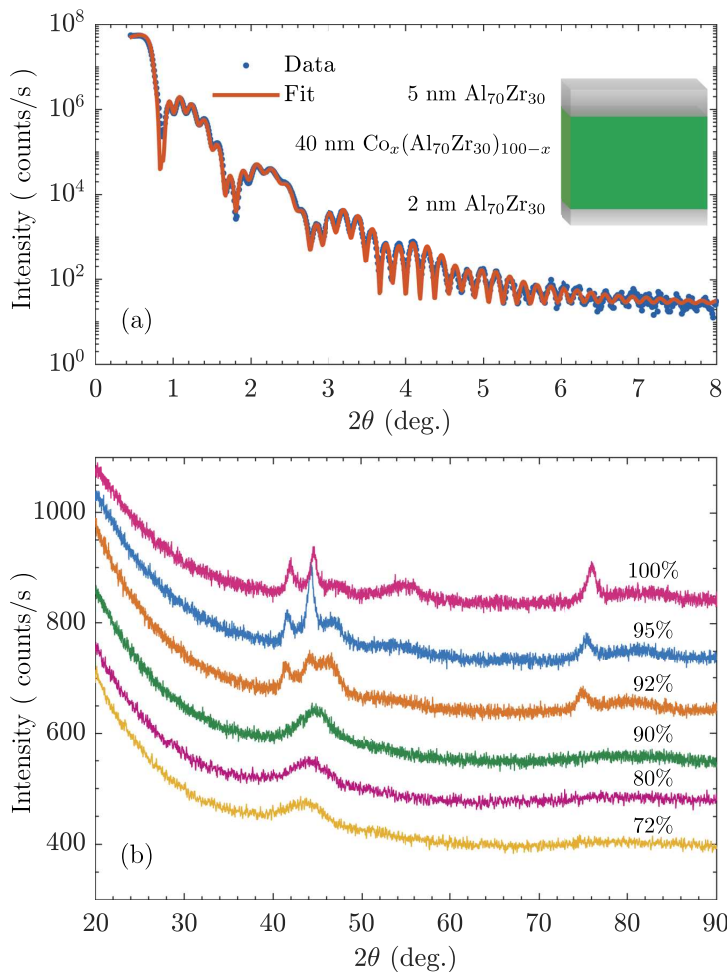
### B. Macroscopic magnetic properties

Figure 2 shows two hysteresis loops for a sample with 90% Co content measured along two orthogonal in-plane directions, which are characteristics for the sample series. During growth, we apply a uniform magnetic field parallel to the film plane that has been shown to induce a uniaxial anisotropy in thin magnetic films, with the easy axis direction parallel to the applied field.<sup>15,19,24,27,28</sup> The hysteresis loop parallel to the growth field is square, with a sharp single switch and a very low coercive field of  $H_c \approx 0.2$  mT. In the perpendicular in-plane direction, the loop has zero remanence but saturates at a low field. The inset shows a polar plot of the remanent magnetization  $M_{\text{rem}}$  as a function of the azimuthal angle  $\varphi$ . The uniaxial anisotropy is clear, with the easy directions where  $M_{\text{rem}}/M_{\text{sat}} = 1$  separated by  $180^\circ$  and a hard axis perpendicular to the easy axis. This can be described by a periodic function,

$$M_{\text{rem}} = M_{\text{sat}} |\cos(\varphi + \alpha)|, \quad (1)$$

as shown in Fig. 2. Here,  $\alpha$  is the offset of the easy axis with respect to the direction of the growth field ( $\varphi = 0$ ) and  $M_{\text{sat}}$  is the saturation magnetization. The close fit demonstrates that the film exhibits a small, but well-defined, uniaxial anisotropy. This applies to the entire composition range studied.

Figure 3 shows the saturation magnetization  $M_{\text{sat}}$  at 20 K (right, green circles) and Curie temperature  $T_c$  (left, blue squares) as a function of the Co content, measured by VSM. In the amorphous composition range below 92 at. % Co, the magnetization decreases linearly with the decrease in the Co content. This is consistent with the magnetization of other amorphous Co alloys.<sup>29</sup> An extrapolation of the linear dependence to 100 at. % Co reveals a magnetization of  $12.3 \times 10^5$  A/m, which is equivalent to an effective moment of  $1.47 \mu_B$  per Co atom. This is slightly below the magnetization of hcp Co. For dilution of Co with a fixed moment, one might expect the magnetization to go to zero at 0% Co. Here, however, the magnetization is reduced to zero at 66% Co. This is because the magnetic interaction in transition metals is through the itinerant electrons. Replacing a Co atom with non-magnetic Al or Zr not only removes the magnetic moment of a single atom but also decreases the magnetic moment of neighboring atoms. This results in a net decrease of  $4.3 \mu_B$  per Co atom, which is 2.7 times larger than the magnetic moment per atom in hcp Co.



**FIG. 1.** Sample design and structure. (a) X-ray reflectivity measurements representative of the sample series (blue dots), including a fit (red line), demonstrating the well-defined layering. The inset shows a schematic of the sample structure. (b) Grazing incidence x-ray diffraction of samples with composition ranging from 72 to 95 at. % Co. The data have been shifted for clarity. Samples with more than 8% AlZr do not show any crystal peaks and are x-ray amorphous.

Similarly, we observe a linear decrease in the Curie temperature  $T_c$  with the decrease in the Co content. The decrease in magnetization as a function of temperature is consistent with that of a typical ferromagnet (see, for example, Ref. 24). We define  $T_c$  as the temperature where the remanent magnetization becomes zero, and this is determined from full hysteresis loop measurements as a function of temperature. The Curie temperature can be viewed as a measure of the magnetic coupling strength  $J$ , since  $J$  is proportional to  $T_c$  according to the Weiss model of a ferromagnet.<sup>11,30</sup> We, therefore, also assign a unit of temperature to  $J$  for convenience. With the decrease in the Co content, the effective magnetic coupling between Co atoms is, therefore, reduced. A linear extrapolation of the Curie temperature to 100% Co gives  $T_c = (1200 \pm 100)^\circ\text{C}$ . This can be compared to  $T_c$  of *hcp* Co, which is  $1130^\circ\text{C}$ . Thus, one can assume a weak or negligible impact of disorder on the effective

Co–Co interactions, in stark contrast to what is observed for Fe.<sup>11</sup> Both the magnetization and  $T_c$  cross zero at  $(66.5 \pm 0.5)$  at. %, below which the alloy is not ferromagnetic at any temperature. This demonstrates the high degree of magnetic tunability of the CoAlZr alloy and also how sensitive its magnetic properties are to small changes in composition.

### C. Competing anisotropies

The simple linear dependence of magnetization and Curie temperature on composition hides a more complex picture of the amorphous film structure, revealed by a closer look at the magnetic anisotropy. As the Co content of the films is reduced below 85 at. %, we observe an anomalous rotation of the easy axis direction away from the direction of the imprinting (growth) field. Figure 4 shows a polar plot of the remanent magnetization of the sample with

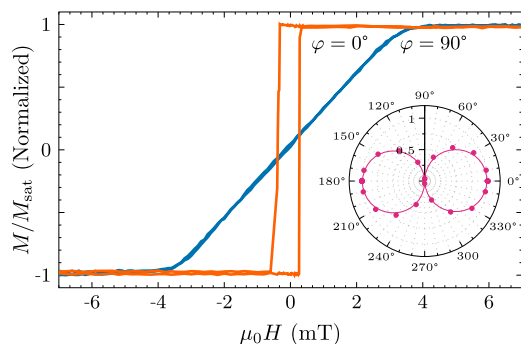


**FIG. 2.** Uniaxial magnetic anisotropy. Hysteresis loops of a film with 90% Co, measured parallel ( $\varphi = 0^\circ$ ) and perpendicular ( $\varphi = 90^\circ$ ) to the applied growth field. The inset shows the polar plot of the normalized remanent magnetization ( $M_{\text{rem}}/M_{\text{sat}}$ ) as a function of azimuthal angle  $\varphi$ , showing the well-defined uniaxial anisotropy.

75 at. % Co (blue dots). The anisotropy is still clearly uniaxial, but the easy axis is rotated by an angle of  $\alpha = 17^\circ$  with respect to the growth field. Furthermore, we find that the angle of the easy axis (with respect to the growth field) increases smoothly as the Co content is reduced. The angle  $\alpha$  is shown as a function of composition in Fig. 5(a). For a high Co content,  $\alpha = 0^\circ$  (easy axis parallel with the growth field), whereas for the lowest Co content,  $\alpha = 45^\circ$ .

To determine the cause of this rotation of the easy axis, a series of reference samples was grown without a growth field. The films grown without field are also uniaxial but their easy axis is fixed at  $\alpha = 45^\circ$ , irrespective of the composition. This is shown by the red

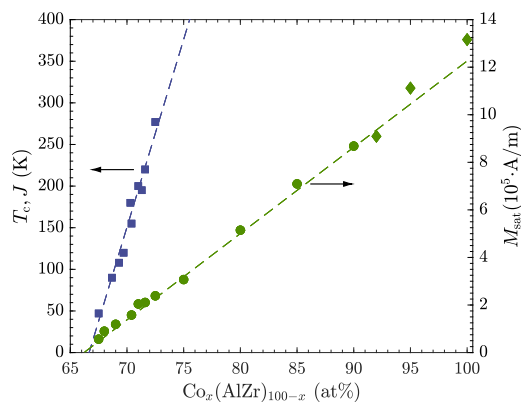


**FIG. 3.** Temperature dependence of magnetic properties. (Left) The Curie temperature  $T_c$ , as a function of Co atomic percentage  $x$ .  $T_c$  can be viewed as a measure of the magnetic coupling strength  $J$ . (Right) The saturation magnetization  $M_{\text{sat}}$  (at 20 mT) measured at 20 K as a function of  $x$ . Amorphous compositions are denoted by circles and polycrystalline compositions by diamonds. Both  $T_c$  and  $M_{\text{sat}}$  show a linear dependence on composition.

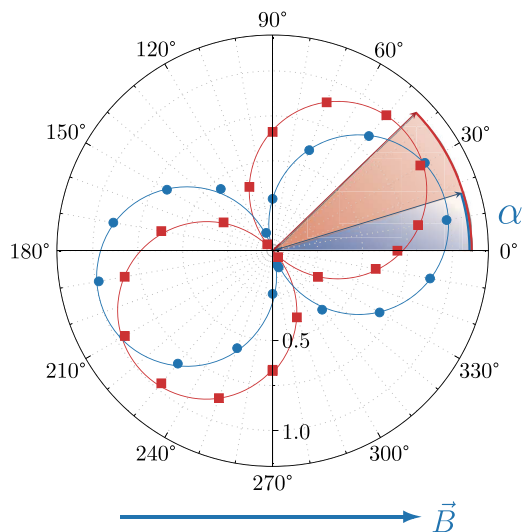


**FIG. 4.** Competing anisotropies. Polar plot of the normalized remanent magnetization of the sample with 75 at. % Co as a function of the azimuthal angle  $\varphi$  for a sample growth with (blue circles) and without (red squares) an external growth field  $B$ , including a fit using Eq. (1). The direction of the growth field is shown by the blue arrow below the graph. The easy axis angle  $\alpha$  depends on whether or not a growth field is applied.

squares in Fig. 4, also for 75 at. % Co. The uniaxial anisotropy can be eliminated by increasing the thickness of the amorphous AlZr buffer layer to 8 nm or by using a thermally oxidized Si substrate, as shown in the [supplementary material](#). We, therefore, conclude that we have a hierarchy of effects governing the anisotropy in the amorphous films: (i) A magnetic field during growth induces an anisotropy parallel to the field. (ii) In the absence of a growth field, the uniaxial anisotropy is dictated by the Si(100) substrate and the easy axis is parallel to the Si[110] in-plane direction. Without a growth field or substrate effects, the films are isotropic. We stress that all the films are x-ray amorphous, regardless of the thickness of the AlZr buffer layer or the presence of a growth field.

A material with two competing uniaxial anisotropy axes,  $A$  and  $B$ , will not, in general, exhibit two easy axes but rather a single easy axis  $C$ , where the easy axis will point in a direction between the two competing axes.<sup>31</sup> The easy axis angles between  $\alpha = 0^\circ$  and  $\alpha = 45^\circ$  observed here are, therefore, a result of the competition between the anisotropy induced by the growth field and the anisotropy induced by the substrate. The size of the two anisotropies is equal as evidenced by the equal saturation fields along the hard axis for samples grown with and without field (see the [supplementary material](#)). The difference lies in the direction of the easy axis.

Magnetic field imprinted anisotropy relies on a strong magnetic response of the growing film, i.e., the effective temperature during growth must be lower than the Curie temperature of the film. This means that field imprinted anisotropy only develops in films with sufficiently high Curie temperature. If the  $T_c$  of an alloy is below the

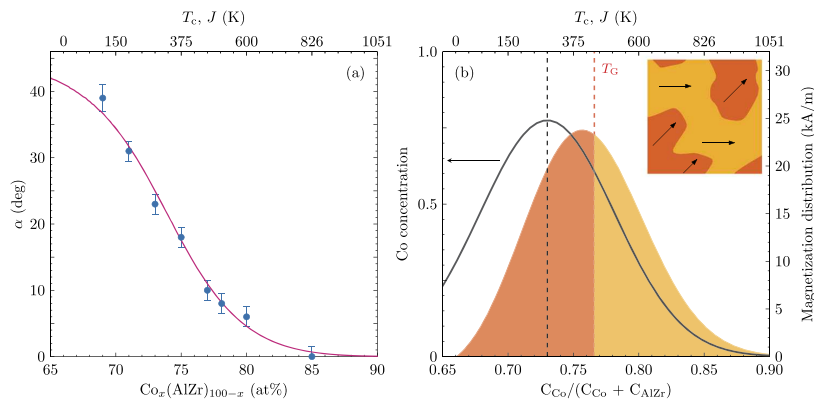


**FIG. 5.** The magnetization and Co concentration distributions. (a) The easy axis angle  $\alpha$  as a function of Co content including a fit using Eq. (4). For a high Co content, the easy axis is aligned with the growth field, whereas for a low Co content, it is aligned with the Si substrate [110] direction. (b) The Co concentration (black line) and magnetization distributions (orange–yellow shaded region) for the sample with  $x = 73\%$ . The area under the curve corresponds to the total magnetization of the sample. At temperatures above  $T_G$  (yellow area), the magnetization interacts with the growth field. The inset is an illustration of the regions with competing anisotropy axes. We find that the effective growth temperature is  $T_G = (450 \pm 90)$  K and  $\sigma = (5.1 \pm 0.8)$  at. %.

effective growth temperature, the anisotropy will be determined by the substrate. For a  $T_c$  above the growth temperature, the anisotropy will be determined by the growth field. If the magnetic coupling between Co atoms in the CoAlZr alloy was homogeneous such that there was a single uniform Curie temperature, we would expect a sharp transition in the direction of the anisotropy. The smooth change in  $\alpha$  as a function of composition in Fig. 5(a), therefore, shows that  $T_c$  is not as well-defined as shown in Fig. 3.

## D. Composition distribution

To understand how the competing anisotropy axes arise, we must look to the disordered structure of the amorphous films. Gemma *et al.*<sup>11</sup> have recently revealed the inhomogeneous composition of amorphous alloys on the nanometer scale by means of atom probe tomography on sputtered FeZr amorphous films. They showed that the elements are not evenly distributed resulting in regions with higher or lower concentration of the magnetic element, extending over a length scale of several nanometers. This, in turn, means that there is a variation in the effective magnetic coupling strength  $J$  on this length scale. Each sample has a well-defined global Curie temperature, where the remanence is reduced to zero, but, nonetheless, we can define a local Curie temperature that can be higher or lower, depending on the local concentration of the magnetic element.<sup>32–34</sup> At the global  $T_c$ , there may still exist disconnected regions that are magnetically ordered, but they do not exhibit long range ordering in the absence of an external field. These are essentially superparamagnetic regions that are easily polarizable and can mediate exchange coupling and proximity effects over several tens of nanometers.<sup>24,27</sup> As shown in Fig. 3, there is a strong change in effective coupling strength with composition in CoAlZr, meaning that there can potentially be a large variation in the local Curie temperature within each sample.

As mentioned previously, a material must have a strong magnetic response during growth to be susceptible to magnetic field imprinting of anisotropy. Due to the local variations in  $J(T_c)$ , only the regions with high enough  $J(T_c)$  will be susceptible to field imprinting. Regions with a lower Co content (lower  $J$ ,  $T_c$ ) will have their anisotropy dictated by the substrate. For films with sufficiently high mean Co concentration, the growth field induced anisotropy will dominate, whereas for low Co concentration films, the substrate induced anisotropy is dominant. In the intermediate composition region, the two mechanisms will coexist and the width of this composition region is determined by the width of the Co concentration distribution and the slope of the  $J(x)$  dependence.

To test this hypothesis, we can analyze the angular dependence of the anisotropy. The anisotropy constant describing the uniaxial in-plane anisotropy can be written as

$$K = \frac{\mu_0 M_{\text{sat}} H_{\text{sat}}}{2}, \quad (2)$$

where  $H_{\text{sat}}$  is the saturation field along the in-plane hard axis and  $M_{\text{sat}}$  is the saturation magnetization. We denote the anisotropy constant due to the substrate by  $K_A$  and the anisotropy constant due to the growth field as  $K_B$  and the angle between the two is  $45^\circ$ . The total anisotropy energy for the two competing anisotropies  $K_A$  and  $K_B$  can be written as

$$E_{\text{total}} = H_{\text{sat}} M_A \sin^2(\pi/4 - \alpha) + H_{\text{sat}} M_B \sin^2(\alpha), \quad (3)$$

where  $M_B$  is the part of the magnetization with anisotropy parallel to the growth field and  $M_A$  is the magnetization with anisotropy at  $45^\circ$ .  $H_{\text{sat}}$  is the saturation field measured along the respective hard axis, which, in this case, has the same magnitude for both  $K_A$  and  $K_B$ .

The direction of the easy axis,  $\alpha$ , can then be found by minimizing the total energy with respect to  $\alpha$ , giving

$$\alpha = \frac{1}{2} \arctan \frac{M_B}{M_A}. \quad (4)$$

The direction of the easy axis is, therefore, governed by the ratio of the partial magnetizations with the two anisotropy axes.

To determine the partial magnetizations, we assume that the distribution of Co concentration can be described by a Gaussian function, as shown by the solid black line in Fig. 5(b), centered at the mean Co concentration  $x$  and with a standard deviation  $\sigma$ . A similar approach has been taken to describe a distribution in blocking temperature due to disorder in a ferromagnetic–antiferromagnetic exchange coupled bilayer.<sup>35</sup> The magnetization distribution is then found by scaling the Gaussian Co concentration distribution with the magnetization as a function of composition  $M(x)$ , which is given by a linear fit of the magnetization in Fig. 3 (see the [supplementary material](#)). Figure 5(b) shows the magnetization distribution corresponding to a concentration distribution with a mean composition of  $x = 73$  at. %. The area under the curve equals the total magnetization of the sample (at 20 K). Each composition is also associated with a Curie temperature (through Fig. 3), which we can compare to the effective growth temperature  $T_G$ . The effective growth temperature determines the regions within the sample, which are affected by the applied magnetic field during growth. Regions that have  $(J, T_c) < T_G$  will couple with the substrate, whereas regions with  $(J, T_c) > T_G$  will align with the growth field. The partial magnetizations,  $M_A$  and  $M_B$ , in Eq. (4), are, therefore, the areas under the curve below (orange) and above (yellow)  $T_G$ , respectively.

The solid line in Fig. 5(a) is calculated from Eq. (4) based on partial magnetizations deduced from the Gaussian concentration distribution in Fig. 5(b). How steeply  $\alpha$  changes depends on  $\sigma$  of the Gaussian distribution, and thus, the width can be determined as  $\sigma = (5.1 \pm 0.8)$  at. %. The horizontal position of the curve is determined by the effective growth temperature that is found to be  $T_G = (450 \pm 90)$  K. This can be considered as the effective temperature of the condensing vapor as the atomic arrangement is formed. The model is in good agreement with the data, as shown by the close fit in Fig. 5(a).

#### IV. CONCLUSIONS

We have shown that unusual magnetic properties arise in amorphous thin films due to their disordered atomic arrangement. Local composition variations result in competing interactions that influence the development of the short-to-medium range structural order during growth. By taking advantage of competing uniaxial anisotropies induced by the substrate and growth field, we are able to map out the distribution in the local magnetic coupling. Only high Co concentration regions with local ordering temperature above the effective growth temperature are affected by the magnetic field during growth, whereas regions with lower ordering temperature are affected by the substrate. We show that these observed magnetic properties of the amorphous alloy can be attributed to a Gaussian distribution in the Co concentration.

The standard deviation of the distribution is a measure of how much the composition of the material varies on the length scale of

the magnetic interactions. A small spatial variation in  $T_c(J)$  would be associated with a narrow peak (small standard deviation) centered around the mean composition. On the other hand, a large spatial difference in  $T_c(J)$  would be a result of a wide composition distribution (large standard deviation). From our model, we find that the composition distribution has a standard deviation of 5.1 at. %, which is similar to that measured in the FeZr system.<sup>41</sup> However, it should be noted that any assessment of the composition distribution is always affected by the size of the probe. Indeed, for large enough probe sizes, the films in question are highly homogeneous as shown by macroscopic material characterization techniques.

The magnetic properties of CoAlZr are just one example of how the nanoscale composition variations inherent in amorphous alloys can affect their macroscopic properties. Such composition variations can explain the variability in the properties reported for seemingly identical amorphous alloys. The specific growth conditions, including the growth technique, temperature, and pressure, will influence the width of the distribution and, in turn, define the competing interactions that shape the emergent properties of the material. This can result in unexpected variability but may also be used to our advantage to tune the material performance. Therefore, it is crucial to be aware of this defining characteristic of disordered materials.

#### SUPPLEMENTARY MATERIAL

See the [supplementary material](#) for additional details of the substrate induced anisotropy, thickness dependence of  $\alpha$ , size of the anisotropy induced by the substrate and growth field, and the composition distribution model.

#### ACKNOWLEDGMENTS

This work was supported by the Icelandic Research Fund (Grant Nos. 174271 and 217843) and the University of Iceland Research Fund.

#### AUTHOR DECLARATIONS

##### Conflict of Interest

The authors have no conflicts to disclose.

#### DATA AVAILABILITY

The data that support the findings of this study are available from the corresponding author upon reasonable request.

#### REFERENCES

- W. Klement Jun, R. H. Willens, and P. Duwez, "Non-crystalline structure in solidified gold–silicon alloys," *Nature* **187**, 869–870 (1960).
- A. L. Greer, "Metallic glasses," *Science* **267**, 1947–1953 (1995).
- G. Xiao and C. L. Chien, "Nonuniqueness of the state of amorphous pure iron," *Phys. Rev. B* **35**, 8763–8766 (1987).
- H. W. Sheng, H. Z. Liu, Y. Q. Cheng, J. Wen, P. L. Lee, W. K. Luo, S. D. Shastri, and E. Ma, "Polyamorphism in a metallic glass," *Nat. Mater.* **6**, 192–197 (2007).
- H. W. Sheng, W. K. Luo, F. M. Alamgir, J. M. Bai, and E. Ma, "Atomic packing and short-to-medium-range order in metallic glasses," *Nature* **439**, 419–425 (2006).



- <sup>6</sup>D. Ma, A. D. Stoica, and X.-L. Wang, "Power-law scaling and fractal nature of medium-range order in metallic glasses," *Nat. Mater.* **8**, 30–34 (2008).
- <sup>7</sup>A.-C. Dippel, M. Roelsgaard, U. Boettger, T. Schneller, O. Gutowski, and U. Ruett, "Local atomic structure of thin and ultrathin films *via* rapid high-energy X-ray total scattering at grazing incidence," *IUCr* **6**, 290–298 (2019).
- <sup>8</sup>S. George, K. Kádas, P. E. Jönsson, G. Muscas, F. Magnus, O. Eriksson, A. Delin, and G. Andersson, "Local structure in amorphous  $\text{Sm}_x\text{Co}_{1-x}$ : A combined experimental and theoretical study," *J. Mater. Sci.* **55**, 12488 (2020).
- <sup>9</sup>A. Hirata, P. Guan, T. Fujita, Y. Hirotsu, A. Inoue, A. R. Yavari, T. Sakurai, and M. Chen, "Direct observation of local atomic order in a metallic glass," *Nat. Mater.* **10**, 28–33 (2010).
- <sup>10</sup>Y. Yang, J. Zhou, F. Zhu, Y. Yuan, D. J. Chang, D. S. Kim, M. Pham, A. Rana, X. Tian, Y. Yao *et al.*, "Determining the three-dimensional atomic structure of an amorphous solid," *Nature* **592**, 60–64 (2021).
- <sup>11</sup>R. Gemma, M. t. Baben, A. Pundt, V. Kapaklis, and B. Hjörvarsson, "The impact of nanoscale compositional variation on the properties of amorphous alloys," *Sci. Rep.* **10**, 11410 (2020).
- <sup>12</sup>B. R. Braeckman and D. Depla, "On the amorphous nature of sputtered thin film alloys," *Acta Mater.* **109**, 323–329 (2016).
- <sup>13</sup>M. Gronau, D. Schuffler, and S. Sprenger, "The magnetic properties of amorphous SmCo-films," *IEEE Trans. Magn.* **20**, 66–68 (1984).
- <sup>14</sup>K. Chen, H. Hegde, and F. J. Cadieu, "Induced anisotropy in amorphous Sm–Co sputtered films," *Appl. Phys. Lett.* **61**, 1861–1863 (1992).
- <sup>15</sup>F. Magnus, R. Moubah, A. H. Roos, A. Kruk, V. Kapaklis, T. Hase, B. Hjörvarsson, and G. Andersson, "Tunable giant magnetic anisotropy in amorphous SmCo thin films," *Appl. Phys. Lett.* **102**, 162402 (2013).
- <sup>16</sup>A. Frisk, F. Magnus, S. George, U. B. Arnalds, and G. Andersson, "Tailoring anisotropy and domain structure in amorphous TbCo thin films through combinatorial methods," *J. Phys. D: Appl. Phys.* **49**, 035005 (2016).
- <sup>17</sup>V. G. Harris, K. D. Aylesworth, B. N. Das, W. T. Elam, and N. C. Koon, "Structural origins of magnetic anisotropy in sputtered amorphous Tb-Fe films," *Phys. Rev. Lett.* **69**, 1939–1942 (1992).
- <sup>18</sup>F. Hellman and E. M. Gyorgy, "Growth-induced magnetic anisotropy in amorphous Tb-Fe," *Phys. Rev. Lett.* **68**, 1391–1394 (1992).
- <sup>19</sup>K. A. Thórarinsdóttir, T. Hase, B. Hjörvarsson, and F. Magnus, "Amorphous exchange-spring magnets with crossed perpendicular and in-plane anisotropies," *Phys. Rev. B* **103**, 014440 (2021).
- <sup>20</sup>M. J. Zuckermann, "The proximity effect for weak itinerant ferromagnets," *Solid State Commun.* **12**, 745–747 (1973).
- <sup>21</sup>R. M. White and D. J. Friedman, "Theory of the magnetic proximity effect," *J. Magn. Magn. Mater.* **49**, 117–123 (1985).
- <sup>22</sup>P. K. Manna and S. M. Yusuf, "Two interface effects: Exchange bias and magnetic proximity," *Phys. Rep.* **535**, 61–99 (2014).
- <sup>23</sup>F. Magnus, M. E. Brooks-Bartlett, R. Moubah, R. A. Procter, G. Andersson, T. P. A. Hase, S. T. Banks, and B. Hjörvarsson, "Long-range magnetic interactions and proximity effects in an amorphous exchange-spring magnet," *Nat. Commun.* **7**, ncomms11931 (2016).
- <sup>24</sup>K. A. Thórarinsdóttir, H. Palonen, G. K. Palsson, B. Hjörvarsson, and F. Magnus, "Giant magnetic proximity effect in amorphous layered magnets," *Phys. Rev. Mater.* **3**, 054409 (2019).
- <sup>25</sup>R. A. Procter, F. Magnus, G. Andersson, C. Sánchez-Hanke, B. Hjörvarsson, and T. P. A. Hase, "Magnetic leverage effects in amorphous SmCo/CoAlZr heterostructures," *Appl. Phys. Lett.* **107**, 062403 (2015).
- <sup>26</sup>P. T. Korelis, P. E. Jönsson, A. Liebig, H.-E. Wannberg, P. Nordblad, and B. Hjörvarsson, "Finite-size effects in amorphous  $\text{Fe}_{90}\text{Zr}_{10}/\text{Al}_{75}\text{Zr}_{25}$  multilayers," *Phys. Rev. B* **85**, 214430 (2012).
- <sup>27</sup>F. Magnus, R. Moubah, V. Kapaklis, G. Andersson, and B. Hjörvarsson, "Magnetostrictive properties of amorphous SmCo thin films with imprinted anisotropy," *Phys. Rev. B* **89**, 134414 (2014).
- <sup>28</sup>H. Raanaei, H. Nguyen, G. Andersson, H. Lidbaum, P. Korelis, K. Leifer, and B. Hjörvarsson, "Imprinting layer specific magnetic anisotropies in amorphous multilayers," *J. Appl. Phys.* **106**, 023918 (2009).
- <sup>29</sup>Y. Kakehashi, *Modern Theory of Magnetism in Metals and Alloys*, Springer Series in Solid-State Sciences Vol. 175 (Springer, Berlin, Heidelberg, 2013).
- <sup>30</sup>S. J. Blundell, *Magnetism in Condensed Matter* (Oxford University Press, 2014).
- <sup>31</sup>B. D. Cullity and C. D. Graham Jr., *Introduction to Magnetic Materials* (IEEE Press/Wiley, 2009).
- <sup>32</sup>R. Skomski and D. J. Sellmyer, "Curie temperature of multiphase nanostructures," *J. Appl. Phys.* **87**, 4756–4758 (2000).
- <sup>33</sup>L. Fallarino, B. J. Kirby, and E. E. Fullerton, "Graded magnetic materials," *J. Phys. D: Appl. Phys.* **54**, 303002 (2021).
- <sup>34</sup>J. Deisenhofer, D. Braak, H.-A. Krug von Nidda, J. Hemberger, R. M. Eremina, V. A. Ivashin, A. M. Balbashov, G. Jug, A. Loidl, T. Kimura, and Y. Tokura, "Observation of a Griffiths phase in paramagnetic  $\text{La}_{1-x}\text{Sr}_x\text{MnO}_3$ ," *Phys. Rev. Lett.* **95**, 257202 (2005).
- <sup>35</sup>S. Brück, J. Sort, V. Baltz, S. Suriñach, J. S. Muñoz, B. Dieny, M. D. Baró, and J. Nogués, "Exploiting length scales of exchange-bias systems to fully tailor double-shifted hysteresis loops," *Adv. Mater.* **17**, 2978–2983 (2005).





## Paper III: Supplementary information

### **Finding order in disorder: Magnetic coupling distribution and competing anisotropies in an amorphous metal alloy**

K.A. Thórarinsdóttir, N. Strandqvist, V.V. Sigurjónsdóttir, E.B. Thorsteins-  
son, B. Hjörvarsson, F. Magnus

Applied Physics Letter Materials (2022)



# Supplementary Information:

## Finding order in disorder: Magnetic coupling distributions and competing anisotropies in an amorphous metal alloy

K. A. Thórarinsdóttir,<sup>1</sup> N. Strandqvist,<sup>2</sup> V. V. Sigurjónsdóttir,<sup>1</sup> E. B. Thorsteinsson,<sup>1</sup> B. Hjörvarsson,<sup>2</sup> and F. Magnus<sup>1, a)</sup>

<sup>1)</sup>Science Institute, University of Iceland, Dunhaga 3, IS-107 Reykjavík, Iceland

<sup>2)</sup>Department of Physics and Astronomy, Uppsala University, Box 530, SE-75121 Uppsala, Sweden

### I. ANISOTROPY INDUCED BY THE SUBSTRATE

CoAlZr is an ultra-soft magnetic alloy and a number of factors can affect its magnetic anisotropy such as growth chamber geometry, substrate, buffer layer, external magnetic field, composition and sample shape. As we have shown, the final anisotropy axis can be defined by the competition of more than one factor. We have carefully examined the effect of each of the above to allow us to draw conclusions about the origin of the observed anisotropy. To eliminate the effects of chamber geometry, the samples were rotated continuously during growth and to minimize the effect of sample shape, samples were grown through a circular shadow mask without external magnetic field.

The effect of the substrate was studied by growing on a thermally oxidized Si substrate (with a 300 nm thick SiO<sub>2</sub> layer), a Si(100) substrate with only the native oxide and with a varying thickness of the amorphous AlZr buffer layer in the range 2-8 nm. Magnetic hysteresis loops shown in Fig. 1 are for Co<sub>75</sub>(AlZr)<sub>25</sub> films grown at the same time and with a buffer layer of 2-nm-thick AlZr. Fig. 1(a) shows hysteresis loops measured along  $\varphi = 0$  and  $90^\circ$ , grown on a thermally oxidized Si substrate with a thick SiO<sub>2</sub> layer. The inset shows a polar plot of the normalized remanent magnetization measured as a function of the azimuthal angle  $\varphi$ . Although a slight variation in remanent magnetization is observed, there is no clear easy or hard axis response. The same effect can be seen using a Si(100) substrate with native oxide and an 8-nm-thick AlZr buffer layer.

When growing on Si(100) substrates with only the native oxide and a buffer layer below 8 nm in thickness we start seeing an effect from the substrate. This is shown in Fig. 1(b). Here we have very well defined in-plane magnetic anisotropy (IMA) where the easy axis lies along the Si[110] in-plane direction of the Si(100) substrate. In the hard axis direction we have zero remanence and a saturation field of  $H_{\text{sat}} = 1$  mT. Therefore we can state that in the absence of in-plane shape anisotropy and substrate influence, the film is isotropic, whereas the effect of the Si(100) substrate is to induce a uniaxial anisotropy along the Si[110] in-plane direction.

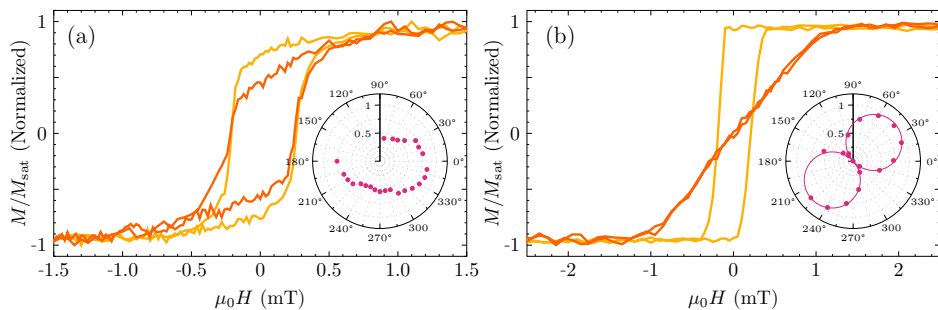


Figure 1. Normalized in-plane hysteresis loops measured along two orthogonal axes for Co<sub>75</sub>(AlZr)<sub>25</sub> grown on (a) thermally oxidized Si (thick SiO<sub>2</sub>) and (b) Si(100) with the native oxide. In addition, both films are grown on a 2-nm-thick AlZr buffer layer, through a circular mask without an external magnetic field. Insets: Polar plots of  $M_{\text{rem}}/M_{\text{sat}}$  as a function of the azimuthal angle  $\varphi$ . The film grown on thick SiO<sub>2</sub> is almost fully isotropic whereas the film grown on the Si(100) with native oxide has a uniaxial anisotropy along the Si[110] in-plane direction.

<sup>a)</sup>Electronic mail: kth106@hi.is

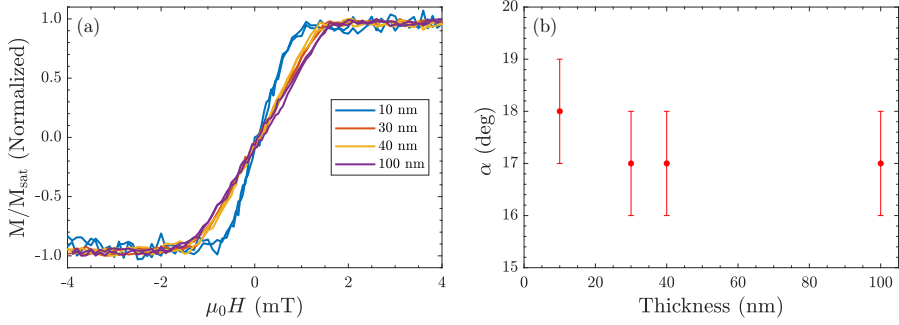


Figure 2. (a) Hysteresis loops measured along the hard axis of  $\text{Co}_{75}(\text{AlZr})_{25}$  films of varying thickness. The films are grown in an external magnetic field. A slight decrease in the anisotropy is observed for the thinnest film. (b) The direction  $\alpha$  of the easy axis relative to the growth field direction, measured for  $\text{Co}_{75}(\text{AlZr})_{25}$  of various thicknesses. The tilting of the easy axis away from the growth field does not depend on film thickness.

## II. THICKNESS DEPENDENCE OF SUBSTRATE INDUCED ANISOTROPY

In order to determine if the substrate induced anisotropy is a short-range interface effect or whether it is independent of thickness, a series of samples with thicknesses ranging from 10 to 100 nm with fixed composition of 75 at.% Co was grown in an external magnetic field. Hysteresis loops measured along the hard axis are shown in Fig. 2(a) and the easy axis angle  $\alpha$ , relative to the growth field, is shown in Fig. 2(b). A rotation of  $\alpha$  towards the growth field as the sample thickness is increased would indicate that the origin of the inplane magnetic anisotropy induced by the substrate is an interface effect that decays with distance from the interface. In the studied range,  $\alpha$  does not change with thickness, showing that it is not a decaying interface effect. Rather, the substrate induces an in-plane structural order in the amorphous films, analogous to crystalline texture. This is similar to the structural ordering observed in amorphous TbFe films which is responsible for the perpendicular magnetic anisotropy in such films. It should be noted however, that we observe a slight change in the saturation field for the 10-nm-thick film which could be due to strain or other interface effects.

## III. SIZE OF ANISOTROPY INDUCED BY SUBSTRATE AND GROWTH FIELD

The size of the anisotropy (the anisotropy constant) can be determined by measuring the saturation field along the hard axis. Fig. 3 shows hysteresis loops measured along the hard axis on 40 nm  $\text{Co}_x(\text{AlZr})_{100-x}$  grown with and without an external magnetic field for two different compositions (85 and 75 at.% Co). Inducing IMA with either substrate or external magnetic field results in the same saturation field  $H_{\text{sat}}$ , although the direction of the hard axis is not the same, as previously discussed. From this we can deduce that the structural origin of IMA induced by an external magnetic field and substrate is the same. Also, this simplifies the expression for the total anisotropy energy for the two competing anisotropies which allows us to arrive at the simple expression for the easy axis angle  $\alpha$ .

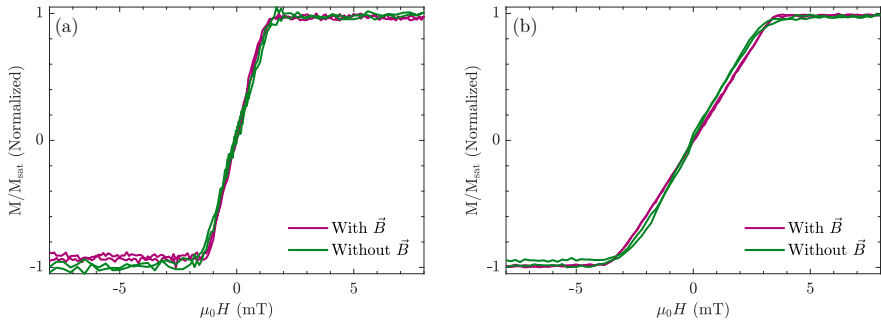


Figure 3. Hysteresis loops measured along the hard axis of 40-nm-thick  $\text{Co}_x(\text{AlZr})_{100-x}$  films grown with and without an external magnetic field with (a)  $x = 85$  at.% Co and (b)  $x = 75$  at.% Co. The saturation field is identical with and without the growth field indicating that the size of the anisotropy induced by the substrate and the growth field is equal. Note that the curves for samples grown with and without field are not measured along the same direction.

#### IV. COMPOSITION DISTRIBUTION MODEL

We explain the anomalous rotation of the angle  $\alpha$  away from the applied growth field as the Co content is decreased, by a competition between two uniaxial anisotropy axes. The distribution of Co within the sample can be described by a Gaussian probability function (solid black line in Fig.5(b)). This represents that within the sample there is a distribution of Co concentrations, where the mean composition is given by the peak of the Gaussian. Changing the Co content shifts the peak of the Gaussian distribution but we assume that the width (standard deviation) is constant. The interaction with the applied growth field depends on the local concentration within the film: Higher Co concentration regions will have a higher ordering temperature and will interact with the external field, while regions of lower Co concentration will not interact with the field.

Where the Co concentration is higher, there is a higher value of magnetic moment per unit area than for areas where the Co concentration is lower. Thus the magnetization distribution will be a Gaussian distribution scaled with the magnetization as a function of composition  $M(x)$ , which is given by a linear fit of the magnetization in Fig. 3. The magnetization distribution is therefore

$$f(x') = \frac{M(x')}{\sigma\sqrt{2\pi}} \exp\left(-\frac{1}{2}\left(\frac{x' - x}{\sigma}\right)^2\right) \quad (1)$$

where  $x$  is the mean composition of the  $\text{CoAlZr}$  alloy and  $\sigma$  is the standard deviation of the composition. This is shown by the filled area in Fig.5(b). We make the assumption that the measured critical temperature is representative of the mean composition of each sample. We then assign the measured critical temperature for each mean composition to the corresponding local concentration in the sample. The partial magnetizations,  $M^A$  and  $M^B$  in Eq.4 are then given by the areas above and below the *effective growth temperature*  $T_G$ , respectively. The angular dependence of the easy axis follows from Eq. 4 and 5. The measured data of  $\alpha$  as a function of composition can now be fitted by performing a Levenberg Marquard minimization. The magnetization, critical temperature and composition are known and therefore the fit can be performed using only the standard deviation  $\sigma$  and effective growth temperature  $T_G$  as variables. This results in the solid line in Fig. 5(a).